

**IN-SITU X-RAY SCATTERING STUDIES  
OF AG NANO-STRUCTURES**

---

A Dissertation presented to  
the Doctoral Committee  
at the University of Missouri

---

In Partial Fulfillment  
of the Requirements for the Degree  
Doctor of Philosophy

---

by

YIYAO CHEN

Dr. Paul F. Miceli, Dissertation Supervisor

May 2016

© Copyright by Yiyao Chen 2016

All Rights Reserved

The undersigned, appointed by the Dean of the Graduate School, have examined the dissertation entitled:

IN-SITU X-RAY SCATTERING STUDIES  
OF AG NANO-STRUCTURES

presented by Yiyao Chen,  
a candidate for the degree of Doctor of Philosophy and hereby certify that, in their opinion, it is worthy of acceptance.

---

Dr. Paul F. Miceli

---

Dr. Ioan Kosztin

---

Dr. Haskell Taub

---

Dr. Gavin King

---

Dr. C. Michael Greenlief

## ACKNOWLEDGMENTS

First of all, I would like to express my gratitude to my adviser, Dr. Paul F. Miceli. I am very thankful to have the opportunity to work with him, it is only with his support and guidance that I can finish my Ph.D study.

I would like to thank Drs. Ioan Kosztin, Haskell Taub, Gavin King, and Michael Greenlief for serving on my Doctoral Committee. My thanks also goes to Dr. Michael Tringides, Ames Laboratory, Iowa State University, for helpful discussions.

I am fortunate to have met my colleagues and friends Shawn Hayden, Michael Gramlich, and Jesse Kremenak with whom I performed experiments together, shared lab work, and discussed research projects.

Special thanks to my parents, Weimin Chen and Nan Wang, who have always given me love and support.

And I thank all the people that have given me help that are not listed here.

## TABLE OF CONTENTS

<b>LIST OF FIGURES</b> . . . . .	<b>vii</b>
<b>ABSTRACT</b> . . . . .	<b>xi</b>
<b>CHAPTER</b>	
<b>1 Introduction</b> . . . . .	<b>1</b>
<b>2 Background</b> . . . . .	<b>3</b>
2.1 Film growth modes[1] . . . . .	3
2.2 Quantum size effect . . . . .	5
2.2.1 Particle in a box . . . . .	5
2.2.2 Electron band filling . . . . .	6
2.3 Preferred island heights in Pb/Si . . . . .	9
2.4 Preferred island heights in Ag/Si . . . . .	12
2.4.1 Bilayer preference . . . . .	12
2.4.2 Is the preference due to QSE? . . . . .	13
<b>3 Scattering Theory</b> . . . . .	<b>16</b>
3.1 X-ray diffraction background[2] . . . . .	16
3.2 Crystal truncation rod . . . . .	21
3.3 The hexagonal coordinate system . . . . .	24
3.4 Different types of measurements . . . . .	26
<b>4 Ag/Si structure and morphology</b> . . . . .	<b>29</b>

4.1	Structural model for Ag/Si(111)7x7 . . . . .	30
4.1.1	Specular reflectivity . . . . .	32
4.1.2	Crystal truncation rod calculation . . . . .	35
4.1.3	Corrections from scattering geometry . . . . .	42
4.2	Vertical structure of Ag thin film from specular reflectivity measurements	43
4.2.1	Coverage dependence measurements . . . . .	44
4.2.2	Temperature dependence measurements . . . . .	49
4.2.3	Measurements for annealing experiments . . . . .	52
4.3	Vertical structure of 21.6 ML Ag film . . . . .	52
4.3.1	Binomial distribution model . . . . .	52
4.3.2	Low density at the interface . . . . .	57
4.4	Fitting parameter tables for specular reflectivity and rods . . . . .	61
4.5	The absence of Ag lattice expansion . . . . .	65
4.6	Ag wetting layer and transition to FCC islands . . . . .	68
4.7	Ag domain rotation . . . . .	75
4.7.1	60 degree rotation . . . . .	75
4.7.2	15.7 degree rotation . . . . .	77
4.7.3	Coincidence Site Lattice calculations . . . . .	80
4.8	Conclusion: Explanation for the height selection . . . . .	85
<b>5</b>	<b>Poisson-like island height distribution . . . . .</b>	<b>89</b>
5.1	The mean and variance from island height distributions . . . . .	90
5.1.1	Normalized island height distribution . . . . .	90

5.1.2	Constant difference between the mean and the variance . . . . .	90
5.2	Trials with simple statistic models . . . . .	94
5.2.1	Shifted Poisson distribution model . . . . .	94
5.2.2	Binomial distribution model . . . . .	95
5.3	Modified Poisson distribution model . . . . .	96
5.3.1	The derivation of the conventional Poisson distribution . . . . .	97
5.3.2	Poisson distribution with different layer probabilities . . . . .	99
5.3.3	Calculation of modified Poisson distribution . . . . .	100
5.3.4	The effect of the $\lambda_j$ parameters . . . . .	102
5.3.5	Final model for Modified Poisson distribution . . . . .	102
5.4	Conclusion . . . . .	107
<b>6</b>	<b>Ag/Ag homoepitaxial results . . . . .</b>	<b>108</b>
6.1	Background . . . . .	109
6.2	Ag/Ag diffuse scattering . . . . .	113
6.3	Ag/Ag coverage-dependent diffuse scattering data . . . . .	115
6.3.1	Elastic boundary conditions at the stress free surface . . . . .	117
6.3.2	Thin film scattering effect . . . . .	125
6.3.3	Numerical integration . . . . .	125
6.4	Analysis of Amar's simulation results . . . . .	126
6.4.1	The average surface normal strain . . . . .	128
6.4.2	Local in-plane displacement . . . . .	133
6.4.3	Conclusion of the MD simulation . . . . .	139

6.5	Diffuse intensity calculation from simulated results . . . . .	140
6.5.1	Finite Size Effect . . . . .	140
6.5.2	Treatment to smooth out the oscillations . . . . .	142
6.5.3	Random defect model . . . . .	146
6.5.4	Conclusion . . . . .	157
<b>APPENDIX</b>		
<b>A</b>	<b>Geometry Correction Calculations . . . . .</b>	<b>158</b>
A.1	Motor angle conversion . . . . .	158
A.2	Scattering angle calculation . . . . .	162
A.3	Geometry corrections . . . . .	163
A.3.1	Rocking scans (crystal truncation rod) . . . . .	164
A.3.2	Stationary geometry (specular reflectivity) . . . . .	169
<b>BIBLIOGRAPHY . . . . .</b>		<b>171</b>
<b>VITA . . . . .</b>		<b>179</b>



## LIST OF FIGURES

Figure	Page
2.1 Three classic film growth modes . . . . .	4
2.2 Energy sub-bands of a metallic thin film . . . . .	7
2.3 Quantum-well states of a metallic thin film . . . . .	8
2.4 The coarsening behavior of Pb islands in Pb/Si(111) . . . . .	10
2.5 Band structure of bulk Ag . . . . .	13
2.6 Ag island height histogram in Ag/Si(111)7x7 . . . . .	14
3.1 Momentum transfer . . . . .	17
3.2 The N-slit interference function . . . . .	20
3.3 A typical crystal truncation rod . . . . .	21
3.4 The hexagonal coordinate system . . . . .	25
3.5 Crystal truncation rods of Ag/Si(111) . . . . .	27
4.1 Structural model of Ag/Si(111) . . . . .	31
4.2 2D and 3D top view of Si 7x7 structure . . . . .	37
4.3 Two conventions of the Si hexagonal coordinate system . . . . .	38
4.4 Side view of the Si 7x7 layers . . . . .	39
4.5 The width of transverse scans for specular reflectivity . . . . .	43

4.6	Specular reflectivity of 0.3 and 0.45 ML Ag . . . . .	46
4.7	Specular reflectivity of 0.9 ML Ag . . . . .	47
4.8	Specular reflectivity of 1.8 ML Ag . . . . .	48
4.9	Summary of coverage dependence study . . . . .	48
4.10	Temperature dependence specular reflectivity studies of 1.8 ML coverage	50
4.11	Island height distribution from 1.8 ML temperature dependence study	50
4.12	Comparison of specular reflectivity studies of 0.9 ML coverage . . . .	51
4.13	Specular reflectivity measurements for annealing experiments . . . . .	51
4.14	Specular reflectivity of 21.6 ML Ag film . . . . .	54
4.15	Fringes around the Ag Bragg peak and the film profile for 21.6 ML .	55
4.16	Effect of the binomial model parameters . . . . .	56
4.17	Hayden's fit to the 21.6 ML data and his film profile . . . . .	59
4.18	Low wetting layer coverage and density . . . . .	60
4.19	Specular reflectivity fitting parameter table part 1 . . . . .	62
4.20	Specular reflectivity fitting parameter table part 2 . . . . .	63
4.21	Specular reflectivity fitting parameter table part 3 . . . . .	64
4.22	The effect of Ag lattice expansion . . . . .	67
4.23	Si seventh-order peak and Ag FCC peak during deposition . . . . .	68
4.24	Si $(\frac{n}{7}, \frac{0}{7})_H$ fractional order peaks during deposition . . . . .	70
4.25	Si $(\frac{0}{7}, \frac{n}{7})_H$ fractional order peaks during deposition . . . . .	71
4.26	Si fractional order peaks after normalization . . . . .	72
4.27	Comparison between specular reflectivity and truncation rod . . . . .	74
4.28	Ag(1,0) <sub>H</sub> rod . . . . .	76
4.29	Azimuthal scan in the HK plane . . . . .	78

4.30	In-plane orientational disorder of Ag islands . . . . .	79
4.31	Radial scan on the Ag Bragg peak and satellite peak . . . . .	80
4.32	0 and 15.8 degree Coincidence Site Lattice of Ag on Si . . . . .	82
4.33	14.4 and 16.6 degree Coincidence Site Lattice of Ag on Si . . . . .	83
4.34	The coincidence of Ag supercells with Si 1a layer . . . . .	84
4.35	Surface energy calculation for Ag nanofilm . . . . .	87
5.1	Constant difference between the mean and the variance . . . . .	91
5.2	Ag(111) surface free energy vs layer height . . . . .	92
5.3	Energy barriers deduced from the average island height . . . . .	93
5.4	The shifted Poisson distribution and the Binomial distribution model . . . . .	95
5.5	The effect of the modified Poisson distribution model . . . . .	103
5.6	Normalized island height distribution . . . . .	105
5.7	Parameters for the Modified Poisson distribution model . . . . .	106
6.1	Strain in homoepitaxial film growth . . . . .	110
6.2	Surface morphology due to deposition angles . . . . .	112
6.3	Kim's model with large vacancy clusters for diffuse scattering . . . . .	114
6.4	Diffuse intensity of homoepitaxial Ag films . . . . .	116
6.5	The integrand in numerical calculation . . . . .	124
6.6	Top view of the Cu/Cu(100) MD simulaton . . . . .	127
6.7	Displacement calculated from the Cu/Cu(100) MD simulation . . . . .	129
6.8	Magnitude of layer displacement calculated from the simulation . . . . .	130
6.9	Layer displacement vs layer height . . . . .	131
6.10	A typical example of overhanging and surface roughness . . . . .	134

6.11	Big in-plane displacement from a big hollow . . . . .	137
6.12	The local displacement field near a hollow . . . . .	138
6.13	An example of Finite Size Effect . . . . .	141
6.14	An attempt to do averaging over randomly chosen small volumes . . .	143
6.15	Gaussian weighted averaging to smooth out oscillations . . . . .	145
6.16	The effect of the location of a single defect in the system . . . . .	147
6.17	Random defect model . . . . .	149
6.18	How defects affect the Bragg peak . . . . .	151
6.19	Intensities calculated from random defect model . . . . .	153
6.20	Random defect model results compared with Kim's results . . . . .	154
6.21	The effect of system size for the random defect model . . . . .	156
A.1	Six-circle and psi-circle diffractometers . . . . .	159
A.2	Scattering angle calculation . . . . .	163
A.3	Sample active area and beam footprint . . . . .	165
A.4	Detailed sample active area calculation . . . . .	168

## ABSTRACT

When metals are synthesized on the nanoscale, new physics can arise in the growth process as quantum confinement of the conduction electrons, known as quantum size effects, can lead to preferred heights of metallic nanoscale islands. Despite a significant amount of prior research, there has been a poor understanding of the growth behavior of the simple noble metal, Ag, on the Si(111)7x7 substrate and researchers have been unable to connect its growth morphology to quantum size effects. This dissertation investigated the growth of Ag on Si(111)7x7, in situ and in ultra-high vacuum, using synchrotron x-ray scattering. Because of the unique ability of this technique to explore the structure of a buried interface on the atomic scale, these studies led to a clear understanding of the role of quantum size effects in the growth behavior of this system.

The studies address the epitaxial relationship between Ag and the substrate as well as the transition from the wetting layer to the growth of nanoscale islands. It is found that islands have a minimum thickness of three Ag atomic layers, which is in contrast to the bilayer on top of a wetting layer that has been reported in previous scanning tunneling microscopy studies. Ag islands are found to form after the completion of the Ag/Si(111)7x7 wetting layer and they convert the underlying wetting layer into the FCC structure of the island. The observed preference of the Ag islands is explained by the energy per area of the island, which derives from quantum confinement effects, and its two phase coexistence with the wetting layer. For thicker island heights, it is found that the distribution of island heights reflect the minimum thickness of three layers. The height fluctuations are observed to exhibit a Poisson-like distribution where only the low heights in the fluctuation spectrum deviate from

a Poisson distribution. A model of the height distribution is presented.

Techniques for exploring buried nanoscale vacancy defects in metals using diffuse x-ray scattering were also explored in this dissertation. Strain fields due to nanoscale vacancy clusters located below a surface were explored through analytical modeling of elastic displacements as well from results of accelerated molecular dynamics simulations. A method for numerically calculating diffuse scattering from nanoscale vacancy clusters was also explored.

As new technologies continue to exploit thin-film metals on nanoscale dimensions, this investigation provides important new understanding about how metals grow on the nanoscale.

# Chapter 1

## Introduction

As the physical size of the structure approaches the atomic scale, the properties of the material become much different from the bulk. A bulk material should have constant physical properties regardless of its size, whereas for nanoscale materials, due to the vast increase of the surface area to volume ratio, the mechanical, electrical, magnetic, optical, chemical and other properties of the material may change dramatically depending on its size. In addition, new quantum mechanics effects come into play because the length scale comes close to the de Broglie wavelength of electrons.

Due to the new properties at nanoscale, thin films (or islands) with certain heights could be energetically favored over others. This provides possibilities to control the film growth at nanoscale to achieve the desired functionalities with quantum engineering. Films with strongly preferred (or “magic”) heights were observed in epitaxial systems like Ag/GaAs(110)[3, 4], Ag/Si(111)[5], Pb/Si(111)[6, 7], Ag/Fe(100)[8], Pb/Cu(111)[9], Pb/Ge(111)[10], and recently In/Si(111)[11]. This magic height phenomenon is explained by the “electronic growth” (or “quantum growth”) model[12]

and is attributed to the quantum size effect (QSE)[13, 14], which arises from the electron confinement and predicts preferred island heights in the equilibrium state.

Ag is a simple noble metal which is a good test bed to study the new quantum property before we move to more complicated systems. Ag/Si(111)7x7 is a metal on semiconductor system which shows a preferred island height during the initial growth of the islands [5, 15, 16, 17]. There is some inconsistency in the literature whether the island height preference repeat after the initial growth[16, 17]. It has been difficult to connect the growth behavior to QSE, and the reason for minimum preferred island height remained a puzzle.

X-ray scattering is an ideal in-situ tool to investigate the formation and the evolving behavior of the film during and after the deposition. Most of the epitaxial thin film growth experiments are measured with scanning probes such as scanning tunneling microscopy (STM) or atomic force microscopy (AFM), which are good at obtaining information from the surface but cannot detect buried interfaces. X-ray scattering is an unique tool that it can detect both the surface and the subsurface, so it is ideal for obtaining the statistical information about the buried interfaces in addition to the whole surface. The information about defects in the film could also be obtained from x-ray scattering measurements.

In this dissertation, chapter 2 introduces the detailed background about QSE in Ag/Si system. Chapter 3 quickly goes through the x-ray scattering theory. Chapter 4 shows our in-situ x-ray scattering results for Ag/Si and the analysis. Chapter 5 talks about an interpretation of the island height distribution of Ag/Si. Unrelated with Ag/Si, chapter 6 shows the attempt to explain the diffuse scattering results for homoepitaxial Ag.



# Chapter 2

## Background

### 2.1 Film growth modes[1]

Depending on the interaction strength between the film and the substrate, there are three classical thin film growth modes: layer-by-layer growth, island growth, and layer-plus-island growth, which are shown in Fig. 2.1. When the atoms in the film are more strongly attracted to the substrate than they are to themselves, the atoms are going to form a complete layer before they start the next one. This is called the layer-by-layer or Frank-van der Merwe (FM) growth mode. In the exact opposite case, when the atoms in the film are more strongly attracted to each other than they are to the substrate, the atoms are going to cluster together, resulting in 3-dimensional islands on the bare substrate. This is called the island or Volmer-Weber (VW) growth mode. In the intermediate case, there is initial attraction between the film and the substrate so that a complete wetting layer is formed on the substrate,

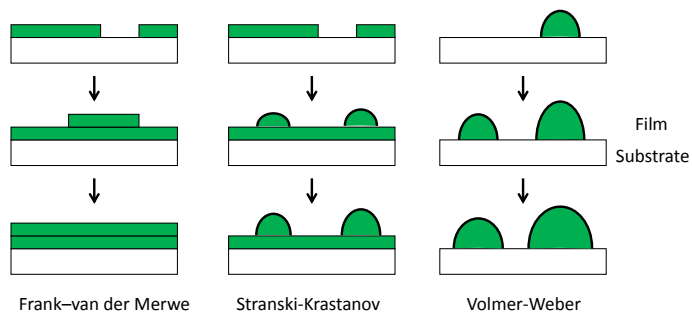


Figure 2.1: Cross-section views of the three classic thin-film growth modes.

then the attraction goes away and island clusters. This is called the layer-plus-island or Stranski-Krastanov (SK) growth mode.

In the epitaxial film growth, FM growth modes usually occur in homoepitaxy where the film and the substrate are the same material. SK and VW growth modes are the most common growth modes for metals grown on semiconductors. However, a different growth mode has been observed experimentally for metals on semiconductors. In 1996, Smith et al.[4] reported a novel growth behavior of Ag on GaAs following a two-step process, deposition at low temperature then annealed to room temperature. The Ag atoms form tiny nanoclusters at low temperature, and they form an atomically smooth film with a thickness of 6 monolayers (ML) after annealing. If the deposition amount is less than 6 ML, the film is still 6 layers high but with holes exposing the substrate. This stability of 6 ML Ag film is explained by the “electronic growth” (or “quantum growth”) model from Zhang et al.[12] that relates

quantum size effect to thin film formation energy.

## 2.2 Quantum size effect

The de Broglie wavelength of electrons near the Fermi level (so-called Fermi wavelength) is comparable to the lattice spacing for most metals. If the thickness of a metal film becomes sufficiently small (on the order of a few atomic layers), the motion of the nearly free electrons along the surface normal direction is confined in a small dimension, and the energy spectrum splitting between sub-bands[13, 14] becomes large compared with  $k_B T$  thus could not be considered continuous. This discretization can lead to oscillatory dependence of the film energy on its thickness, indicating certain layers are more energetically favored than others. As the result the electron confinement energy becomes an important consideration and it can dictate the stability of the film.

As early as 1989, the influence of QSE on film growth mechanics has been observed experimentally[18]. A lot of experimental and theoretical papers are published on QSE. Some review articles about QSE could be found at Ref#[19, 20], and review articles about the energy states associated with QSE could be found at Ref#[21, 22].

### 2.2.1 Particle in a box

The idea of QSE can be understood from the simple quantum mechanical particle in a box model. When the electrons are confined vertically, the substrate-film interface at  $z=0$  and film-vacuum interface at  $z=D$  become the wall barriers of the one dimensional

square well. In a thin film with thickness  $D$ , the condition to form standing waves is

$$D = n \frac{\lambda_F}{2}, \quad n = 1, 2, 3, \dots, \quad (2.1)$$

where  $\lambda_F$  is the wavelength of the free electrons at the bulk Fermi level. From a *simple and naive* point of view, if the following condition is met

$$Nd_0 \approx n \frac{\lambda_F}{2}, \quad N = 1, 2, 3, \dots, n = 1, 2, 3, \dots, \quad (2.2)$$

where  $N$  is the integer number of atomic layers assumed to have the same thickness  $d_0$ , the  $N$ -layer film should be stable.

### 2.2.2 Electron band filling

Here we take a detailed look on how to calculate and predict the preferred layer height. Considering the film (or islands) as electron clouds with large in-plane dimension  $L$ , but small perpendicular height  $D$ , we could separate the electron energy calculation into in-plane and perpendicular components.

$$\varepsilon = \frac{\hbar^2}{2m_{//}}(k_x^2 + k_y^2) + \frac{\hbar^2}{2m_z}k_z^2, \quad (2.3)$$

where  $m_{//}$  and  $m_z$  are the effective masses in-plane and perpendicular,  $k_x$ ,  $k_y$ , and  $k_z$  are the momentum wave vector components along different directions.

The dimension  $L$  in-plane is sufficiently large ( $L$  still  $> 100$  nm for islands), so the Born Von-Karman periodic boundary condition can be applied. In the perpendicular direction, periodic boundary condition is not valid due to the small size (several

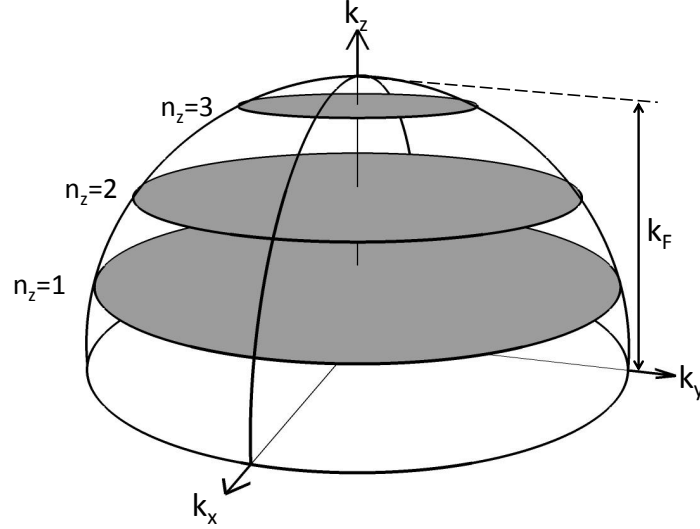


Figure 2.2: Occupied electron states in thin metal films. The states are continuous along  $k_x$  and  $k_y$  directions but discrete along  $k_z$  direction.

atomic layer  $\sim 1$  nm), particle in a box boundary condition is applied. We get

$$k_{x,y} = \frac{2\pi}{L}n_{x,y}, \quad k_z = \frac{\pi}{D}n_z, \quad n_{x,y} = 0, \pm 1, \pm 2, \dots, \quad n_z = 1, 2, 3, \dots, \quad (2.4)$$

where  $n_x, n_y$  are integers,  $n_z$  is a positive integer. Because  $L$  is large, we can treat  $k_x$  and  $k_y$  as continuous numbers, whereas  $k_z$  is discrete. The occupied electron states are situated in Fermi discs as shown in Fig. 2.2.

The discrete energy levels in the perpendicular ( $z$ ) direction are associated with the so-called quantum-well states (QWS)[21]. As shown in Fig. 2.3, if we plot the dispersion curve  $E_z$  vs  $k_z$ , it can be seen that as the film thickness  $D$  increases, the spacing between two nearby QWS which is  $\frac{\pi}{D}$  decreases and new QWS will move across the Fermi level. The film energy oscillates as a function of the film thickness. Every time an unoccupied QWS crosses the Fermi level, the film energy will start a

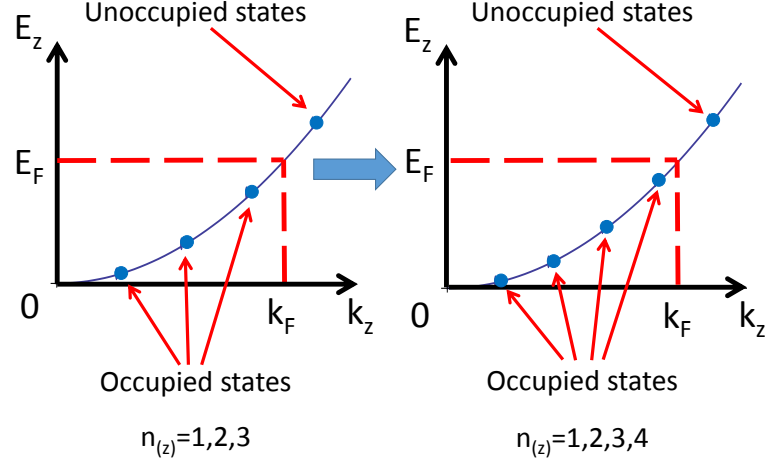


Figure 2.3: Quantum-well states come across the Fermi level as the film thickness increases,  $E_F$  and  $k_F$  are the energy and the wave vector of free electrons at the bulk Fermi level.

new oscillation, thus the film should be stable around the new local minimum of the film energy. Detailed calculations can be found at Wu and Zhang[23].

In reality, the substrate-film interface and film-vacuum interface are not infinite barriers as treated in the square well, which means electronic wave functions can leak through the barriers. A phase shift  $\phi$  is introduced to count for the finite barriers, the effect of different substrates can also be accounted by different phase shifts, and the quantization condition becomes[24]

$$2k_z N d_0 + 2\phi = n2\pi, \quad N = 1, 2, 3, \dots, n = 1, 2, 3\dots \quad (2.5)$$

The periodicity for the QWS crossing the Fermi level can be calculated from the above equation as  $\Delta N = \frac{\pi}{k_F d_0}$ . Since all the bands are translated into the First Brillouin Zone using the reduced zone scheme, if the free electron Fermi wave vector

$k_F$  lies beyond the First Brillouin boundary  $k_{BZ}$ , we need to count the effective wave vector properly. For example, Pb has the s band filled and the Fermi level lies within the p band, when we calculate the periodicity of QWS crossing the Fermi level along the Pb(111) direction, we need to take into account that the effective wave vector folds back from the L point,  $k_{BZ} - k_{Eff} = k_F - k_{BZ}$ , with  $k_{BZ} = k_{111}$ , we get  $k_{Eff} = 2k_{111} - k_F$ . Take  $d_0=2.858\text{\AA}$ ,  $k_{111} = \pi/d_0 = 1.099\text{\AA}^{-1}$ ,  $k_F = 1.58\text{\AA}^{-1}$ ,<sup>1</sup> we get  $\Delta N = 1.78$  for Pb(111), which predicts the energy of thin Pb(111) films oscillates with a period of close to two layers.

## 2.3 Preferred island heights in Pb/Si

Pb/Si(111) is a widely studied QSE system which exhibits pancake shaped islands with flat tops, steep edges and strongly preferred heights. At low coverage, the dominant island height of Pb/Si(111)7x7 is observed to be 4 or 5 ML, 7 ML and 9 ML depending on the deposition temperature and coverage[7]. QSE in Pb is very robust that it produces atomically flat films all the way up to above 20 ML, in Pb/Si(111)7x7 as well as Pb/Si(111) $\sqrt{3}\times\sqrt{3}$ . The observed stable heights are 5, 7, 9, 11, 13, 14, 16, 18, 20 ML above the wetting layer[10]. This observed bilayer selection agrees with the thickness-dependent energy calculations that predict oscillatory stability. And the even-odd crossover phenomenon from 13 ML to 14 ML is the result of the slightly incommensurate beating[26] between the interlayer spacing and the Fermi wavelength ( $\Delta N = 1.78$  not 2).

The prediction of the preferred island heights with bilayer stability from QSE

---

<sup>1</sup>This Fermi wave vector is taken from Ref#[25], if different experimental Fermi wavelength or wave vector is used, it may give slightly different  $\Delta N$ s.

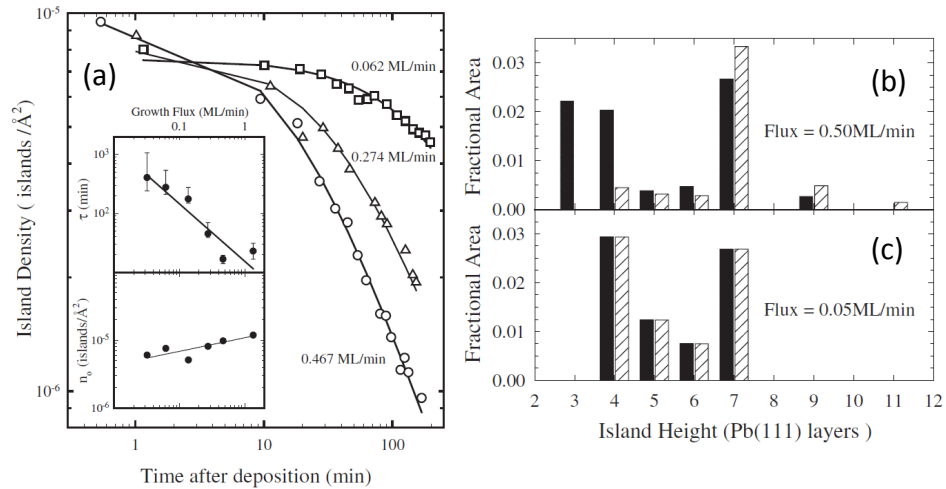


Figure 2.4: (a) Island density vs time demonstrates the breakdown of scaling for coarsening behavior of Pb/Si(111): The curves do not approach each other at long times. These data were obtained from x-ray diffuse scattering measured after the deposition of 1.2 ML of Pb at 208 K for various deposition fluxes. (b) and (c) STM analysis of the island height histogram of 1.6 ML Pb grown at 230 K. The Pb atoms were deposited using a fast deposition rate for (b) and a slow deposition rate for (c). The behavior of islands  $\sim$ 5 minutes (black) and 74 minutes (cross-hatched) after the deposition are different in the 2 cases with different deposition rate. Reprinted with permission from Jeffrey et al.[27]. Copyright 2006 by the American Physical Society.



conditions assumes that the islands attain their equilibrium configuration. In epitaxial growth, that is not usually achieved, so the ability to see the magic heights is surprising. Our group looked further into this question by performing coarsening experiments where the island densities were measured as a function of time just after the islands were grown to study how the islands with non-preferred height transform into islands with preferred heights. We observed that the initial oscillatory stability eventually led to one most stable height of 7 ML in Pb/Si(111)7x7.

Our group showed that in Pb/Si the island densities measured at different flux rates do not approach each other at long times[27], which is in sharp contradiction to the established Ostwald ripening prediction that island densities converge at long times. As shown in Fig. 2.4b and c, with fast deposition rate, a large number of non-preferred islands is created and they decay quickly, whereas with slow deposition rate, the island distribution is closer to the equilibrium state and it does not change much. The coarsening behavior is different depending on the deposition flux, and the relaxation time is inversely proportional to the flux. The coarsening rate of Pb islands on Si(111)7x7 is found to be orders of magnitude (about a factor of 1000) faster[28] than the expected value from large Pb crystals. This anomalously fast relaxation rate might explain why QSE effect is so robust in the Pb(111) systems: the kinetic of Pb atoms are so great that they could reach the quasi-equilibrium state very fast, so the island height matches what is predicted from the equilibrium state QSE conditions.

But there still remains unresolved mysteries in Pb/Si. What is the reason for the anomalously fast relaxation rate? Why 7 ML island is the most stable island? And the coarsening behavior is still not completely understood.

## 2.4 Preferred island heights in Ag/Si

### 2.4.1 Bilayer preference

The interest of QSE in the Ag/Si(111)7x7 system started from 1998 when Huang et al.[29] reported that atomically flat pinhole-free Ag films could be formed when the deposited material exceeded 6 ML, whereas multilayer pits appeared when the deposited material was less. The film growth was done in a two-step process where the material was first deposited at low temperature (LT), then annealed to room temperature (RT). (This behavior is similar to the Ag/GaAs[4].) Later Gavioli et al.[5] reported that following the two-step deposition process, Ag adatoms formed 2 ML height flat plateaus above the wetting layer instead of commonly observed pyramids at low coverage. The plateaus grew laterally without changing their height as the coverage increased.

The bilayer preference in the initial growth of Ag/Si(111)7x7 was observed not only in a two-step deposition process, but also in single step RT deposition process[15, 16, 17]. Goswami et al.[16] reported that the bilayers were preferred even at higher coverage, but Unal et al.[17] reported that the initial bilayer preference did not repeat and all layer heights greater than a bilayer had been observed to occur in single-layer increments. Since STM could only look at a small region on the whole sample, x-ray scattering would be ideal to look at the statistical average over the whole sample surface and verify whether there is more bilayer preference beyond the first 2 layers.

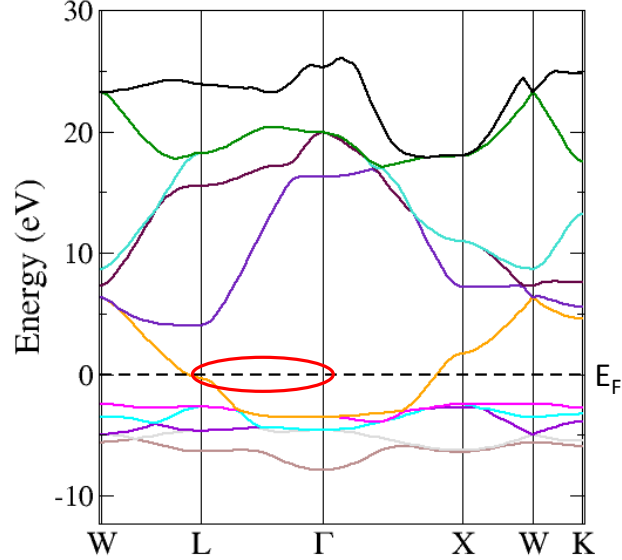


Figure 2.5: The band structure of bulk Ag. As indicated by the red circle, the Fermi level lies within the band gap along the [111] L- $\Gamma$  direction. The band structure calculation figure is copied from internet (<http://exciting-code.org/ag-bandstructure>).

### 2.4.2 Is the preference due to QSE?

If we use the previous equation  $\Delta N = \frac{\pi}{k_F d_0}$ , and put in Ag(111) parameters  $d_0 = 2.361 \text{ \AA}$ ,  $k_{111} = \pi/d_0 = 1.331 \text{ \AA}^{-1}$ ,  $k_F = 1.2 \text{ \AA}^{-1}$ ,<sup>2</sup> we get  $\Delta N = 1.11$  for Ag(111), which is close to 1 layer and does not give bilayer selection. In fact as shown in Fig. 2.5, the electronic structure of bulk Ag along [111] L- $\Gamma$  direction has a gap at the Fermi level. There is be no free electrons to form the standing waves, so electron confinement should not be the reason for the bilayer height selection.

Several STM groups measured the height of the first Ag bilayer as  $5.3 \text{ \AA}$  [5, 16, 17], whereas the conventional Ag lattice constant along (111) direction is  $4.72 \text{ \AA}$  for bilayer spacing. Fig. 2.6 shows the STM measurement of Unal et al. [17]. They claimed that the 12% expansion would shift the Fermi energy level below the band gap in

<sup>2</sup>This Fermi wave vector is also taken from Ref#[25].

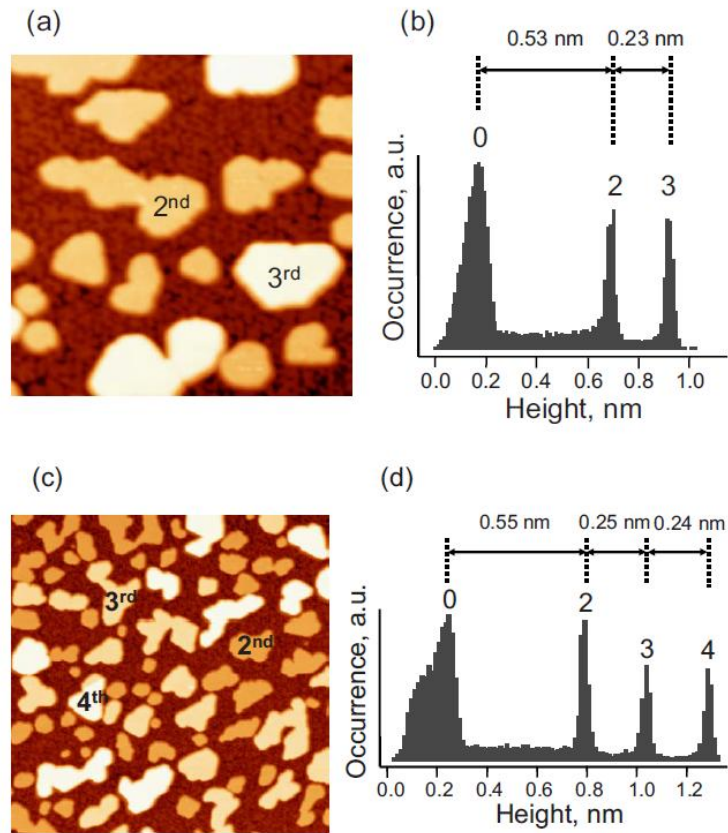


Figure 2.6: Parts (a) and (c) are STM images of Ag/Si(111) in areas of  $100 \times 100 \text{ nm}^2$  and  $250 \times 250 \text{ nm}^2$ , respectively. Parts (b) and (d) are height histograms corresponding to panels (a) and (c), respectively. In panels (a) and (b), the Ag coverage is 1.2 ML, and in (c) and (d), it is 1.8 ML. The wetting layer is marked as 0 in the height histograms. Reprinted with permission from Unal et al.[17]. Copyright 2010 by the American Physical Society.

Ag(111) direction, thus allowing electron confinement to control the height selection, and enabling the oscillatory energy behavior. The lattice expansion was observed to vanish for islands higher than 2 layers, therefore they suggested that when the Ag film grew thicker and the lattice expansion went away, the height selection also vanished.

X-ray scattering is capable of detecting layers underneath the surface, so it would be useful and important to verify the expansion effect claimed by the paper. We are going to address the following issues that are important to understand crystal growth: island height distributions, wetting layer structure, interlayer spacings in the islands, and the interface between the islands and the substrate.

# Chapter 3

## Scattering Theory

### 3.1 X-ray diffraction background[2]

X-ray diffraction is used to determine the atomic structure of a crystal[30]. X-rays scatter from the electrons of the atoms and they exhibit diffraction effects from the periodic ordering of the atoms. By measuring the angle and the intensity of the diffracted x-ray beam, we could get information about the electron distribution of the sample.

The x-ray intensity we measure is proportional to the square of the x-ray wave amplitude. We start from the amplitude scattered from an electron. The Thompson formula[30, 31] describes the amplitude of the wave  $A_1$  that comes from a scattering electron at  $r_e$ , as a function of the amplitude of the incoming wave  $A_0$ , assuming a dipole approximation,

$$A_1 e^{-i\vec{k}_f \cdot \vec{r}_e} = A_0 \frac{e^2}{mc^2} \frac{1}{R_0} e^{-i\vec{k}_i \cdot \vec{r}_e}, \quad (3.1)$$

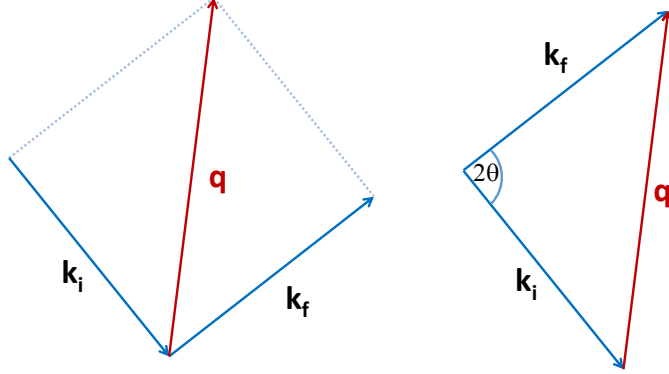


Figure 3.1: The incident and exit wave vectors  $\vec{k}_i$  and  $\vec{k}_f$ , the momentum transfer is defined as  $\vec{q} \equiv \vec{k}_f - \vec{k}_i$ .

where  $e$  and  $m$  are the electrons charge and mass,  $c$  is the speed of light,  $R_0$  is distance from the sample to the detector.

Now we introduce the momentum transfer  $\vec{q}$ , which is the vector difference between the incoming wave vector  $\vec{k}_i$  and outgoing wave vector  $\vec{k}_f$ . Since  $|\vec{k}_i| = |\vec{k}_f| = |\vec{k}| = 2\pi/\lambda$  in elastic scattering, where  $\lambda$  is the x-ray wave length, we can get the Bragg's law,

$$|\vec{q}| = 2 |\vec{k}| \sin \frac{2\theta}{2} = \frac{4\pi}{\lambda} \sin \theta. \quad (3.2)$$

Utilizing the definition of momentum transfer  $\vec{q} \equiv \vec{k}_f - \vec{k}_i$ , we could rearrange equation 3.1 and get

$$A_1 = A_0 \frac{e^2}{mc^2} \frac{1}{R_0} e^{i\vec{q} \cdot \vec{r}_e}. \quad (3.3)$$

Using the kinematical approximation, we sum up the scattering amplitude of electrons. By integrating the electron density within an atom, we get the diffraction

amplitude from an atom,

$$\begin{aligned}
A_2 &= A_0 \frac{e^2}{mc^2} \frac{1}{R_0} \int \rho(\vec{r}') e^{i\vec{q} \cdot (\vec{R}_n + \vec{r}_j + \vec{r}')} d^3 r' \\
&= A_0 \frac{e^2}{mc^2} \frac{1}{R_0} f(q) e^{i\vec{q} \cdot (\vec{R}_n + \vec{r}_j)},
\end{aligned} \tag{3.4}$$

where the atomic form factor is defined as

$$f(q) = \int \rho(\vec{r}') e^{i\vec{q} \cdot \vec{r}'} d^3 r'. \tag{3.5}$$

In other words, the atomic form factor is defined as the Fourier transform of the electron density of one atom. Assuming spherical symmetry, the atomic form factor is independent of the directions.

By adding up all the  $N_c$  numbers of atoms in one unit cell of the crystal, we get the diffraction amplitude from a unit cell. If there are different species of atoms in the unit cell, we have to assign different atomic form factors  $f_j(q)$ .

$$\begin{aligned}
A_3 &= A_0 \frac{e^2}{mc^2} \frac{1}{R_0} \sum_{j=1}^{N_c} f_j(q) e^{i\vec{q} \cdot (\vec{R}_n + \vec{r}_j)} \\
&= A_0 \frac{e^2}{mc^2} \frac{1}{R_0} F(\vec{q}) e^{i\vec{q} \cdot \vec{R}_n},
\end{aligned} \tag{3.6}$$

where the structure factor of the unit cell is defined as

$$F(\vec{q}) = \sum_{j=1}^{N_c} f_j(q) e^{i\vec{q} \cdot \vec{r}_j}. \tag{3.7}$$

The final step is to add up all the unit cells over the whole crystal. For simplicity, assume the crystal to be block-shaped with  $N_1$ ,  $N_2$  and  $N_3$  unit cells along the three



crystal axes defined by the vectors  $\vec{a}_1$ ,  $\vec{a}_2$  and  $\vec{a}_3$ . Taking  $\vec{R}_n = n_1\vec{a}_1 + n_2\vec{a}_2 + n_3\vec{a}_3$ , we get the diffraction amplitude for the whole crystal,

$$A_4 = A_0 \frac{e^2}{mc^2} \frac{1}{R_0} F(\vec{q}) \sum_{n_1=1}^{N_1} \sum_{n_2=1}^{N_2} \sum_{n_3=1}^{N_3} e^{i\vec{q} \cdot (n_1\vec{a}_1 + n_2\vec{a}_2 + n_3\vec{a}_3)}. \quad (3.8)$$

Now we introduce the concept of reciprocal lattice space. We define the reciprocal lattice vectors  $\vec{b}_1$ ,  $\vec{b}_2$  and  $\vec{b}_3$  from the real space unit cell vectors  $\vec{a}_1$ ,  $\vec{a}_2$  and  $\vec{a}_3$ .

$$\vec{b}_1 = 2\pi \frac{\vec{a}_2 \times \vec{a}_3}{\vec{a}_1 \cdot (\vec{a}_2 \times \vec{a}_3)}, \vec{b}_2 = 2\pi \frac{\vec{a}_3 \times \vec{a}_1}{\vec{a}_2 \cdot (\vec{a}_3 \times \vec{a}_1)}, \vec{b}_3 = 2\pi \frac{\vec{a}_1 \times \vec{a}_2}{\vec{a}_3 \cdot (\vec{a}_1 \times \vec{a}_2)}. \quad (3.9)$$

Since the  $a_j$ s have the units of length( $\text{\AA}$ ), the  $b_j$ s have the units of inverse length( $\text{\AA}^{-1}$ ).

Then we could express the momentum transfer in reciprocal lattice units  $\vec{q} = h\vec{b}_1 + k\vec{b}_2 + l\vec{b}_3$ . With our definition,

$$\vec{q} \cdot \vec{a}_1 = 2\pi h, \vec{q} \cdot \vec{a}_2 = 2\pi k, \vec{q} \cdot \vec{a}_3 = 2\pi l. \quad (3.10)$$

The scattering intensity from the crystal becomes

$$\begin{aligned} I(\vec{q}) &= A_0^2 \frac{e^4}{m^2 c^4 R_0^2} |F(\vec{q})|^2 \sum_{n_1=0}^{N_1-1} \sum_{n_2=0}^{N_2-1} \sum_{n_3=0}^{N_3-1} e^{i\vec{q} \cdot (n_1\vec{a}_1 + n_2\vec{a}_2 + n_3\vec{a}_3)}|^2 \\ &= A_0^2 \frac{e^4}{m^2 c^4 R_0^2} |F(\vec{q})|^2 \frac{\sin^2(N_1\pi h)}{\sin^2(\pi h)} \frac{\sin^2(N_2\pi k)}{\sin^2(\pi k)} \frac{\sin^2(N_3\pi l)}{\sin^2(\pi l)}. \end{aligned} \quad (3.11)$$

$\frac{\sin^2(Nx/2)}{\sin^2(x/2)}$  is called the ‘‘N slit interference function’’ from its use in optics. An example of it is plotted in Fig. 3.2. If h,k,l are all integers,

$$I(\vec{q}) = A_0^2 \frac{e^4}{m^2 c^4 R_0^2} |F(\vec{q})|^2 N_1^2 N_2^2 N_3^2, \quad (3.12)$$

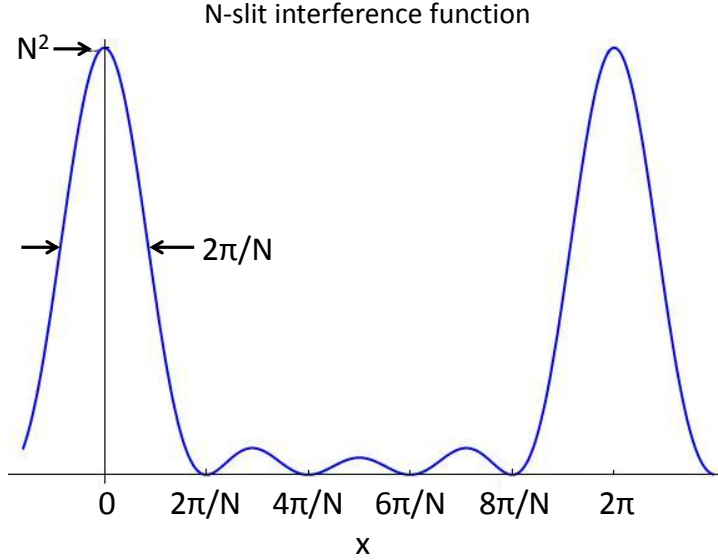


Figure 3.2: N-slit interference function shown for  $N=5$ . Primary maxima are spaced  $2\pi$  apart, and subsidiary maxima are spaced  $2\pi/N$  apart. There are  $N-2$  subsidiary maxima between two nearest primary maxima, and the width of the a primary maximum is  $2\pi/N$ .

these are the Bragg peaks.

From the property of N slit interference function, in the limit of  $N_j$ s are large, the Bragg peaks are sharp, and the intensities between the Bragg peaks are basically zero, we can treat the intensity as a periodic array of  $\delta$  functions.  $N_1$  and  $N_2$  along sample surface are really large. The substrate is thick compared with the thin film, but we no longer have x-ray coherence between the front and back surfaces. We are then left with coherence with only the top interface where now  $N_3$  along the surface normal is small. Therefore there is no in-plane intensities between the Bragg peaks, the only remaining intensities connecting the Bragg peaks are out of plane along the surface normal direction. This is called the crystal truncation rod (CTR).

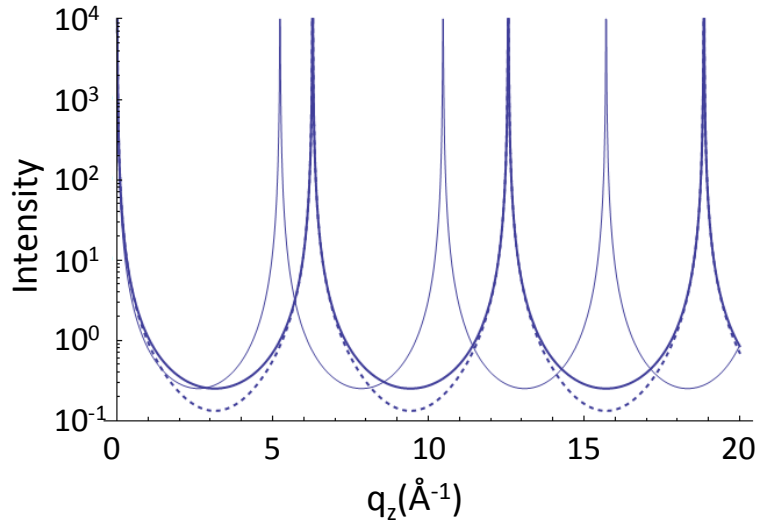


Figure 3.3: Crystal truncation rod of a semi-infinite simple cubic substrate. The solid thick curve shows the sharp Bragg peaks from lattice spacing  $d=1\text{\AA}$ , with no surface roughness. The solid thin curve shows the effect of a different lattice spacing  $d=1.2\text{\AA}$ , with no surface roughness. It can be seen that the different lattice constant shifts the Bragg peak positions. The dashed thick curve shows the effect of surface roughness  $\sigma=0.4\text{\AA}$ , with  $d=1\text{\AA}$ . It can be seen that the surface roughness only affect the intensities between the Bragg peaks.

## 3.2 Crystal truncation rod

We could study the properties of a crystal surface by measuring CTRs along the surface normal direction. The lattice spacing between the atomic layers could be determined from the positions of the Bragg peaks, and the surface roughness could be determined from the intensities between the Bragg peaks. Fig. 3.3 demonstrates the effects of a different lattice spacing and surface roughness on the CTR, the detailed calculations are given below.

If we take  $h, k$  only at integer values and take  $l$  as continuous values, we can do

the in-plane summation separately from the out-of-plane summation,

$$I(\vec{q}) = A_0^2 \frac{e^4}{m^2 c^4 R_0^2} |F(\vec{q})|^2 \left| \sum_{\vec{R}_{2D}} e^{i\vec{q} \cdot \vec{R}_{2D}} \sum_{n_3=0}^{N_3-1} e^{i\vec{q} \cdot (n_3 \vec{a}_3)} \right|^2, \quad (3.13)$$

where  $\vec{R}_{2D}$  is along the sample surface. The measured CTR Bragg intensity is a statistical average over the sample, we focus on the summation along surface normal direction and put everything else into the scale factor  $S_F = |A_0 \frac{e^2}{mc^2} \frac{1}{R_0} \sum_{\vec{R}_{2D}} e^{i\vec{q} \cdot \vec{R}_{2D}}|^2$ , we get

$$I(\vec{q}) = S_F |F(\vec{q})|^2 \left| \langle \sum_{n_3} e^{iq_z a_3 n_3} \rangle \right|^2, \quad (3.14)$$

where the average is taken over the whole sample surface.

Now we are going to show an example of CTR calculation for a single interface simple cubic crystal treated as a semi-infinite substrate with some roughness on top. With the amplitude term going through a transformation

$$A = \sum_{n=N}^{-\infty} e^{iq_z dn} = e^{iq_z dN} \sum_{n=0}^{-\infty} e^{iq_z dn'}, \quad (3.15)$$

where  $n'=n-N$ , we get the truncation term  $\frac{1}{1 - e^{-iq_z d}}$  for semi-infinite substrate from the infinite summation of power series. Here we use  $d$  for the layer spacing, and  $N$  is different at different  $\vec{R}_{2D}$  positions on the sample surface.

Now the average amplitude becomes

$$\langle A \rangle = \frac{\langle e^{iq_z dN} \rangle_N}{1 - e^{-iq_z d}} = \frac{V_0}{1 - e^{-iq_z d}}, \quad (3.16)$$

with  $V_0 = \langle e^{iq_z dN} \rangle_N$  as the term describing surface roughness. If we assume the

top surface follows a binomial distribution[32],

$$V_0 = \sum_{j=0}^M p_j e^{iq_z dj}, \quad p_j = \frac{M!}{j!(M-j)!} p^j q^{M-j}, \quad (3.17)$$

with  $\bar{N}$  as the average height,  $p = \bar{N}/M$ ,  $q=1-p$ ,  $M$  is the maximum layer number which is an integer. The variance of the distribution  $s^2 = Mpq = \bar{N}q$ , the height fluctuation  $\sigma = sd$ . Utilizing the definition  $\sum_{j=0}^M p_j = (p+q)^M = 1$ ,

$$\begin{aligned} V_0 &= \sum_{j=0}^M \frac{M!}{j!(M-j)!} p^j q^{M-j} e^{iq_z dj} = (pe^{iq_z d} + q)^M \\ &= [(1-q)e^{iq_z d} + q]^M = e^{iq_z dM} [1 + q(e^{-iq_z d} - 1)]^M. \end{aligned} \quad (3.18)$$

Taking the limit of  $p \rightarrow 1$  and  $q \rightarrow 0$ ,

$$\begin{aligned} \ln V_0 &= iq_z dM + M \ln[1 + q(e^{-iq_z d} - 1)] \approx iq_z dM + Mq(e^{-iq_z d} - 1) \\ &= iq_z dM + Mqe^{-iq_z d/2}(e^{-iq_z d/2} - e^{iq_z d/2}) \\ &= iq_z dM + Mq(\cos \frac{q_z d}{2} - i \sin \frac{q_z d}{2})(-2i \sin \frac{q_z d}{2}) \\ &= iq_z dM + \frac{s^2}{p}(-2i \sin \frac{q_z d}{2} \cos \frac{q_z d}{2} - 2 \sin^2 \frac{q_z d}{2}). \end{aligned} \quad (3.19)$$

At the end, we have the roughness term

$$|V_0|^2 = e^{-4s^2 \sin^2 \frac{q_z d}{2}} = e^{-4 \frac{\sigma^2}{d^2} \sin^2 \frac{q_z d}{2}}. \quad (3.20)$$

This is the surface roughness mentioned in Ref#[32, 33], and here we show the detailed derivation. Now we can calculate the CTR intensity which is proportional to  $|\langle A \rangle|^2$ , the result is plotted in Fig. 3.3.

### 3.3 The hexagonal coordinate system

Ag has face-centered cubic (FCC) structure, Si has diamond structure which consists of two inter-penetrating FCC. As shown in Fig. 3.4a, the atoms on the (111) planes of the FCC structure are hexagonally packed, it is convenient to use a hexagonal coordinate system. Taking the cubic lattice constant of the FCC structure as  $a_c$ , the distance between nearest neighbors in the (111) plane is  $a_H = \frac{a_c}{\sqrt{2}}$ , and the body diagonal of the cubic  $c_H = \sqrt{3}a_c$  is the spacing between four (111) planes ( $c_H = 3d_{111}$ ).

Now we set up our hexagonal coordinate system, we take  $\vec{a}_1$  and  $\vec{a}_2$  120 degrees apart on the (111) plane,  $\vec{a}_3$  is perpendicular to the (111) plane. Take the real space coordinates as shown in Fig. 3.4b, z axis is out of the page, and let one unit cell contain 3 layers of (111) planes, we get

$$\begin{aligned} \vec{a}_1 &= \frac{a_c}{\sqrt{2}}\hat{x}, \vec{a}_2 = \frac{a_c}{\sqrt{2}}\left(-\frac{1}{2}\hat{x} + \frac{\sqrt{3}}{2}\hat{y}\right), \vec{a}_3 = \sqrt{3}a_c\hat{z}, \\ \text{or} \quad \vec{a}_1 &= a_H\hat{x}, \vec{a}_2 = a_H\left(-\frac{1}{2}\hat{x} + \frac{\sqrt{3}}{2}\hat{y}\right), \vec{a}_3 = c_H\hat{z}. \end{aligned} \quad (3.21)$$

$\vec{a}_1 \cdot (\vec{a}_2 \times \vec{a}_3) = \frac{3}{4}a_c^3$ , from equation 3.9 we get

$$\begin{aligned} \vec{b}_1 &= \frac{2\pi}{a_c}\left(\sqrt{2}\hat{x} + \frac{\sqrt{2}}{\sqrt{3}}\hat{y}\right), \vec{b}_2 = \frac{2\pi}{a_c}\frac{2\sqrt{2}}{\sqrt{3}}\hat{y}, \vec{b}_3 = \frac{2\pi}{\sqrt{3}a_c}\hat{z}, \\ \text{or} \quad \vec{b}_1 &= \frac{2\pi}{a_H}\left(\hat{x} + \frac{1}{\sqrt{3}}\hat{y}\right), \vec{b}_2 = \frac{2\pi}{a_H}\frac{2}{\sqrt{3}}\hat{y}, \vec{b}_3 = \frac{2\pi}{c_H}\hat{z}, \end{aligned} \quad (3.22)$$

$\vec{b}_1$  and  $\vec{b}_2$  are 60 degrees apart in the reciprocal space. The momentum transfer can be expressed as  $\vec{Q} = H\vec{b}_1 + K\vec{b}_2 + L\vec{b}_3$ . The momentum transfer can be separated into in-plane and out-of-plane components,  $Q_{//} = \frac{2\pi}{a_H}\sqrt{\frac{4}{3}(H^2 + HK + K^2)}$  and  $Q_{\perp} =$

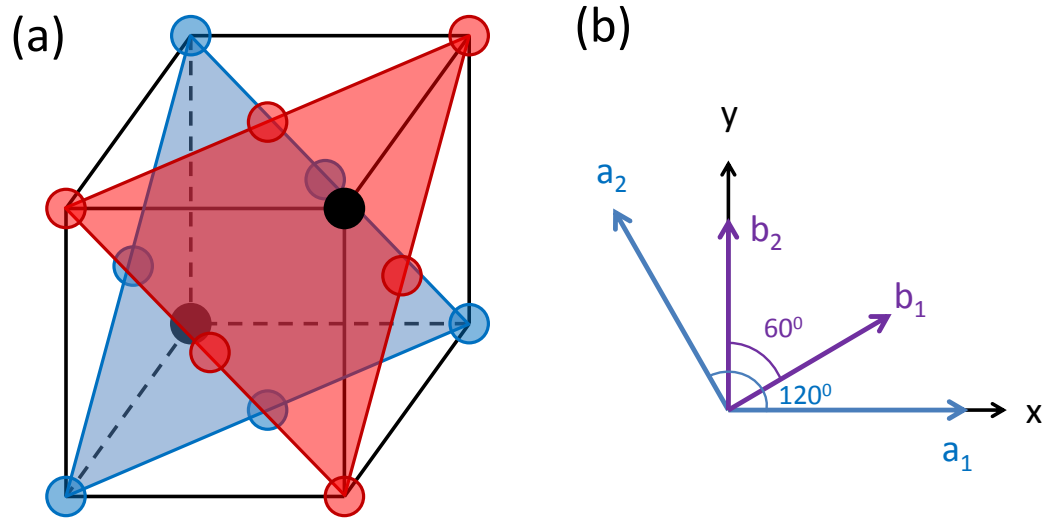


Figure 3.4: (a) The (111) plane in FCC structure, atoms are hexagonally packed on the plane. (b) The real space and reciprocal space hexagonal coordinate system, the real space in-plane axes are 120 degrees apart, and the reciprocal space in-plane axes are 60 degrees apart, the z axis is out of the page.

$$Q_z = \frac{2\pi L}{c_H}.$$

### 3.4 Different types of measurements

Now let us introduce the different types of x-ray scattering measurements that we performed. As stated in the previous section, there are Bragg peaks and the CTRs in the reciprocal space. If we have some incommensurate film on top of a substrate in real space (e.g. Ag/Si), there are scattering contributions from both the substrate and the film, and what we observe depends on where the measurement is done in the reciprocal space.

As shown schematically in Fig. 3.5, the CTRs are elongated along the direction perpendicular to the surface, indicated by the vertical lines. Bragg points are represented by green (light) and red (dark) spheres for substrate and film, respectively. Due to the incommensurate lattice constants of the substrate and the film, their respective rod do not overlap except for specular rod for which  $H=K=0$ . When we measure truncation rods, we can get information from only the film or the substrate.

Specular reflection, which is measured along the  $[0,0,L]_H$ , is an unique CTR measurement where the scattered amplitude from all the atomic layers of the substrate and film interfere and contribute to the specular rod.

Bulk truncation rods are measured at  $H,K$ =integer positions in the reciprocal space. When we look at reconstructed surfaces (e.g. Si 7x7), we have to look at bigger unit cells since a reconstructed surface has a larger periodicity than bulk. In this case, if we still use the bulk coordinate system, fractional order rods exist between the integer rods (in Si 7x7 case, the fractional order rods are seventh-order



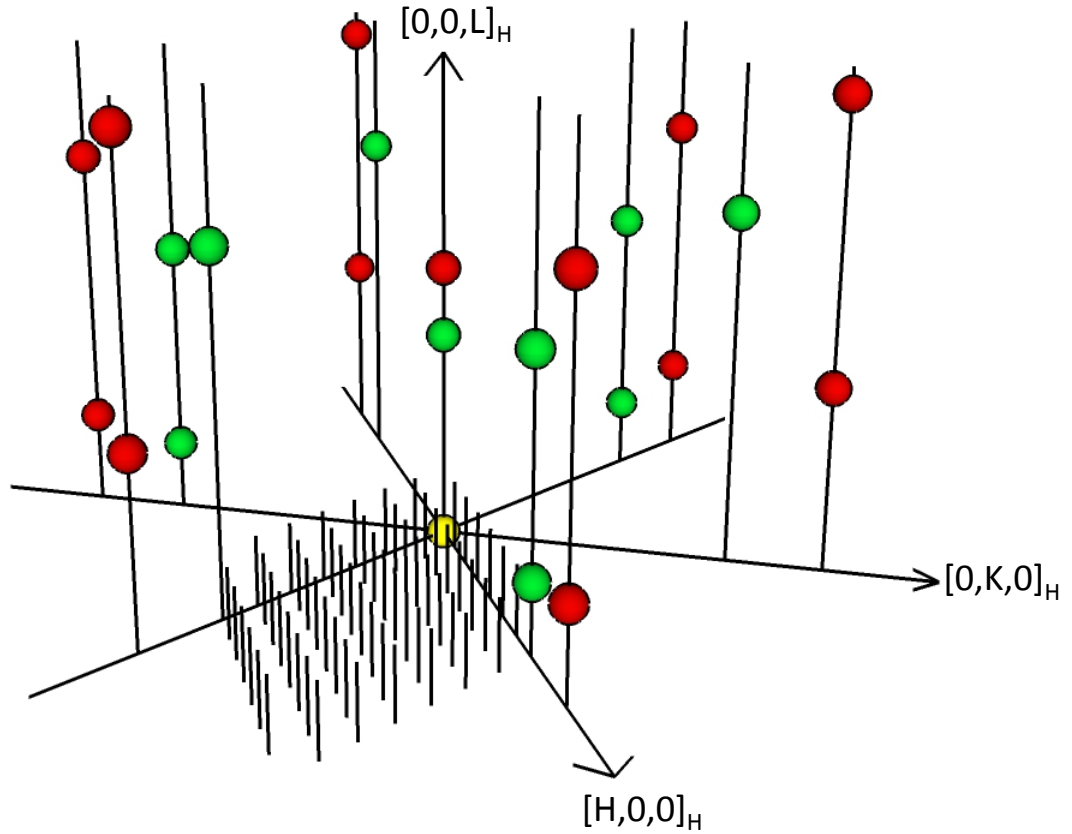


Figure 3.5: Schematic diagram illustrating the crystal truncation rods for Ag/Si(111) $7 \times 7$ , where the surface normal is along  $[0,0,L]_H$ . Bragg points are represented by green (light) spheres for Si and red (dark) spheres for Ag, from  $L=0$  to  $L=7$ . The specular reflectivity is along  $[0,0,L]_H$  whereas the truncation rods for the Si lattice and the incommensurate Ag lattice correspond to rods having non-zero  $H$  and/or  $K$ . A small subset of the fractional rods from the  $7 \times 7$  wetting layer, which have no Bragg points, are shown schematically in the region between  $[H,0,0]_H$  and  $[H,\bar{K},0]_H$ .

rods where  $H, K = \text{integer}/7$ ). There are no Bragg peaks in fractional order rods. Grazing incidence diffraction of the fractional order peaks, with  $L \sim 0$ , reveals in-plane structural information of the reconstructed surface.

# Chapter 4

## Ag/Si structure and morphology

X-ray scattering experiments were performed in situ using the surface scattering chamber (base pressure of  $1 \times 10^{-10}$  Torr) on a psi-circle diffractometer located at the 6IDC beam line at the Advanced Photon Source using a photon energy of 16.2keV.

The commercially-available 1mm-thick n-type Si(111) substrates used in these studies had a resistivity in the range of 1-10 $\Omega$ cm. Surface miscut angles were determined by x-ray reflectivity to be between 0.015-0.05°. The Si(111)7x7 surface was prepared by heating the Si(111) substrate to 1200°C for  $\sim$ 1 min and then slowly cooling from 1000°C for over 10 min to obtain the reconstructed surface. The quality of the surface was determined by transversely scanning the (8/7, 0, 0.1)<sub>H</sub> in-plane reflection. It exhibited an angular width of 0.02° to 0.05°, which corresponds to domain sizes between 8000Å and 3300Å. This large domain size, which is on the order of the step length given by the surface miscut angle, was routinely observed for all surfaces that were prepared as described above.

Ag was deposited on the clean Si(111)7x7 surface from a thermal evaporator

using a deposition rate of  $\sim 1.1 \text{ ML} \pm 0.1 \text{ ML/min}$ , where 1 ML is one monolayer of Ag(111) ( $1 \text{ ML} = 1.38 \times 10^{15} \text{ atoms/cm}^2$ ). The deposition rate was determined by a commercial quartz crystal oscillator that was calibrated from the period of x-ray intensity oscillations measured at the Ag specular anti-Bragg position during the layer-by-layer growth of Ag/Ag(001). The sample was cooled using a He closed-cycle refrigerator while heating employed a tungsten filament behind the sample. Heating for the purpose of preparing the Si(111)7x7 was performed by electron bombardment whereas maintaining the temperature during the scattering measurements ( $-50^\circ\text{C}$  to  $450^\circ\text{C}$ ) utilized radiative heating from the tungsten filament. The temperature was measured by a type K thermocouple connected to the bottom of the sample holder, which was also used for temperature control with a feedback system. The temperature stability was  $\pm 0.5^\circ\text{C}$  and the absolute temperature accuracy was better than  $\pm 10^\circ\text{C}$ .

## 4.1 Structural model for Ag/Si(111)7x7

Specular reflectivity and crystal truncation rods were measured to study the island height distributions of Ag grown on top of the Si(111)7x7. In-plane diffraction peaks were also measured to gain information about the wetting layer and the metal-substrate interface.

As described in chapter 3, in specular reflectivity measurements, the momentum transfer  $Q$  does not have in-plane component, so that  $Q = Q_\perp = \frac{2\pi L}{c_H}$ . In truncation rod measurements  $Q$  has both in-plane and out-of-plane component, we will directly use  $H$  and  $K$  to describe the in-plane momentum transfer.

In order to fit and analyze our data, we established a structural model for Ag/Si(111)7x7,

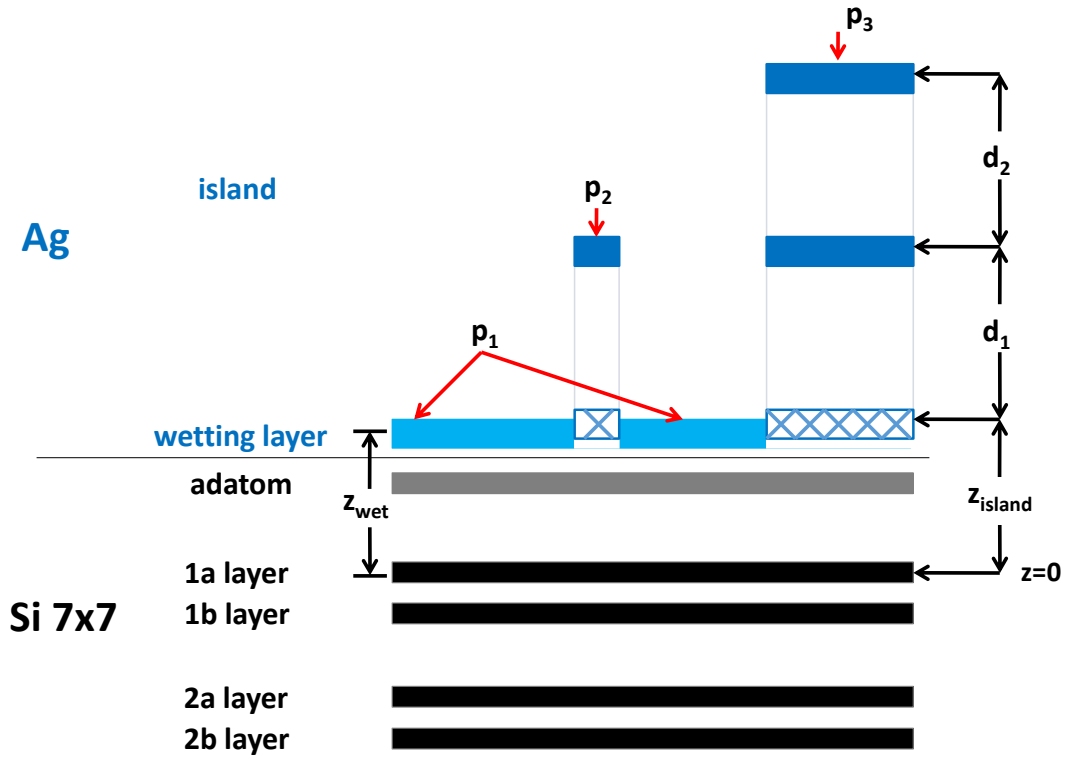


Figure 4.1: Side view showing the atomic layers used in the structural model for specular reflectivity and crystal truncation rods. The Ag wetting layer and Ag islands sit on the Si(111)7x7 structure; the bulk Si substrate is not shown.  $p_j$  is the fraction of the surface occupied by islands having a height  $j$ . The bottom atomic layer of the islands are cross-hatched to indicate that its structure is to be determined in the study.

shown in Fig. 4.1. Note that it is only necessary to discuss the vertical structure because a specular reflectivity measurement is sensitive to all of the atomic layers regardless of their lateral structure, whereas a crystal truncation rod measurement will detect only the atomic layers in Fig. 4.1 that have the in-plane symmetry of the rod being measured. In particular, we will investigate the rods that have the in-plane Ag FCC structure.

### 4.1.1 Specular reflectivity

The structural model assumes a semi-infinite bulk Si(111) substrate having the Si(111) 7x7 reconstructed surface, which consists of five Si layers: 2b, 2a, 1b, 1a and the ad-atom layer. Its structure has been described by Robinson et al.[34] and we utilize the atomic positions and layer occupancies from that work. The Ag wetting layer sits on top of the Si(111)7x7 at a position given by  $z_{wet}$ , which is measured relative to the position of the Si 1a layer. The Ag islands are also drawn as sitting on top of the Si(111)7x7 at a position given by  $z_{island}$ . However, because the structure of the first atomic layer in the island remains as a major question, it is drawn as cross-hatched and its relationship to the wetting layer and the islands will be explored in the experiments.

The spacings between the Ag atomic layers in the islands are given as  $d_n$  and the fraction of the surface occupied by islands of height  $j$  is given by  $p_j$ , which describes the island height distribution.  $p_0$  is the fraction of the surface that has bare Si(111)7x7,  $p_{wet}$  is the fraction of the surface covered by the wetting layer,  $p_1$  is the surface fraction of a single-layer island,  $p_2$  is the fraction of the surface that contains 2-layer islands, and etc. By definition all surface fractions add to unity,

$p_{wet} + \sum_{j=0}^{\infty} p_j = 1$ , which imposes a constraint on the values of the  $p_j$ s.

The x-ray scattering intensity is proportional to square of the total amplitude scattered from Ag film and Si substrate. Following equation 3.14, we can write the calculated scattering intensity corresponding to the structure given in Fig. 4.1 as  $I_{calc} = S_F |A|^2 |V_{sub}|^2$ , where  $S_F$  is a scale factor, A is the total amplitude and  $|V_{sub}|^2$  is the Si substrate roughness term.

The total amplitude is expressed as

$$A = \rho_{Si} f_{Si} A_{Si} + \rho_{Ag} f_{Ag} A_{Ag}, \quad (4.1)$$

where  $f_{Si}$  and  $f_{Ag}$  are the atomic form factors, including the thermal Debye-Waller factor  $e^{-M}$ , for Si and Ag, respectively. M is given by

$$M = \frac{6h^2T}{mk_B\Theta^2} \left[ \left( \phi(x) + \frac{x}{4} \right) \left( \frac{Q}{4\pi} \right)^2 \right], \quad (4.2)$$

where h is Planck's constant, T is the absolute temperature,  $k_B$  is Boltzman's constant, m and  $\Theta$  are the atomic mass and the Debye temperature. (We take 225K as the Ag Debye temperature and 645K as the Si Debye temperature.)  $x = \frac{\Theta}{T}$  and  $\phi(x)$  is a tabulated function from Ref#[35].  $\rho_{Ag}$  and  $\rho_{Si}$  are the bulk areal densities of Ag(111) and Si(111) planes;  $\rho_{Ag} = 1.763\rho_{Si}$  is used here.

For specular reflectivity,  $e^{i\vec{Q}\cdot\vec{r}}$  becomes  $e^{iQz}$ . Following the derivation in chapter 3.2, the Si substrate roughness term is expressed as

$$|V_{sub}|^2 = e^{-4 \frac{\sigma_{sub}^2}{d_{Si}^2} \sin^2 \frac{Qd_{Si}}{2}} = e^{-4 \frac{\sigma_{sub}^2}{d_{Si}^2} \sin^2 \frac{2\pi L}{6}}, \quad (4.3)$$

where  $d_{Si} = \frac{c_H}{3}$  is the Si(111) layer spacing, and  $\sigma_{sub}$  is the root-mean-square (RMS) roughness of the Si substrate.

The Si amplitude has contributions from bulk Si and from Si(111)7x7 reconstructed surface,  $A_{Si} = A_{Si}^{bulk} + A_{Si}^{DAS}$ .  $A_{Si}^{DAS}$  is given by the dimer-atom-stacking fault (DAS) model[36] of the reconstructed surface according to

$$A_{Si}^{DAS} = \sum_j \eta_j e^{iQz_j} e^{-\frac{1}{2}Q^2\zeta_j^2}. \quad (4.4)$$

$j$  sums over 5 layers (Si 2b, 2a, 1b, 1a, and adatom layer for  $j=1$  to 5) of the DAS model with each layer having a position  $z_j$ , an occupancy  $\eta_j$ , and a layer height fluctuation  $\zeta_j$ , given in Robinson and Vlieg[34].  $A_{Si}^{bulk}$  describes the amplitude from the semi-infinite bulk Si (one unit cell in diamond structure contains six atoms),

$$A_{Si}^{bulk} = \frac{\left(1 + e^{-\frac{i\pi L}{6}}\right) \left(1 + e^{-\frac{i2\pi L}{3}} + e^{-\frac{i4\pi L}{3}}\right)}{1 - e^{-i2\pi L}} e^{-iQz_{3a}}. \quad (4.5)$$

where  $z=0$  is located at the Si 1a layer so that  $z_{3a}$  is the starting point of the bulk Si below the reconstructed surface.

When Ag grows on the Si substrate, it commensurately wets the Si(111)7x7 up to a saturation coverage about 0.4 ML. In order to describe the areal density, we define  $\phi \equiv 1$  as the areal density of bulk Ag(111). We can allow the model to change the Ag wetting layer density  $\phi_{wet}$  (it should be smaller than 0.5[15]) and the Ag island density  $\phi_n$ . Although  $\phi_n = 1$  for the FCC layers in the island,  $\phi_1$  remains a question, as indicated by the cross-hatched first layer in Fig. 4.1:  $\phi_1 = \phi_{wet}$  if the islands grow on top of the wetting layer whereas  $\phi_1 = 1$  if the islands are FCC Ag all the way to the substrate. Because our studies find (will be shown later)  $z_{wet} \approx z_{island}$  and because



specular reflection does not distinguish the Ag 7x7 structure from Ag FCC,  $p_1$  will effectively be indistinguishable from  $p_{wet}$  in the specular reflectivity measurements so that  $p_{wet}$  will include  $p_1$  in this case.

With these considerations, the Ag coverage is given as

$$\Theta = p_{wet}\phi_{wet} + \sum_{j=1} p_j \sum_{n=1}^j \phi_n, \quad (4.6)$$

and the Ag specular scattering amplitude from all the Ag layers is given as

$$A_{Ag} = p_{wet}\phi_{wet}e^{iQz_{wet}}e^{-\frac{1}{2}Q^2\sigma_{wet}^2} + \sum_{j=1} p_j \sum_{n=1}^j \phi_n e^{iQz_n}e^{-\frac{1}{2}Q^2\sigma_j^2}. \quad (4.7)$$

The height of the individual atomic layer in Ag islands  $z_n$  is also measured relative to the position of Si 1a layer, where  $z_n$  is expressed as  $z_n = z_{island} + d_1 + d_2 + \dots + d_{n-1}$ . Therefore the model has the ability to change certain Ag layer spacing  $d_n$ , if necessary. If all Ag inter-atomic layer spacings are the same as the bulk value  $d_{Ag}=2.361\text{\AA}$ ,  $z_n$  will simplify to  $z_n = z_{island} + (n - 1)d_{Ag}$ .  $\sigma_{wet}$  and  $\sigma_j$  are the RMS variation in the vertical position of the wetting layer and the j-th island. For simplicity, we take  $\sigma_j = \sigma$  for all islands.

### 4.1.2 Crystal truncation rod calculation

Unlike in specular reflectivity calculation where we only need to keep track of the vertical positions of the atoms, in crystal truncation rod calculation we have to keep track of the in-plane positions in addition to the vertical positions of the atoms.

## Truncation rod for Si

Bulk Si has diamond structure, which consists of two inter-penetrating FCC structures. Because of the Si 7x7 reconstructed structure on top of the bulk Si, a bigger unit cell (in plane) is chosen. As shown in Fig. 4.2, layer 2a, 2b have the bulk Si structure that not affected by the reconstruction. Both layer 2a and 2b have 49 atoms in the unit cell (we have to exclude the leftmost column and bottom row of extra atoms for layer 2a in the drawing). Layer 1b has the dimer structure and misses one atom at the origin, therefore has 48 atoms in the unit cell (we also have to exclude the leftmost column and bottom row of extra atoms in the drawing). Layer 1a has the stacking fault and has only 42 atoms in the unit cell. The adatom layer only has 12 atoms[36]. The bulk Si has three-fold symmetry, as can be seen from the 2a, 2b layers; the adatom, 1a, and 1b layers have six-fold symmetry. As the result, bulk Si rods have three-fold symmetry as shown in Fig. 3.5, and Si fractional rods which come from the Si 7x7 structure have six-fold symmetry.

There are two conventions of defining the Si hexagonal coordinate system, the difference comes from the choice of directions for  $\vec{a}_1$  and  $\vec{a}_2$  in real space. We followed the convention from Ref#[37] which defines  $[3, 0, 0]_H = [\bar{4}, 2, 2]_c$ ,  $[0, 3, 0]_H = [\bar{2}, \bar{2}, 4]_c$ , and  $[0, 0, 3]_H = [1, 1, 1]_c$ . T. C. Chiang's group followed the other convention from Ref#[38] which defines  $[3, 0, 0]_H = [4, \bar{2}, \bar{2}]_c$ ,  $[0, 3, 0]_H = [2, 2, \bar{4}]_c$ , and  $[0, 0, 3]_H = [1, 1, 1]_c$ . If we ever have to compare results using these two different hexagonal coordinate conventions, the  $(H, K, L)_H$  coordinate in one convention is equivalent to the  $(\bar{H}, \bar{K}, L)_H$  in the other convention.

As shown in Fig. 4.3, when setting up the real space coordinate, by choosing the orientation of the unit cell (faulted half at left side or at right side), we could get

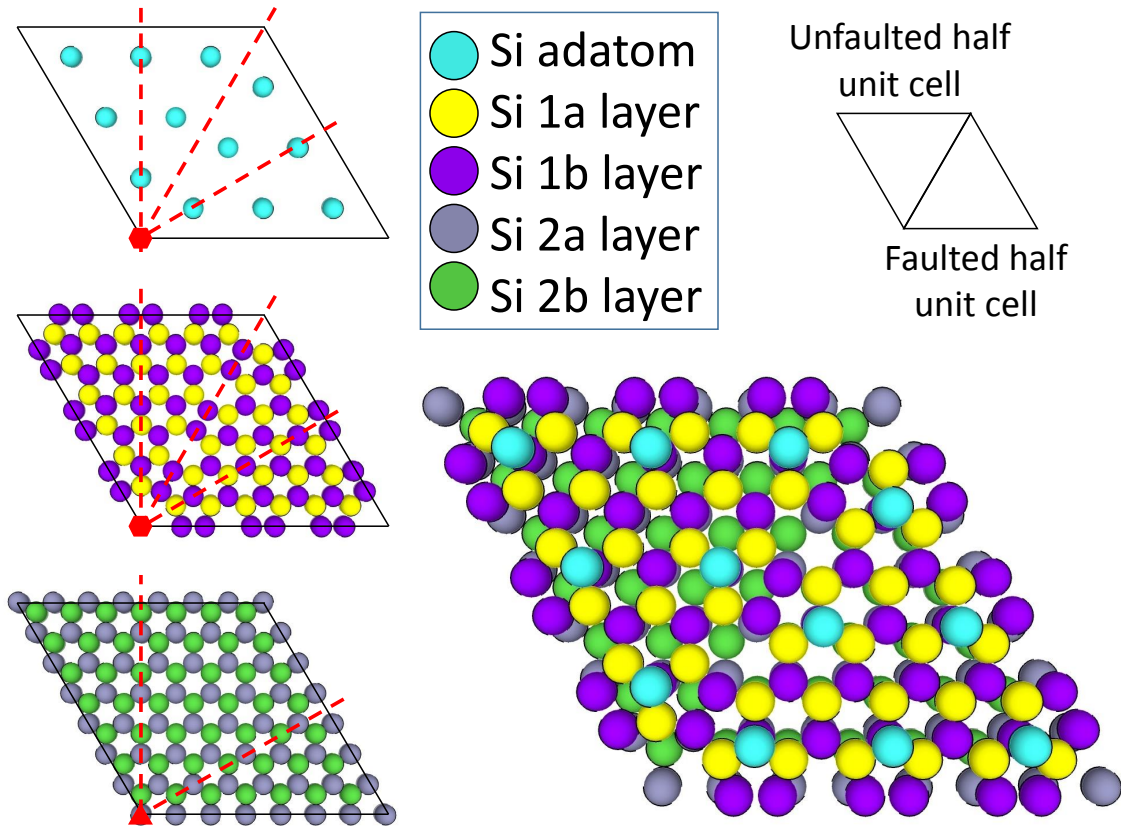


Figure 4.2: 2D and 3D view of the Si  $7 \times 7$  reconstructed structure which consists of adatoms, 1a layer, 1b layer, 2a layer and 2b layer (2a and 2b layer are bulk Si that are nominally unreconstructed)[37]. Si adatom, 1a, and 1b layers have six-fold symmetry, whereas Si 2a, 2b, and bulk layers have three-fold symmetry. The dashed lines indicate mirror symmetries.

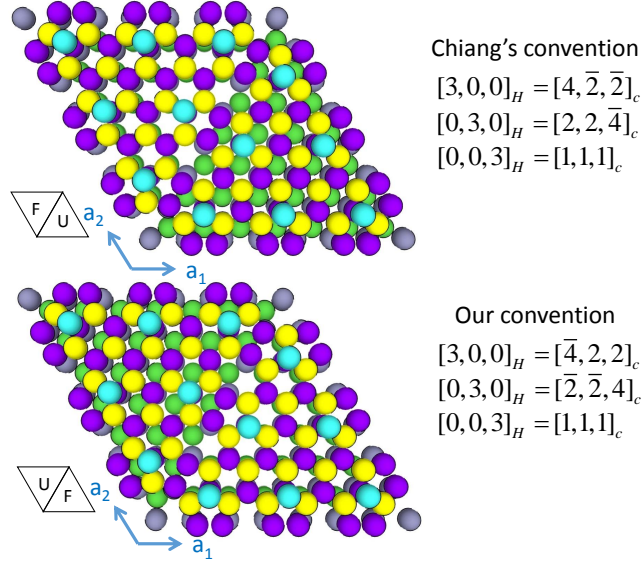


Figure 4.3: The two conventions of the HKL hexagonal coordinate system are only different at the directions of  $\vec{a}_1$  and  $\vec{a}_2$  in real space.

results that follow either of the conventions. Choosing the faulted half unit cell to be at the right side of the origin, the result will follow our convention. It should be noted that using the in-plane atomic positions from the schematic diagram of Ref#[37] figure 1 will get to Chiang's convention. Fig. 4.2 has a different orientation of Si 2a and 2b layer (and bulk Si) than Ref#[37] figure 1, and it leads to the convention that we follow.

Combing the in-plane and out-of-plane geometry from both the top view and the side view shown in Fig. 4.4, the translational vector from the Si b layer to the Si a layer above is  $\vec{R}_0 = \frac{2}{3}\vec{a}_1 + \frac{1}{3}\vec{a}_2 + \frac{1}{12}\vec{a}_3$ , the translational vector from the Si a layer to the next Si a layer is  $\vec{R} = \frac{2}{3}\vec{a}_1 + \frac{1}{3}\vec{a}_2 + \frac{1}{3}\vec{a}_3$ , where  $a_3 = c_H$  is the height of the unit cell.

If we choose one Si 3a layer atom as the origin (0,0,0) in real space, summing over

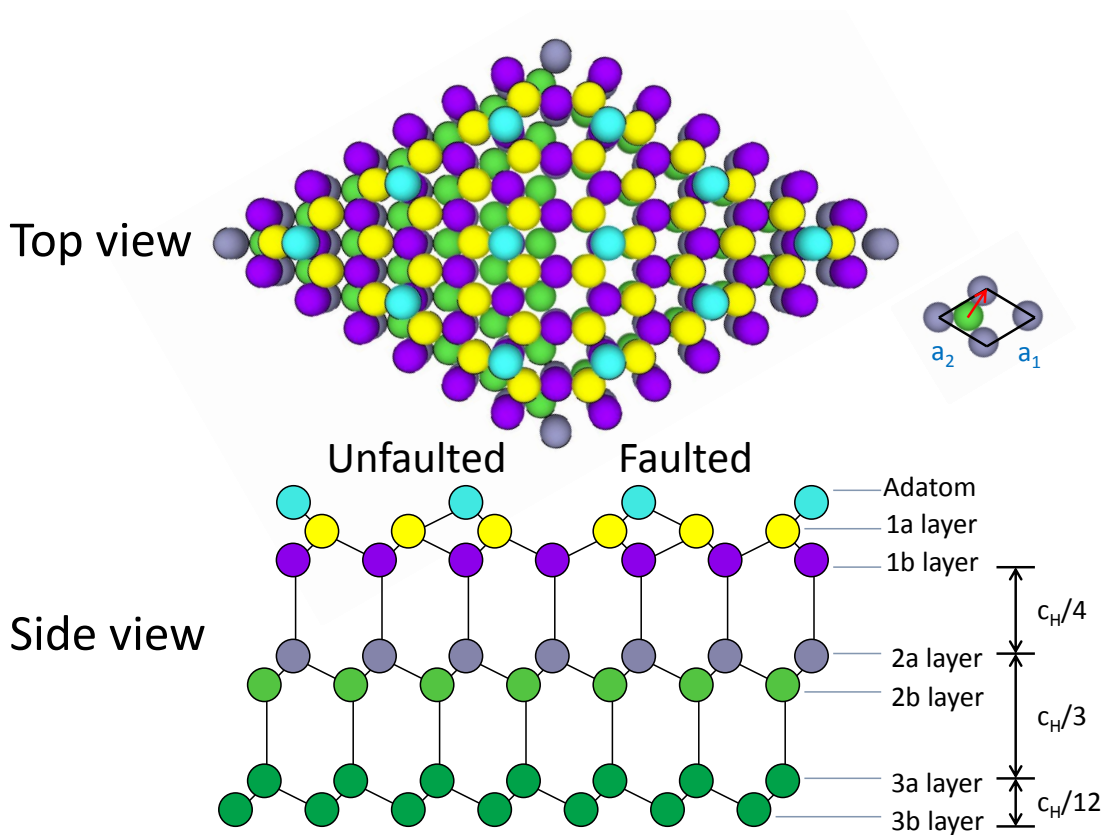


Figure 4.4: Top view and side view of the Si 7x7 layers, the 1b layer Si atoms are drawn at the ideal positions, rather than the dimer positions. The scale is different in top view and side view figures, and layer 3a and 3b are not shown in the top view figure. The spacing between the nearest Si a,b layer is  $\frac{c_H}{12}$ , the spacing between two Si a layers or b layers is  $\frac{c_H}{3}$  (same as  $d_{Si}$ ), where  $c_H$  is the height of the unit cell.

all 49 atoms in the unit cell in plane will give me

$$A_{3a} = (1 + e^{i2\pi H} + e^{i2\pi 2H} + e^{i2\pi 3H} + e^{i2\pi 4H} + e^{i2\pi 5H} + e^{i2\pi 6H}) \\ (1 + e^{i2\pi K} + e^{i2\pi 2K} + e^{i2\pi 3K} + e^{i2\pi 4K} + e^{i2\pi 5K} + e^{i2\pi 6K}). \quad (4.8)$$

Then

$$A_{3b} = A_{3a} e^{-i2\pi(\frac{2}{3}H + \frac{1}{3}K + \frac{1}{12}L)}. \quad (4.9)$$

One Si unit cell contains three type a layers and three type b layers, summing over all unit cells (vertically) give us

$$A_{bulk} = A_{3a} [1 + e^{-i2\pi(\frac{2}{3}H + \frac{1}{3}K + \frac{1}{12}L)}] [1 + e^{-i2\pi(\frac{2}{3}H + \frac{1}{3}K + \frac{1}{3}L)} + e^{-i2\pi(\frac{4}{3}H + \frac{2}{3}K + \frac{2}{3}L)}] \\ \div [1 - e^{-i2\pi(2H + K + L)}]. \quad (4.10)$$

As discussed in chapter 3, the in-plane sum could be treated as  $\delta$  functions, then it could be combined into the scale factor. Bulk Si has 1 by 1 periodicity, only integer H and K values give non-zero contribution for bulk rod, the denominator is equivalent to  $[1 - e^{-i2\pi L}]$ .

The term for the Si roughness  $|V_{sub}|^2$  becomes

$$|V_{sub}|^2 = e^{-4\frac{\sigma_{sub}^2}{d_{Si}^2} \sin^2 \frac{\vec{Q} \cdot \vec{R}}{2}} = e^{-4\frac{\sigma_{sub}^2}{d_{Si}^2} \sin^2 \frac{2\pi(2H + K + L)}{6}}, \quad (4.11)$$

For Si 7x7 structures, we have to count all the atoms in each layer as shown in Fig. 4.2. For 2a and 2b layers, it is the same as bulk case, but for adatom, 1a and 1b layers, we have to get the in-plane position for each atom.  $A_{7 \times 7}$  can be calculated by summing  $e^{i\vec{Q} \cdot \vec{r}}$  for all the atoms in the 7x7 structure. Si 7x7 has the periodicity of 7 by 7, the in-plane translational vector between unit cells is  $\vec{R} = n_1 7\vec{a}_1 + n_2 7\vec{a}_2$ , but the

in-plane momentum transfer is still denoted as  $\vec{Q}_{//} = H\vec{b}_1 + K\vec{b}_2$ , thus H,K=integer/7 will also give non-zero summation. As the result we have n/7 fractional rods which describe the Si 7x7 structure. (For bulk Si, even the in-plane summation factor is non-zero,  $A_{3a}$  itself is zero if H,K=n/7 because of the periodicity in summing  $e^{i\vec{Q}\cdot\vec{r}}$  of the 49 atoms, so bulk Si has no contribution to the n/7 rods.)

### Truncation rod for Ag

Ag has a different lattice constant than Si, that means for the same momentum transfer Q, the H', K' and L' values in Ag coordinate are different than the H, K and L values in Si coordinate. The relationship between the Si coordinate and Ag coordinate is  $H = \frac{d_{Si}}{d_{Ag}}H'$ ,  $K = \frac{d_{Si}}{d_{Ag}}K'$ , and  $L = \frac{d_{Si}}{d_{Ag}}L'$ , and we take  $\frac{d_{Si}}{d_{Ag}} = 1.328$ . For example,  $\text{Ag}(1,1,0)_H = (1.328, 1.328, 0)_H$ .

The scattering amplitude for a FCC Ag truncation rod has no contribution from the Si substrate or the Ag wetting layer. Ag truncation rod measurements are modeled as a free standing Ag FCC structure with 1x1 in-plane periodicity while taking  $\phi_1 = 1$ . The cross-hatched region in the first atomic layer of the islands in Fig. 4.1 will contribute to the rod only if that layer exhibits the FCC structure of Ag.

Similar to what we get from the Si case, the 3D translational vector from a Ag layer to the next Ag layer is  $\vec{R} = \frac{2}{3}\vec{a}'_1 + \frac{1}{3}\vec{a}'_2 + d_{Ag}\hat{z}$ , where  $\vec{a}'_1$  and  $\vec{a}'_2$  are the real space in-plane vectors for Ag,  $|\vec{a}'_1| = |\vec{a}'_2| = 2.892 \text{ \AA}$ , and  $d_{Ag} = 2.361 \text{ \AA}$  is the spacing between the Ag layers along the (111) direction. The phase  $e^{i\vec{Q}\cdot\vec{R}}$  has both the in-plane part  $e^{i2\pi\frac{2H'+K'}{3}}$  and the out-of-plane part  $e^{iQ_{\perp}d_{Ag}}$ .

Keeping track of the in-plane phase each time we go to a higher layer while using the vertical height  $z_n$  directly to calculate the out-of-plane phase, the amplitude of

the n-th layer Ag is given as

$$A_n = (e^{i2\pi\frac{2H'+K'}{3}})^{n-1} e^{iQ_\perp z_n}, \quad (4.12)$$

assuming the in-plane phase is zero at the first layer. Then take the vertical disorder into account and sum over all fractions of different island heights, the scattering amplitude for a  $\text{Ag}(H',K')_H$  truncation rod is calculated as

$$A_{Ag} = \sum_{j=1} p_j \sum_{n=1}^j \phi_n (e^{i2\pi\frac{2H'+K'}{3}})^{n-1} e^{iQ_\perp z_n} e^{-\frac{1}{2}Q_\perp^2 \sigma_j^2}. \quad (4.13)$$

It should be noted that  $p_j$  determined from the measurement of truncation rods will have an overall unknown scale factor whereas  $p_j$  can be determined on an absolute scale from specular reflectivity because it includes a strong reference amplitude from the substrate.

### 4.1.3 Corrections from scattering geometry

Now we have set up the equations to calculate the scattered x-ray intensities from the sample, but if we are going to compare them with the experimental results, we have to take into account some correction factors from the scattering geometry[39, 40]. We included the Lorentz factor for volume integration in reciprocal space, polarization factor for beam polarization, footprint correction for beam spilling off the sample at low angles, and sample active area correction for the area acceptance of the detector on the sample. Details are described in the Appendix A.



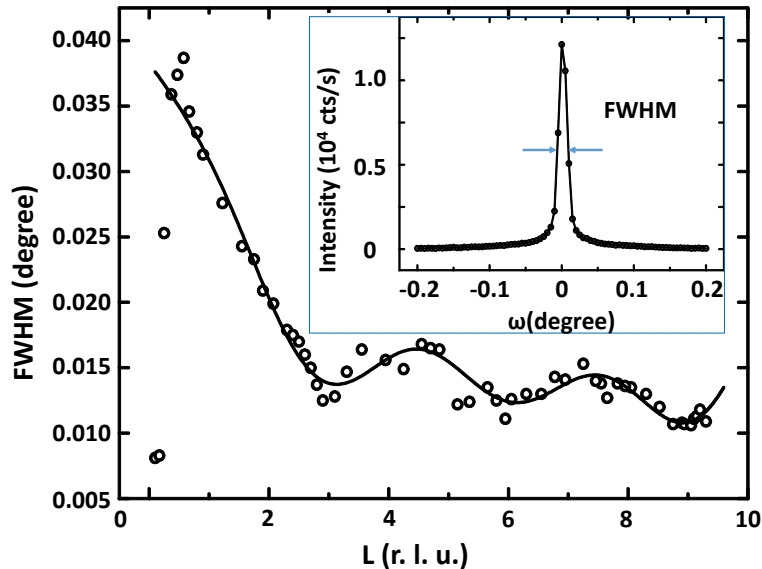


Figure 4.5: The full-width-at-half-maximum (FWHM) of transverse peaks for specular reflectivity measured at different  $L$  values for a clean Si(111)7x7 surface. The solid line is a fit using a combination of Bessel functions. The inset shows a typical transverse scan where the FWHM of the peak is always smaller than 0.05 degree, and the background is basically flat.

## 4.2 Vertical structure of Ag thin film from specular reflectivity measurements

Specular reflectivity has been measured to study the vertical structure of Ag thin film. Transverse scan is needed in order to get the integrated intensity, but taking a transverse scan at each data point is too slow for the high density of data points we take, so a quick way of measuring reflectivity is applied and pseudo integrated intensity is calculated for data analysis.

After sample alignment, a  $\theta$ - $2\theta$  line scan is run through the specular along the  $L$  direction to measure the specular intensity, another  $\theta$ - $2\theta$  line scan is run with a small offset in  $\theta$  angle (e.g. 0.05 degrees) to measure the background. The difference

between the two scans gives the specular peak height. A series of transverse scans are measured at different  $L$  values to get the specular peak width, and the full-width-at-half-maximum (FWHM) of the scans are fitted to a combination of Bessel functions. The specular peak height is multiplied by the pseudo transverse width from the Bessel fit to get the pseudo integrated intensity. The inset of Fig. 4.5 shows a typical transverse scan, where the peak has a narrow FWHM and flat background. Fig. 4.5 shows the transverse peak width of a clean Si 7x7 surface at different  $L$  values, which oscillates up and down. The amplitude of the oscillation varies from sample to sample. Unfortunately we did not perform a systematic measurement of the transverse width for each sample, we used the same pseudo transverse width from a clean Si 7x7 sample to calculate the pseudo integrated intensity for most of the specular reflectivity measurements.

### 4.2.1 Coverage dependence measurements

In order to establish the evolution of the vertical structure, we start from analyzing the specular reflectivity data at the lowest coverage. Fig. 4.6a shows a reflectivity measurement of 0.3 ML of Ag deposited on the Si(111)7x7 at 300 K. At such coverage, there is no island formed, only Ag wetting layer covering the Si substrate. Near  $L=2.6$  there is a cusp in the reflectivity where its position and depth is sensitive to both the height  $z_{wet}$  and the coverage  $\Theta$  of the wetting layer. With Si 7x7 parameters fixed at Robinson's values[34], least-squares fitting gives  $z_{wet} = 2.18 \pm 0.15 \text{ \AA}$ ,  $\sigma_{wet} = 0.3 \pm 0.1 \text{ \AA}$ ,  $\sigma_{sub} = 0.9 \pm 0.4 \text{ \AA}$  and  $\Theta = 0.30 \pm 0.03$  ML. These values of  $z_{wet}$ ,  $\sigma_{wet}$  and  $\sigma_{sub}$  are consistent for all of the coverages that we studied. The parameter error bars were obtained by determining the range over which the parameter could be varied while

maintaining an acceptable fit to the data.

Our analysis used the structural parameters previously determined for the Si(111)7x7[34] except that the  $\zeta_j$  were fixed at  $0.1\text{\AA}$  and the  $z_j$  positions of the Si atoms for  $j=1$  through 4 were refined to give slightly improved fits. Each time we create a new sample the Si 7x7 is annealed and the parameters should vary. The refined  $z_j$  did not change more than  $\pm 0.08\text{\AA}$  from the literature values due to the minimal sensitivity to them in the presence of Ag. Although an early x-ray scattering study of 100 ML Ag on Si(111)7x7 suggested that the 7x7 reconstructed surface of Si was severely modified by the deposition of Ag[41], an attempt to use their structural parameters for the Si layers, however, did not fit our data. Moreover, our present in-situ study clearly shows the 7x7 reflections from the wetting layer. It is possible that the earlier x-ray scattering study was affected by the sample transfer after the film was grown and/or by the long time between the growth and the x-ray measurement[41].

To observe the emergence of islands, we performed another deposition at a slightly higher coverage, as shown in Fig. 4.6b for 0.45 ML Ag deposited at 300K. Compared with the measurement from 0.3 ML, a small but broad peak around  $L=3.98$  is clearly visible in the reflectivity, which is the location of the  $\text{Ag}(1,1,1)_c$  Bragg peak and it indicates the existence of FCC Ag islands. These results are consistent with STM studies that show the start of 3D islands formation at 0.35 ML[15]. From our fit to the reflectivity, we find that  $\sim 5\%$  of surface is covered by islands.

Measurements were also performed at higher coverages. Fig. 4.7 shows a specular reflectivity measurement for 0.9 ML Ag deposited on Si(111) 7x7 at 300K. In this case two FCC Ag Bragg peaks appear prominently near  $L= 3.98$  and  $7.96$  as well as one subsidiary maximum that is located between them. In analogy to a three-slit optical

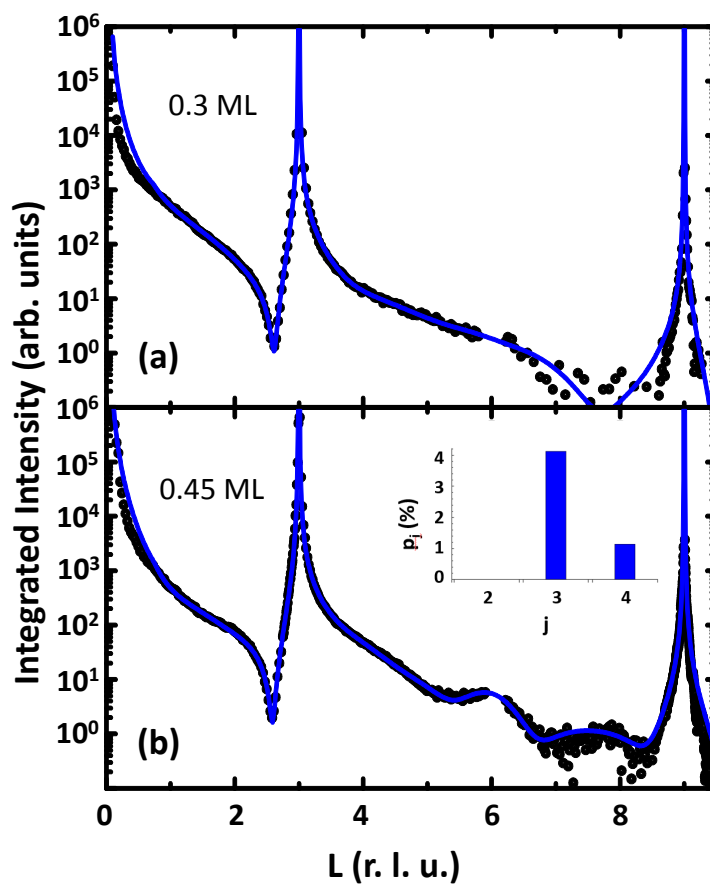


Figure 4.6: Specular reflectivity measurements for Ag deposited on Si(111)7x7 at 300K. The solid curves are a fit from the model. (a) 0.3 ML Ag shows only a wetting layer with no islands. (b) 0.45 ML Ag reveals the emergence of islands and the in-set shows the corresponding island height distribution determined from fitting the data.  $p_3$  is dominant and about 5% of the surface is covered by Ag islands.

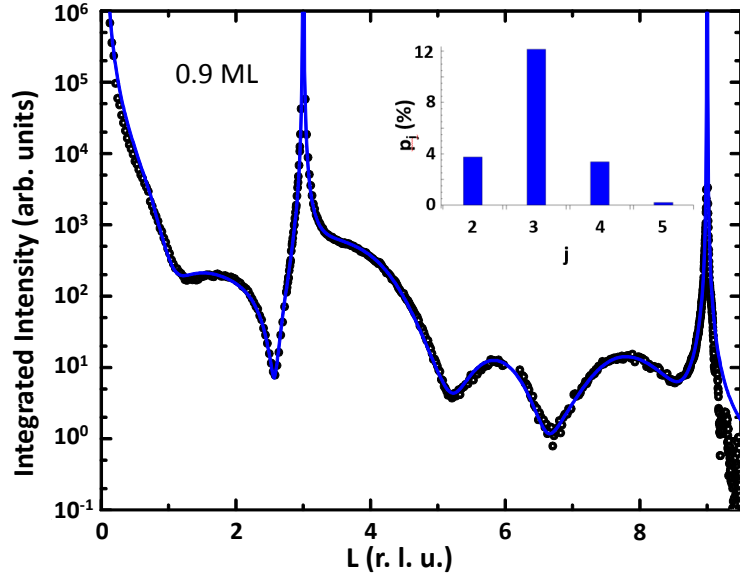


Figure 4.7: Specular reflectivity measurement for 0.9 ML Ag deposited on Si(111) 7x7 at 300K. The solid curve is a best fit to the model. The in-set shows the histogram of  $p_j$  where there are predominantly 3-layer islands.

interference pattern and because the atomic layers of Ag dominate the scattering, the single subsidiary maximum suggests islands having three atomic layers with the conventional lattice spacing of FCC Ag. Quantitatively fitting the data gives a height distribution shown in the inset, which indeed indicates the predominance of three-layer islands.

Fig. 4.8 shows a specular reflectivity measurement for 1.8 ML Ag deposited on Si(111)7x7 at 300K. A fit to the data reveals the predominance of 4-layer islands, which is qualitatively apparent from the two subsidiary maxima between the Bragg peaks.

Fig. 4.9 summarizes the coverage-dependence of the height distributions that were determined from our experiments at 300K. The vertical axis of the plot is the population of islands having a given height relative to the total population of the islands,

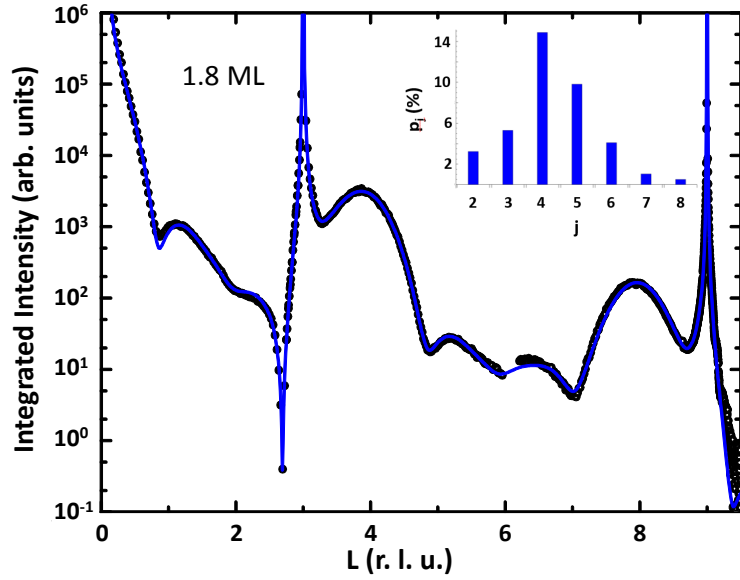


Figure 4.8: Specular reflectivity measurement for 1.8 ML Ag deposited on Si(111) 7x7 at 300K. The solid curve is a best fit to the model. The in-set shows the histogram of  $p_j$  where there are predominantly 4-layer islands at this higher coverage.

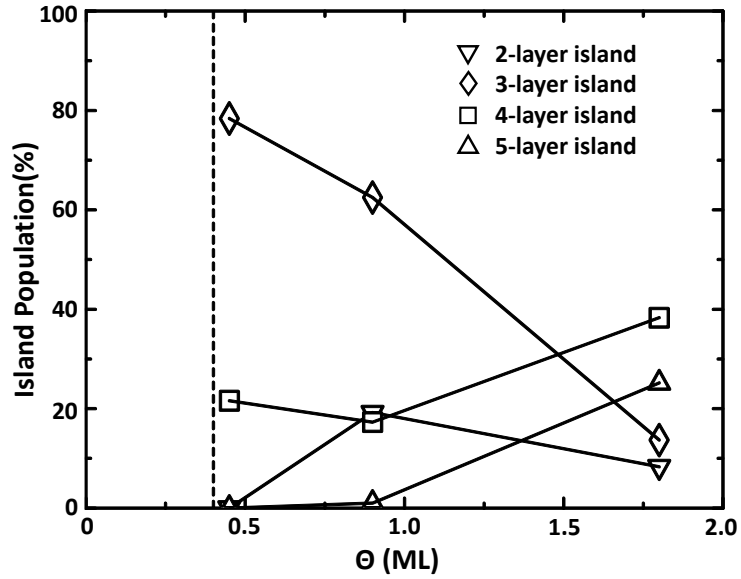


Figure 4.9: Population,  $\frac{p_j}{\sum_{j=2} p_j}$ , of island heights measured as a function of Ag coverage at 300K. The vertical dashed line indicates the coverage at which islands begin to form after the completion of the wetting layer.

$\frac{p_j}{\sum_{j=2} p_j}$ . It can be seen that there is a clear preference for 3-layer islands at low coverage; however, as the coverage increases, the preference shifts towards taller islands. Our results are in good agreement with STM studies[17] after taking into account the different ways of counting island layers. Note that a small population of 2-layer islands is also found in the measurement, this is consistent with prior STM studies in the literature[15, 42], and it will be seen later that 2-layer islands go away with higher temperature and/or higher coverage.

### 4.2.2 Temperature dependence measurements

The temperature dependence of the island growth was also studied. Fig. 4.10 shows the specular reflectivity measurements of 1.8 ML Ag deposited on Si(111)7x7 at 260 K, 300 K, 360 K and 400 K. It can be seen that as temperature increases, the width of the Ag Bragg peaks (around  $L=3.98$  and  $7.96$ ) decreases, and the intensities also increases, indicating higher islands.

Fig. 4.11 shows a histogram of island distributions ( $p_j$ ) for the temperature dependence study. As the temperature increases, the islands tend to grow higher and have a wider island height distribution. This behavior is consistent with increased kinetic relaxation with temperature where the system tries to reduce the interfacial energy by increasing the island height to the extent permitted by the available mobility.

When we compare the measurements of 0.9 ML Ag deposited on Si(111)7x7 at different temperatures, we also observe the Ag Bragg peak becomes higher and narrower as temperature increases, similar to 1.8 ML coverage measurements.

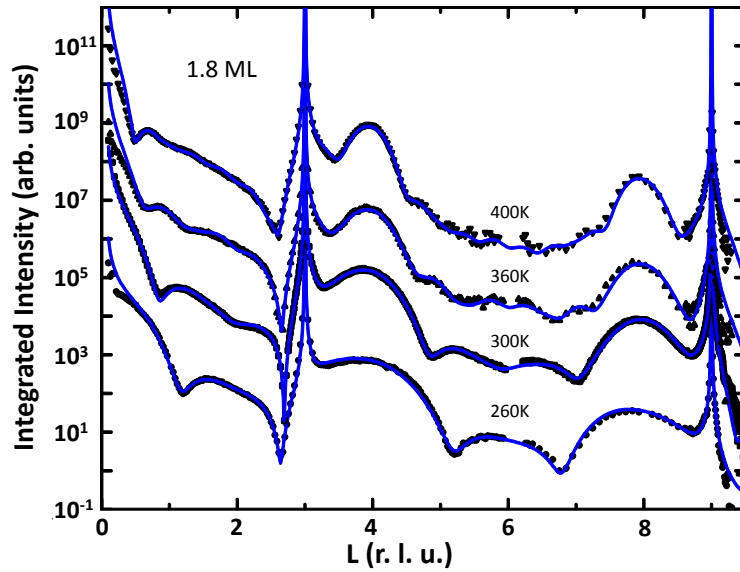


Figure 4.10: Specular effectivity measurements of 1.8 ML Ag deposited on Si(111)7x7 at different temperatures. Solid curves are the best fits.

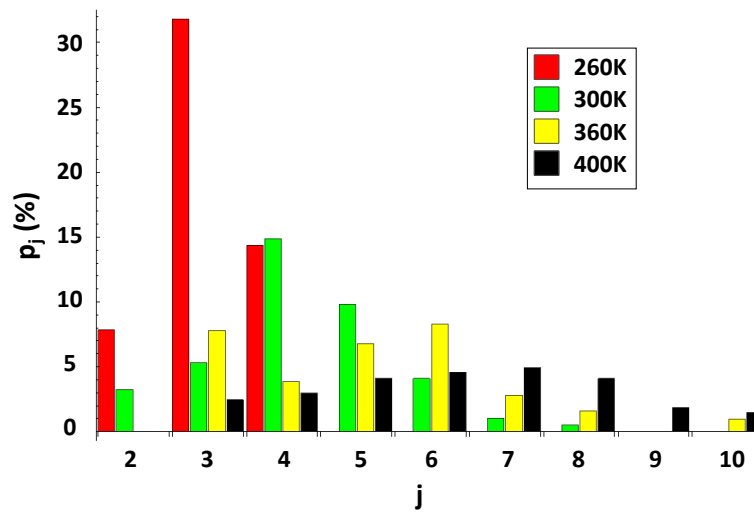


Figure 4.11: The island height distribution,  $p_j$ , for 1.8 ML of Ag deposited at different temperatures. As the temperature increases, the average island height and the breadth of the distribution increases, which indicates that mobility plays an important role in the observed distributions.



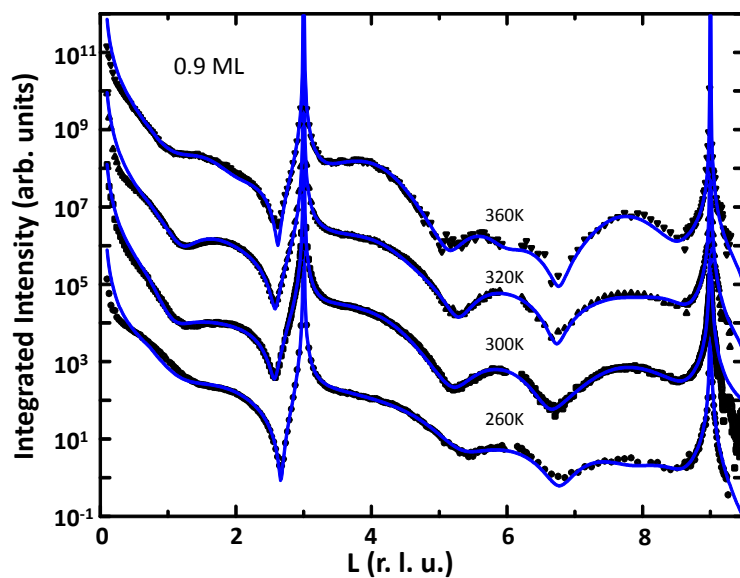


Figure 4.12: Specular effectivity measurements of 0.9 ML Ag deposited on Si(111) 7x7 at different temperatures. Solid curves are the best fits.

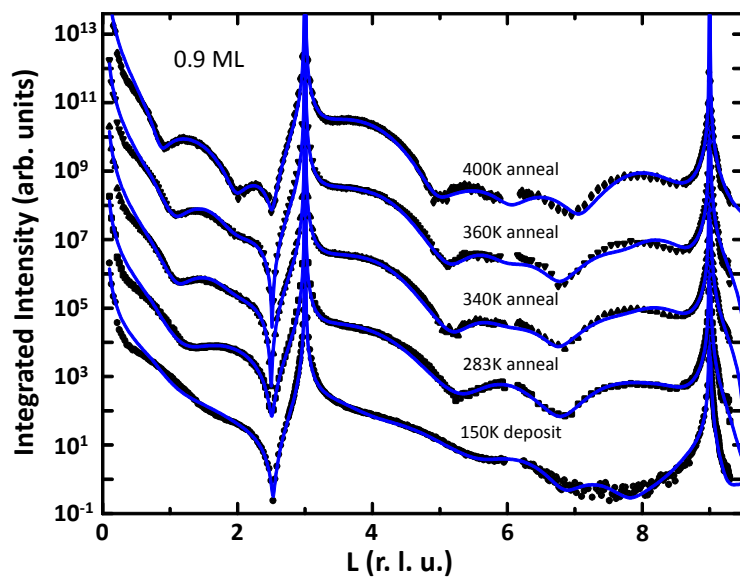


Figure 4.13: Specular effectivity measurements of 0.9 ML Ag deposited on Si(111) 7x7 at 150K then annealed to different temperatures. Solid curves are the best fits.

### 4.2.3 Measurements for annealing experiments

One sample was created after deposition of 0.9 ML Ag Si(111)7x7 at 150K. We could barely observe Ag Bragg intensities, so the sample was annealed to different temperatures. As shown in Fig. 4.13, Ag Bragg peaks show up after the annealing. The change of the fringes around the anti-Bragg region  $L=2$  also indicates that the Ag islands are becoming taller in height.

## 4.3 Vertical structure of 21.6 ML Ag film

One sample with relatively high coverage of 21.6 ML Ag deposited on Si(111)7x7 at 300K was also created. The measured specular reflectivity is shown in Fig. 4.14, we observe strong Ag Bragg peaks around  $L=3.98$  and  $L=7.96$ . Fig. 4.15 shows the zoomed in view around the Ag Bragg peaks. The fringes (subsidiary maxima) around the Ag Bragg peaks die off quickly.

### 4.3.1 Binomial distribution model

For such a thick film, it is impractical to use individual  $p_j$  to describe the island height distributions in reflectivity models. A binomial distribution is used to describe  $p_j$ . After the simplifications  $\phi_n = 1$ ,  $z_n = z_{island} + (n - 1)d_{Ag}$ , and  $\sigma_j = \sigma$ , the second term in equation 4.7 becomes

$$A_{Agfilm} = e^{iQz_{island}} e^{-\frac{1}{2}Q^2\sigma^2} \sum_{j=1} p_j \sum_{n=1}^j e^{iQ(n-1)d_{Ag}}. \quad (4.14)$$

Utilizing the power series, the equation could be further simplified to

$$\begin{aligned}
A_{Agfilm} &= e^{iQz_{island}} e^{-\frac{1}{2}Q^2\sigma^2} \sum_{j=1} p_j \frac{(1 - e^{iQjd_{Ag}})}{(1 - e^{iQd_{Ag}})} \\
&= \frac{e^{iQz_{island}} e^{-\frac{1}{2}Q^2\sigma^2}}{(1 - e^{iQd_{Ag}})} \sum_{j=1} p_j (1 - e^{iQjd_{Ag}}) \\
&= \frac{e^{iQz_{island}} e^{-\frac{1}{2}Q^2\sigma^2}}{(1 - e^{iQd_{Ag}})} \left( \sum_{j=1} p_j - \sum_{j=1} p_j e^{iQjd_{Ag}} \right).
\end{aligned} \tag{4.15}$$

From definition, any binomial distribution follows  $\sum_{j=0} p_j = 1$ , but our constraint is  $\sum_{j=1} p_j = 1 - p_{wet}$  with  $p_0 = 0$ . So after everything is derived from a conventional binomial distribution, our distribution needs to be multiplied by the factor  $(1 - p_{wet})$ . In order to create a binomial island height distribution, only two parameters are needed in the model: the maximum island height  $M$ , and the average island height  $\bar{n}$ . (More details of the binomial distribution are discussed in chapter 3.2 or 5.2.2). Following the treatment of equation 3.18, the Ag amplitude for a thick film in specular reflectivity is given as

$$A_{Ag} = p_{wet} \phi_{wet} e^{iQz_{wet}} e^{-\frac{1}{2}Q^2\sigma_{wet}^2} + (1 - p_{wet}) e^{iQz_{island}} e^{-\frac{1}{2}Q^2\sigma^2} \frac{1 - (pe^{iQd_{Ag}} + q)^M}{1 - e^{iQd_{Ag}}}. \tag{4.16}$$

A best fit to the Binomial distribution model is plotted in Fig. 4.14 as the solid curve. Here we will first discuss the Ag Bragg peak regions (zoomed in and plotted in Fig. 4.15) that are directly related with the Binomial distribution model, then we will discuss the anti-Bragg regions that is associated with  $\phi_{wet}$ .

The fringes around the Ag Bragg peak are related with the two parameters: maximum island height  $M$  and average island height  $\bar{n}$ . Fig. 4.16 shows the effect of the two parameters, the spacing between the fringes in the Ag Bragg peak region is in-

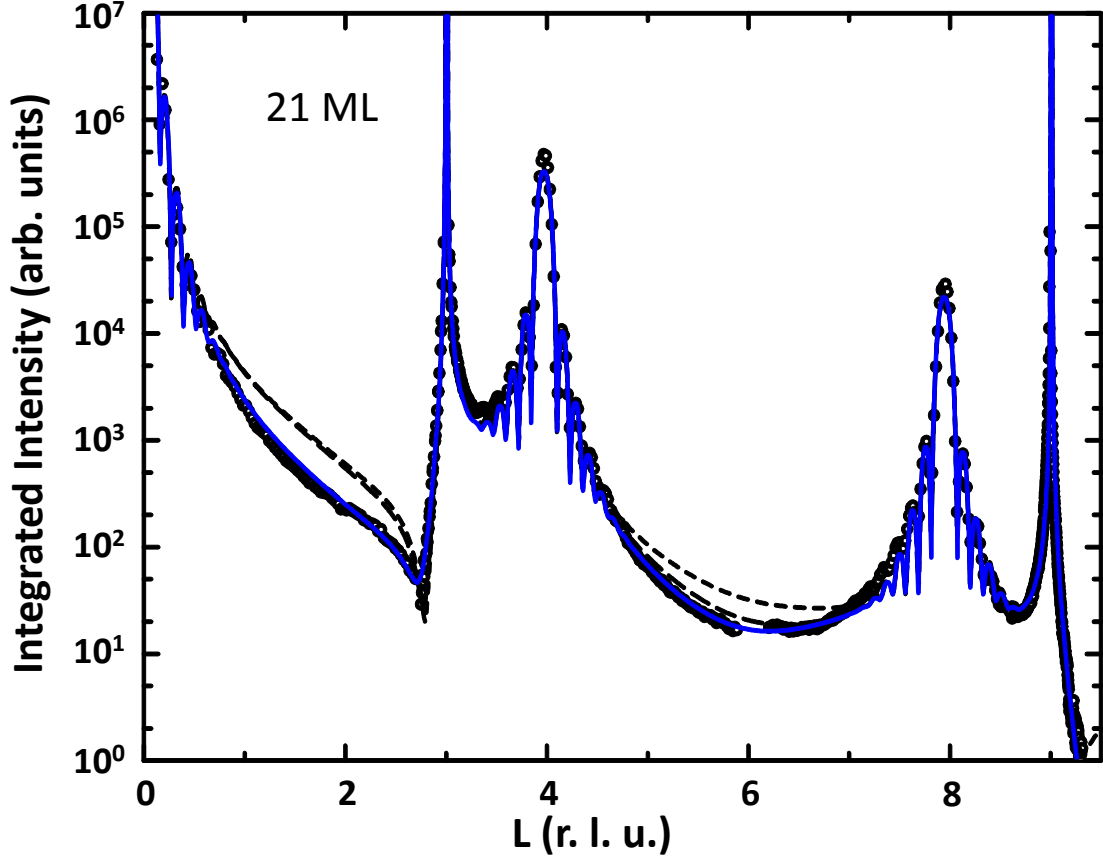


Figure 4.14: Specular reflectivity measurements from a sample of 21.6 ML Ag on Si(111)7x7 deposited at 300K. Solid curves are the best fit using a binomial distribution of  $\bar{n} = 30.9$  and  $M=39$  with  $p_{wet} = 0.4$ ,  $\phi_{wet} = 0$ , and  $\sigma_{wet}=0$ . The short dashed curve is plotted with the same binomial distribution with  $\phi_{wet} = 0.3$  and  $\sigma_{wet} = 0.1\text{\AA}$ , the long dashed curve is plotted with  $\phi_{wet} = 0.3$  and  $\sigma_{wet} = 0.3\text{\AA}$ . We see that the roughness  $\sigma_{wet}$  could reduce the Ag anti-Bragg intensity around  $L=6$ , but there is no way for the fit to come close to the data at the Ag anti-Bragg region around  $L=2$  with the non zero wetting layer density.

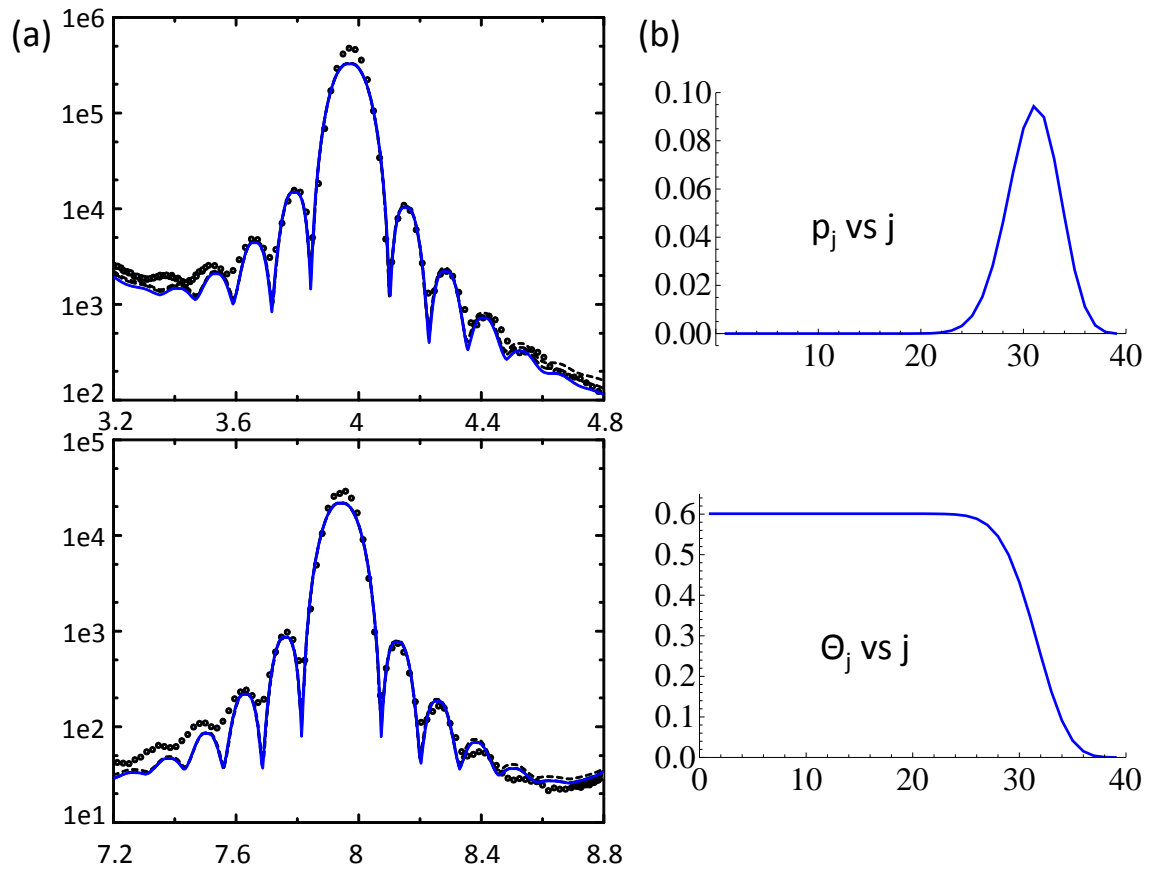


Figure 4.15: (a) Zoomed in view of the specular reflectivity shown in Fig. 4.14 around the Ag Bragg peak regions  $L=3.98$  and  $L=7.96$ . Spacing between the Ag fringes near the Bragg peak is related with the average film height. How fast the fringes die off is related with the roughness of the upper interface. The change of wetting layer density  $\phi_{wet}$  described in Fig. 4.14 does not affect the Ag Bragg peaks, only a slight change can be seen as dashed curves very far away from the Bragg peaks. (b) The island height distribution profile and the coverage profile from the fit plotted in Fig. 4.14.

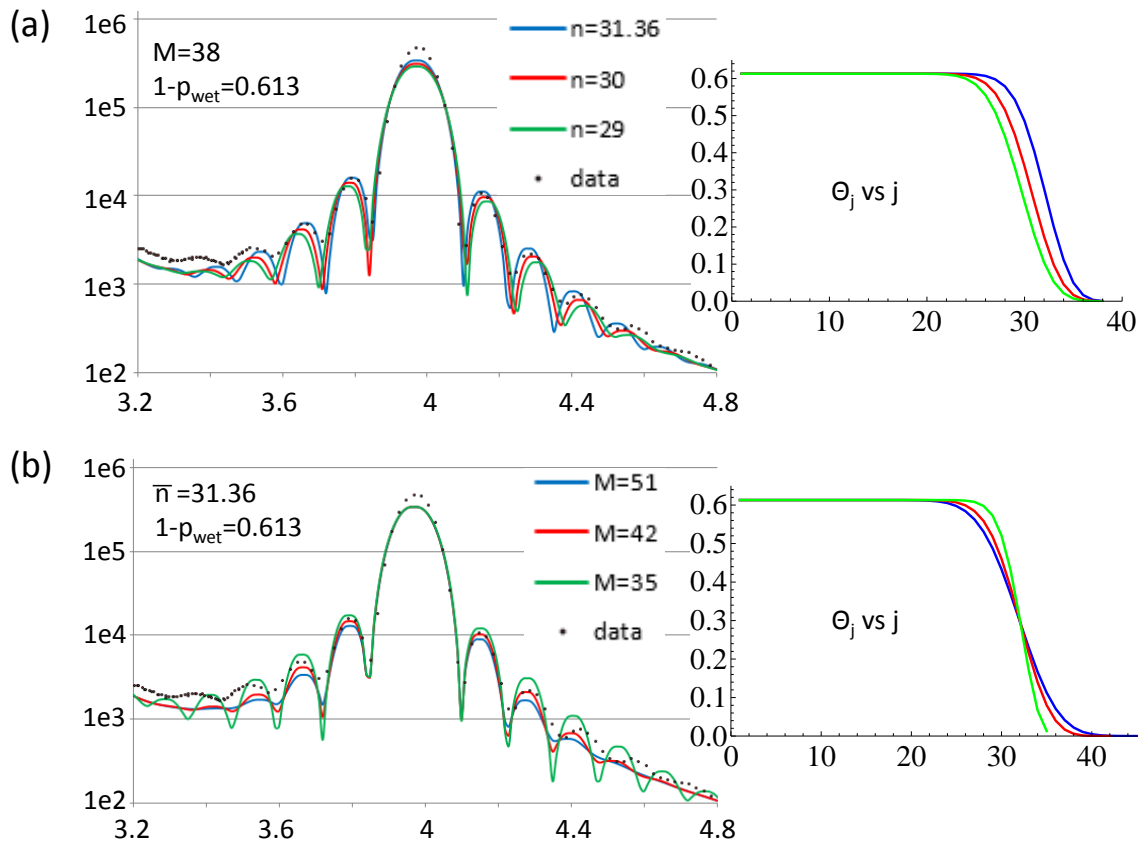


Figure 4.16: Tests for the effect of the binomial model parameters: (a) changing the maximum island height  $M$  while having a constant  $\bar{n}$  modifies the fringe spacing, (b) changing the average island height  $\bar{n}$  while having a constant  $M$  modifies the fringe amplitude. The curves generated from the model are shown on the left, the coverage profile of the film are shown on the right.

versely proportional to  $\bar{n}$ , it has no relationship with  $M$ . The amplitude of the fringes are related with the height fluctuation (roughness) of the upper interface, which is given by the square root of variance  $s = \sqrt{Mp(1-p)}$  (in units of ML) multiplied by the Ag spacing  $d_{Ag}$ . The roughness is related with maximum height  $M$  (once we fix  $\bar{n}$ ) and it determines how fast the fringe intensities dampen, smaller  $M$  gives bigger fringe amplitude.

The maximum height  $M$  needs to be an integer, so  $M$  is manually determined to have the value of 39 based on the fringe amplitudes. Least square fitting gives the average island height  $\bar{n} = 30.9$ . As shown in Fig. 4.15a, the fit is able to get the spacing of the central fringes really well, but it can not get the outer fringes together with the central fringes. It seems like there is some extra interference (probably from the interface) that is weak so it did not affect the central fringes but shifted the outer fringe locations. The cusps between the Ag fringes are a little too deep, but this is the best fit without missing the fringe amplitudes.

### 4.3.2 Low density at the interface

With  $\phi_n = 1$ , the coverage  $\Theta_j$  (or electron density, in units of ML) of each layer could be calculated from  $p_j$ . By definition,  $p_j = \Theta_j - \Theta_{j+1}$  is the exposed fraction of the layers.  $\Theta_M = p_M$  for the top layer,  $\Theta_{M-1} = \Theta_M + p_{M-1} = p_M + p_{M-1}$ , summing up the whole series we get

$$\Theta_j = \sum_{n=j}^M p_n, \quad \text{for } j \geq 2. \quad (4.17)$$

Because we have a Ag wetting layer, we cannot distinguish  $p_1$  from  $p_{wet}$ . Therefore the total coverage for the first monolayer of Ag at the interface is given as

$$\Theta_1 = p_{wet}\phi_{wet} + (1 - p_{wet})\phi_1. \quad (4.18)$$

Interestingly, the 21.6 ML fit gives  $p_{wet} = 0.4$  with  $\phi_{wet} = 0$ . As shown in Fig. 4.14, if we use a non zero  $\phi_{wet}$ , there is no way we could fit the anti-Bragg regions around  $L=2$ . We may not be able to distinguish the contributions between  $\phi_1$  and  $\phi_{wet}$ , but the anti-Bragg regions are sensitive to the total coverage  $\Theta_1$  at the Ag/Si interface. Our fitting result tells us that there is only 0.6 ML Ag at the interface even after a deposition of more than 20 ML – this is a much lower density than our expectation at the interface!

In fact the binomial model fit is limited by 2 parameters. The intensity at the anti-Bragg regions determines  $\Theta_1$  which is  $(1-p_{wet})$  when  $\phi_{wet} = 0$ , and the fringe spacing of Ag Bragg peak determines the average island height  $\bar{n}$ . The total coverage of the film is given as  $(1 - p_{wet})\bar{n}$ , thus there is basically no room to vary the total coverage in the binomial model. The film coverage from the fit is 18.6 ML, this is a slightly lower coverage than our expectation of 21.6 ML, which explains why the Ag Bragg intensity is always lower than the data.

My colleague Shawn Hayden is able to fit the 21.6 ML data with a different model and get a slightly better fitting result. Hayden studied the low interfacial density of Ag/Ag(001) homoepitaxial growth and the deposition angle dependence of the interfacial density from Ag/Si(111)7x7 grazing angle x-ray reflectivity measurements[43]. He used more complex models to describe the film profile and had more freedom in the parameter space. Fig. 4.17 shows a fitting result from Hayden where negative  $p_j$



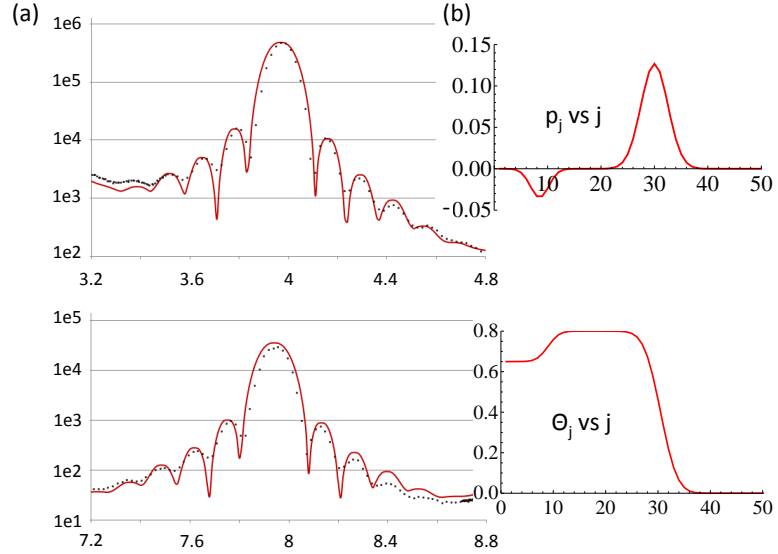


Figure 4.17: Hayden's fit to the specular reflectivity of 21.6 ML Ag film, the whole fit is omitted because it is qualitatively the same as mine in Fig. 4.14. (a)Zoomed in view of Ag Bragg peaks around  $L=3.98$  and  $L=7.96$ , (b)The island height distribution profile and the coverage profile of the film with a back interface.

is allowed to create a back interface between the Ag and Si, and error functions are used to describe the back and top interfaces. The quality of his overall fit is the same as mine, but he is able to get the spacing and the amplitude of the Ag Bragg fringes better with his film profile. The total coverage of 22.7 ML is also slightly closer to our expectation. Although it is a completely different film profile with a back interface, it also requires a low interfacial Ag density (0.65 ML is used in this fit).

We see a hint of a decreasing wetting layer density in our low-coverage samples, as shown in Fig. 4.18. Although it is a relatively small effect and susceptible to systematic errors, the trend is suggestive. The wetting layer coverage  $\Theta_{wet} = p_{wet}\phi_{wet}$  and wetting layer density  $\phi_{wet}$  both decrease as the Ag coverage increases at the two different temperatures we measured. The fits are sensitive to the Ag coverage at the interface  $\Theta_1$ , with  $\phi_1 = 1$  assumed and  $p_{wet}$  calculated from  $1 - \sum p_j$ ,  $\Theta_{wet}$  can be

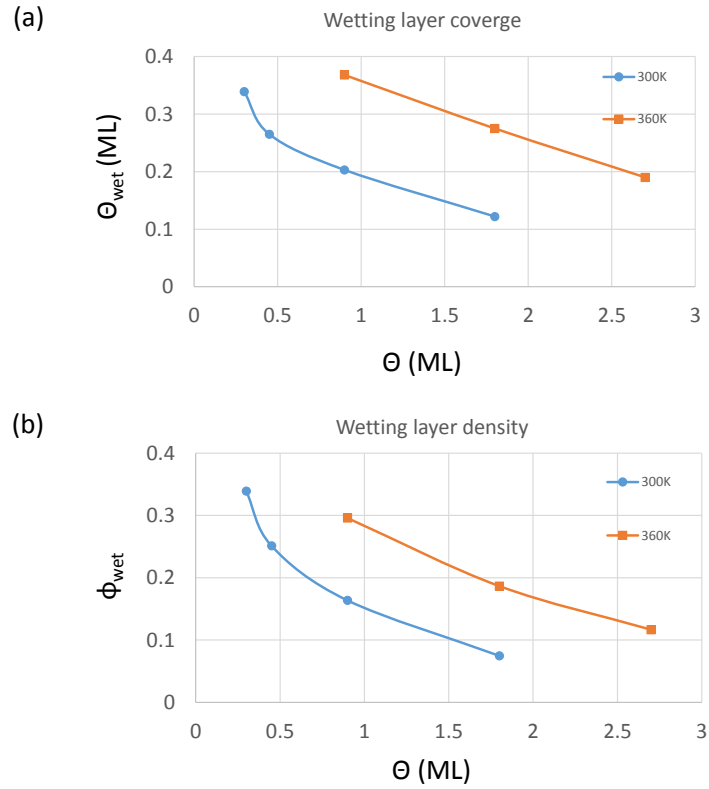


Figure 4.18: (a)Wetting layer coverage  $\Theta_{wet}$  and (b)wetting layer density  $\phi_{wet}$  as a function of film coverage at 300K and 360K. It can be seen that the wetting layer coverage and density decreases with further deposition of the film. The smooth curve connecting the points is just a guide to the eye. Note that the assumption  $\phi_1 = 1$  for the first layer of FCC island is used.

determined, then  $\phi_{wet}$  is calculated as  $\Theta_{wet}/p_{wet}$ . It might be possible that  $\phi_1 < 1$ , which could compensate for some wetting layer decrease, but the decreasing trend remains. A possible explanation for this decrease of wetting layer density is that when the islands consume the wetting layer to form FCC structure (which will be discussed later), they consume not only the wetting layer underneath them but also the wetting layer around them, so the atoms in the wetting layer are pulled away. (Fig. 4.18 shows that the wetting layer coverage and density is higher at 360K than 300K for the same coverage. This could be explained by the saturation coverage of the wetting layer is slightly higher at a higher temperature[15].)

## 4.4 Fitting parameter tables for specular reflectivity and rods

Here we give the parameter tables for all specular reflectivity fits. The parameters are defined in section 4.1 and illustrated in Fig. 4.1. In the process of fitting the specular reflectivity measurements, several different ways to deal with the Si 7x7 parameters have been tried out. Different sets of fixed 7x7 parameters are used, fixing all the fluctuation (roughness) parameters  $\zeta_j$  and fitting the position parameters  $z_j$  is used, fixing the position parameters  $z_j$  and fitting the roughness parameters  $\zeta_j$  is also used. We do not have the independent sensitivity for all 10 Si 7x7 parameters. For our convenience to fit all the data in a systematic way, we choose to fix all  $\zeta_j$  to 0.1Å, keep adatom layer position at  $z_5=1.58\text{\AA}$  from Robinson's work[34], and fit the displacement from the ideal layer positions  $\Delta z_j$  for  $j=1$  to 4. (All the positions of Ag wetting layer, Ag film, and Si adatoms are relative to the *real* position of Si 1a layer

Parameters	21.6ML_300K	0.9ML_150K deposit	0.9ML_283K anneal	0.9ML_340K anneal	0.9ML_360K anneal	0.9ML_400K anneal
$S_F$	1.879	0.95	0.921	0.98	0.937	1.008
$z_{island}$	2.148	1.837	2.051	2.175	2.176	2.501
$\sigma$	0.069	0.354	0.126	0.140	0.157	0.205
$M$	39	2.263	2.242	2.289	2.3	2.502
$n$	30.9	0.265	0.177	0.109	0.096	0.105
$z_{wet}$	2.18	0.141	0.041	0.000	0.000	0.247
$\phi_{wet}$	0	1.558	1.471	1.208	1.151	0.909
$\sigma_{wet}$	0	0.7341	0.7488	0.7554	0.7573	0.7693
$\sigma_{sub}$	0.161	0.1288	0.0538	0.0408	0.0395	0.0546
$p_{wet}$	0.399	0.1008	0.1475	0.1168	0.1035	0.0446
$\Delta z_1$	-0.01	0.0363	0.0319	0.0624	0.0745	0.0916
$\Delta z_2$	-0.04		0.0180	0.0118	0.0108	0.0295
$\Delta z_3$	0.02			0.0128	0.0144	0.0104
$\Delta z_4$	0.08					
$z_5$	1.58					
$\zeta_1$	0.1	-0.0005	-0.0372	-0.0548	-0.0723	-0.0131
$\zeta_2$	0.1	-0.0986	-0.0249	-0.0613	-0.0834	-0.0261
$\zeta_3$	0.1	0.0823	0.0780	0.0181	-0.0086	0.0067
$\zeta_4$	0.1	0.2468	0.0419	0.0275	0.0245	-0.0547
$\zeta_5$	0.1	1.58	1.58	1.58	1.58	1.58
		0.1	0.1	0.1	0.1	0.1
		0.1	0.1	0.1	0.1	0.1
		0.1	0.1	0.1	0.1	0.1
		0.1	0.1	0.1	0.1	0.1
		0.1	0.1	0.1	0.1	0.1
		0.1	0.1	0.1	0.1	0.1
		0.1	0.1	0.1	0.1	0.1
		0.1	0.1	0.1	0.1	0.1
		0.1	0.1	0.1	0.1	0.1

Figure 4.19: The fitting parameter table for the 21.6 ML film and the annealing experiments.

which includes  $\Delta z_4$ .) The parameter tables are shown in Fig. 4.19, 4.20, and 4.21.

The sample of 0.9 ML Ag deposited at 150K is very hard to fit with the expected coverage. In order to constrain the coverage at 0.9 ML which is confirmed from the annealing measurement fits, the fitting parameters are forced to some extreme values. If the values from 150K sample are excluded, the average island height  $z_{island}=2.14\text{\AA}$ , and the average wetting layer height  $z_{wet}=2.23\text{\AA}$ . The island height value is slightly lower than the wetting layer height value, since our error bar for film and island height is  $\pm 0.15\text{\AA}$ , we conclude that the island and the wetting layer are at the same height of

Parameters	0.9ML_260K	1.8ML_260K	.3ML_300K	.45ML_300K	0.9ML_300K	1.8ML_300K	0.9ML_320K	0.9ML_360K
$S_F$	0.574	0.451	0.595	1.55	1.849	2.113	0.921	0.23
$Z_{\text{island}}$	1.979	2.116		2.18	2.067	2.308	2.066	1.977
$\sigma$	0.000	0.093		0.566	0.000	0.112	0.000	0.000
$Z_{\text{wet}}$	2.187	2.278	2.071	2.068	2.194	2.081	2.205	2.211
$\phi_{\text{wet}}$	0.385	0.207	0.339	0.265	0.203	0.122	0.262	0.368
$\sigma_{\text{wet}}$	0.272	0.000	0.300	0.214	0.328	0.000	0.226	0.461
$\sigma_{\text{sub}}$	0.747	0.460	1.297	1.703	1.080	0.000	1.171	1.097
$\rho_{\text{wet}}$	0.8526	0.4593	1	0.9473	0.8055	0.6113	0.8136	0.8036
$\rho_2$	0.033	0.0788		0	0.0374	0.0324	0.0062	0
$\rho_3$	0.1144	0.3182		0.0413	0.1215	0.0531	0.1596	0.1036
$\rho_4$	0	0.1437		0.0114	0.0337	0.1487	0	0.0696
$\rho_5$		0			0.0019	0.0981	0.0094	0.0056
$\rho_6$		0			0	0.041	0.0112	0.0176
$\rho_7$						0.0104		
$\rho_8$						0.005		
$\rho_9$								
$\rho_{10}$								
$\Delta z_1$	-0.01	-0.0389	-0.0363	-0.0447	-0.0226	-0.0013	-0.0624	-0.0377
$\Delta z_2$	-0.04	-0.0101	-0.0503	0.035	0.0369	-0.0058	-0.0676	-0.0191
$\Delta z_3$	0.02	0.0698	0.1185	0.147	-0.0459	0.0106	0.0458	0.122
$\Delta z_4$	0.08	-0.0014	0.1739	0.0355	-0.0085	0.1102	0.0347	0.0937
$z_5$	1.58	1.58	1.58	1.717	1.58	1.58	1.58	1.58
$\zeta_1$	0.1	0.1	0.1	0	0.1	0.1	0.1	0.1
$\zeta_2$	0.1	0.1	0.1	0.15	0.1	0.1	0.1	0.1
$\zeta_3$	0.1	0.1	0.1	0.09	0.1	0.1	0.1	0.1
$\zeta_4$	0.1	0.1	0.1	0.1	0.1	0.1	0.1	0.1
$\zeta_5$	0.1	0.1	0.1	0.08	0.1	0.1	0.1	0.1

Figure 4.20: The fitting parameter table for specular reflectivity measurements.

Parameters	1.8ML_360K	2.7ML_360K	1.8ML_400K	Parameters	0.9ML_360K	Ag (1,1) <sub>H</sub>	Ag (1,0) <sub>H</sub>	Parameters
S <sub>F</sub>	0.436	0.546	0.637	S <sub>F</sub>	1.33	0.13	0.0424	S <sub>F</sub>
Z <sub>island</sub>	2.097	2.17	2.148	Z <sub>island</sub>	2.032			Z <sub>island</sub>
σ	0.113	0.089	0.085	σ	0.042	0.219	0.115	σ
Z <sub>wet</sub>	2.252	2.317	2.357	Z <sub>wet</sub>	2.167			Z <sub>wet</sub>
ϕ <sub>wet</sub>	0.275	0.19	0.181	ϕ <sub>wet</sub>	0.213			ϕ <sub>wet</sub>
σ <sub>wet</sub>	0.209	0.194	0.280	σ <sub>wet</sub>	0.378			σ <sub>wet</sub>
σ <sub>sub</sub>	0.942	0.635	0.966	σ <sub>sub</sub>	0.341	0.231	0	σ <sub>sub</sub>
ρ <sub>wet</sub>	0.6783	0.6131	0.7349	ρ <sub>wet</sub>	0.8239	0.0218	0.0218	ρ1
ρ2	0	0	0	ρ2	0.002	0.0231	0.0231	ρ2
ρ3	0.078	0.0422	0.0246	ρ3	0.0959	0.0752	0.0752	ρ3
ρ4	0.0387	0.0299	0.0298	ρ4	0.0361	0.0433	0.0433	ρ4
ρ5	0.068	0.0328	0.0411	ρ5	0.0229	0.0191	0.0191	ρ5
ρ6	0.0828	0.0692	0.0458	ρ6	0.0108	0.0122	0.0122	ρ6
ρ7	0.0282	0.1061	0.0494	ρ7	0.0084	0.0091	0.0091	ρ7
ρ8	0.0161	0.0691	0.041	ρ8				ρ8
ρ9	0	0.0257	0.0186	ρ9				ρ9
ρ10	0.0099	0.0119	0.0148	ρ10				ρ10
Δz1	-0.0935	-0.0482	-0.0556	Δz1	-0.0542	1	4.107	(H,K) S <sub>F</sub>
Δz2	-0.1054	-0.0768	-0.0347	Δz2	-0.0235	0	3.836	(K,H) S <sub>F</sub>
Δz3	0.1011	0.0481	0.1007	Δz3	-0.1141			
Δz4	-0.031	-0.0158	-0.0444	Δz4	-0.0863			
z5	1.58	1.58	1.58	z5	1.58			
ζ1	0.1	0.1	0.1	ζ1	0.1			
ζ2	0.1	0.1	0.1	ζ2	0.1			
ζ3	0.1	0.1	0.1	ζ3	0.1			
ζ4	0.1	0.1	0.1	ζ4	0.1			
ζ5	0.1	0.1	0.1	ζ5	0.1			

Figure 4.21: The fitting parameter table for specular reflectivity measurements. The fitting parameters for specular reflectivity and truncation rod measurements for 0.9 ML deposited at 360K are also shown.

$2.18 \pm 0.15 \text{ \AA}$ . Similarly excluding some special cases, the average island height roughness is  $\sigma = 0.1 \pm 0.05 \text{ \AA}$ , the average wetting layer roughness is  $\sigma_{wet} = 0.3 \pm 0.1 \text{ \AA}$ , and the substrate roughness  $\sigma_{sub} = 0.9 \pm 0.4 \text{ \AA}$ , which happens to agree with the parameter ranges from 0.3 ML data fits.

We are not very sensitive to the Si 7x7 parameters when there is enough FCC Ag film. But when we are sensitive to the Si 7x7 parameters at low coverage of 0.3 ML and 0.45 ML, we did not count long enough to get good statistics. The Si 7x7 parameters of the 0.45 ML fit in the table have different  $\zeta_j$  and  $z_5$  values than the rest of the fits. They are from an old fitting setup for Si 7x7. Since we do not have accurate data in the region sensitive to the Si 7x7 parameters for 0.45 ML, the parameters are just kept in the old setup. After fitting all the samples, the range 7x7 parameters vary is  $\Delta z_1 = -0.05 \pm 0.05 \text{ \AA}$ ,  $\Delta z_2 = -0.03 \pm 0.07 \text{ \AA}$ ,  $\Delta z_3 = 0.04 \pm 0.09 \text{ \AA}$ , and  $\Delta z_4 = 0.03 \pm 0.09 \text{ \AA}$ . For comparison, the values measured by Robinson from one Si 7x7 sample[34] are  $\Delta z_1 = -0.01 \pm 0.03 \text{ \AA}$ ,  $\Delta z_2 = -0.04 \pm 0.03 \text{ \AA}$ ,  $\Delta z_3 = 0.02 \pm 0.03 \text{ \AA}$ ,  $\Delta z_4 = 0.08 \pm 0.03 \text{ \AA}$ , and  $\Delta z_5 = 0.88 \pm 0.20 \text{ \AA}$  (equivalent as  $z_5 = 1.58 \text{ \AA}$ ). The roughness values from Robinson's measurement are given as  $\zeta_2 = 0.15 \pm 0.05 \text{ \AA}$ ,  $\zeta_3 = 0.09 \pm 0.07 \text{ \AA}$ ,  $\zeta_4 = 0.10 \pm 0.09 \text{ \AA}$ ,  $\zeta_5 = 0.08 \pm 0.16 \text{ \AA}$ . The sample where we measured both specular reflectivity and Ag truncation rod (0.9 ML at 360K) is created in a different run from all other samples, so its parameters are slightly different.

## 4.5 The absence of Ag lattice expansion

Our x-ray scattering investigation shows no evidence of an expanded Ag lattice in the islands. Recall that Unal et al. noticed that theirs as well as other STM studies[5,

16, 17] find a 12% Ag lattice expansion for first two atomic layers in the island (it was called a bilayer on top of the wetting layer). However, our x-ray scattering data can be explained by the conventional bulk lattice spacing of Ag whereas a 12% expanded Ag lattice would be easily detected in our measurements. This point is demonstrated in Fig. 4.22 which shows the experimental reflectivity data from a sample that has predominantly 3-layer islands (0.9 ML deposited at 300K). The solid curve utilizes the conventional Ag lattice constant and it provides an excellent fit to the data. By contrast, the dashed curve uses a 12% expanded lattice, taking  $d_1 = d_2 = 1.12d_{Ag}$ , and it dramatically misses the data.

In an effort to seek an alternative explanation for the discrepancy, we tried a model that raises the island position relative to the substrate. Because STM measures the distance between the wetting layer and the top of the island, STM cannot distinguish between a Ag lattice expansion and a case where the islands lift off of the substrate, presumably by 12%, but keep the conventional Ag lattice constant. In fact, x-ray scattering studies have found that Pb islands pull away from the substrate, relative to the wetting layer, when they form in the Pb/Si(111)7x7 system[28]. However, Fig. 4.22 demonstrates that this situation does not occur for Ag/Si(111)7x7. The dotted curve shows the predicted reflectivity for Ag islands having the conventional lattice constant but raised from the substrate by an amount required to give the 12% expansion observed by STM ( $z_{island} = z_{wet} + 0.6\text{\AA}$ ). As can be seen, the dotted curve significantly misses the data. (The plotted curves are not fits, if we fit the data with the constraints  $d_1 = d_2 = 1.12d_{Ag}$  or  $z_{island} = z_{wet} + 0.6\text{\AA}$ , we could get better results than what is plotted in the figure. But the results are always worse than our best fit without the constraints.) Therefore, we conclude that the Ag islands exhibit the



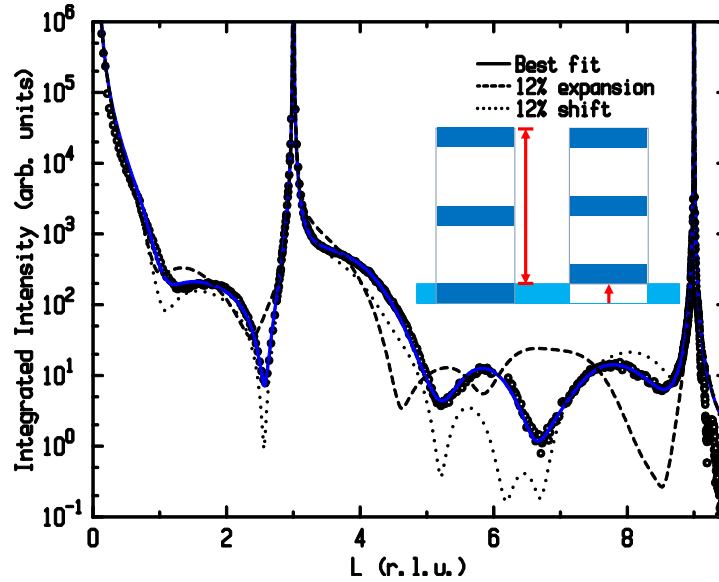


Figure 4.22: Using 0.9 ML Ag deposited at 300K, which exhibits predominantly 3-layer islands, it is demonstrated that the Ag interplanar spacing is the same as for bulk Ag. The solid curve is the best fit using the bulk Ag lattice constant. The long-dashed curve assumes a 12% expansion of the Ag lattice whereas the dotted curve assumes that the islands are vertically displaced from the substrate by an amount that would be equivalent to the height resulting from a 12% lattice expansion. The inset illustrates the two cases schematically.

conventional lattice constant for FCC Ag and, moreover, the Ag wetting layer and the islands exhibit a similar height from the substrate.

X-ray scattering directly measures the core electron positions, it is very sensitive to small changes in distance, the 12% expansion or displacement represents an enormous effect that is not observed in our experiments. We therefore conclude that Ag has the conventional bulk lattice spacing and suggest that the STM measurements are affected by the difference between the electronic properties of the islands and the Ag wetting layer. In particular, the Ag wetting layer contains a low density of Ag, which might lead to a smaller tunneling efficiency into the wetting layer. That would require the STM tip to be closer to the wetting layer than when measuring near the top of

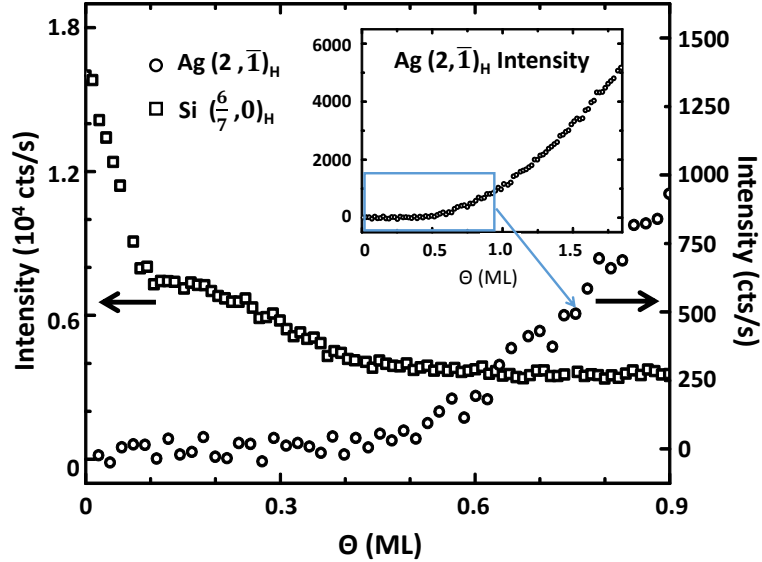


Figure 4.23:  $(\frac{6}{7}, 0)_H$  and  $\text{Ag}(2, \bar{1})_H$  intensity at  $L=0.1$  as a function of Ag coverage during deposition at 360K and 300K, respectively. FCC Ag islands begin to form only after the wetting layer structure saturates.

the electronically denser islands, thereby leading to an apparent expansion of the Ag islands when their heights are measured relative to the wetting layer.

## 4.6 Ag wetting layer and transition to FCC islands

Ag initially wets the  $\text{Si}(111)7 \times 7$  reconstructed surface and after certain coverage FCC islands start to form. When does the Ag wetting layer saturate, when does the Ag FCC island start to form, and what happens to the Ag wetting layer when the FCC islands form?

Fig. 4.23 shows the coverage dependence, at  $L=0.1$ , of the  $(\frac{6}{7}, 0)_H$  intensity for the reconstructed surface along with the  $\text{Ag}(2, \bar{1})_H$  intensity that is representative of FCC Ag. The  $(\frac{6}{7}, 0)_H$  intensity changes with coverage as Ag is incorporated commensurately

into the Si(111)7x7 surface until the wetting layer structure saturates near a coverage of  $\sim 0.4$  ML and therefore completely wets the substrate. Note that the intensity of the  $(\frac{6}{7}, 0)_H$  peak stops changing at the saturation coverage but it does not vanish, indicating that there is a saturated Ag/Si(111)7x7 wetting layer structure.

Additional evidence for the saturating wetting layer structure was obtained by measuring a series of many seventh-order diffraction intensities,  $(H, K, 0.1)_H$ , as a function of coverage, in 0.1 ML increments (it takes  $\sim 20$  minutes to do the deposition and perform the measurements for each step) as shown in Fig. 4.24 and 4.25. In Fig. 4.26 where each diffraction intensity is normalized by its value measured at 0.5 ML coverage, it can be seen that all of the intensities vary strongly up to a coverage of  $\sim 0.4$  ML whereas there is negligible intensity change in intensity at higher coverage. Therefore the wetting layer neither changes its structure nor absorbs more Ag for a coverage above  $\sim 0.4$  ML.

Fig. 4.23 also shows that Ag islands start form above a coverage of 0.4 ML, which is consistent with previous STM studies of Ag/Si(111)7x7[5, 15, 17, 42]. The incommensurate FCC Ag $(2, \bar{1})_H$  truncation rod intensity emerges at the coverage for which the wetting layer structure saturates. Therefore, the wetting layer is the most stable Ag structure on the Si(111)7x7 surface and the FCC Ag islands form in coexistence with the saturated wetting layer structure.

We now turn to the interfacial atomic layer of Ag that lies between the island and the substrate (the cross-hatched layer in Fig. 4.1). To investigate the structure of that layer, specular reflectivity and Ag crystal truncation rods are measured on the same sample, which is prepared by depositing 0.9 ML of Ag on Si(111)7x7 at 360K. As discussed in chapter 3, specular reflectivity is sensitive to all of the Ag atomic layers

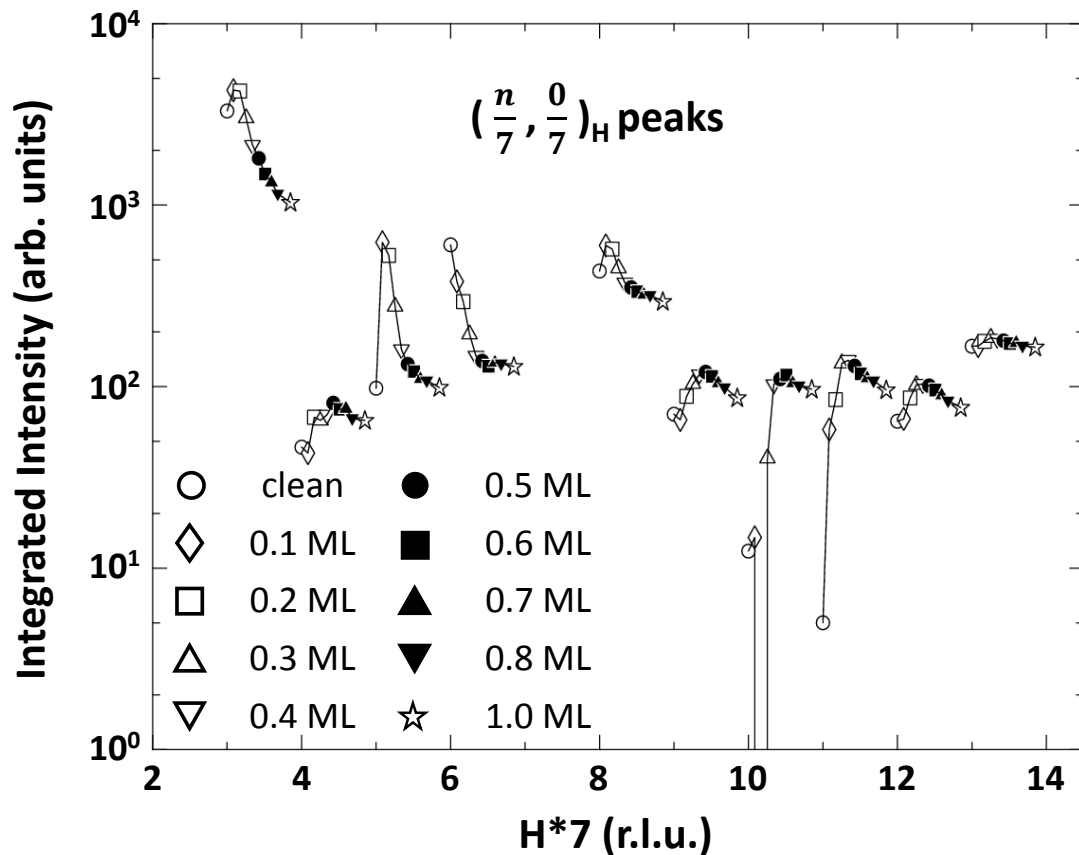


Figure 4.24: Si  $(\frac{n}{7}, \frac{0}{7})_H$  diffraction intensities measured as a function of coverage at 360K. The measured intensity is normalized by the upstream monitor, then Lorentz fitting is used to calculate the integrated intensity from the transverse scans. The first point is plotted at the h value of the measurement and the data points to the right, connected by lines, are for different coverages as indicated in the key.

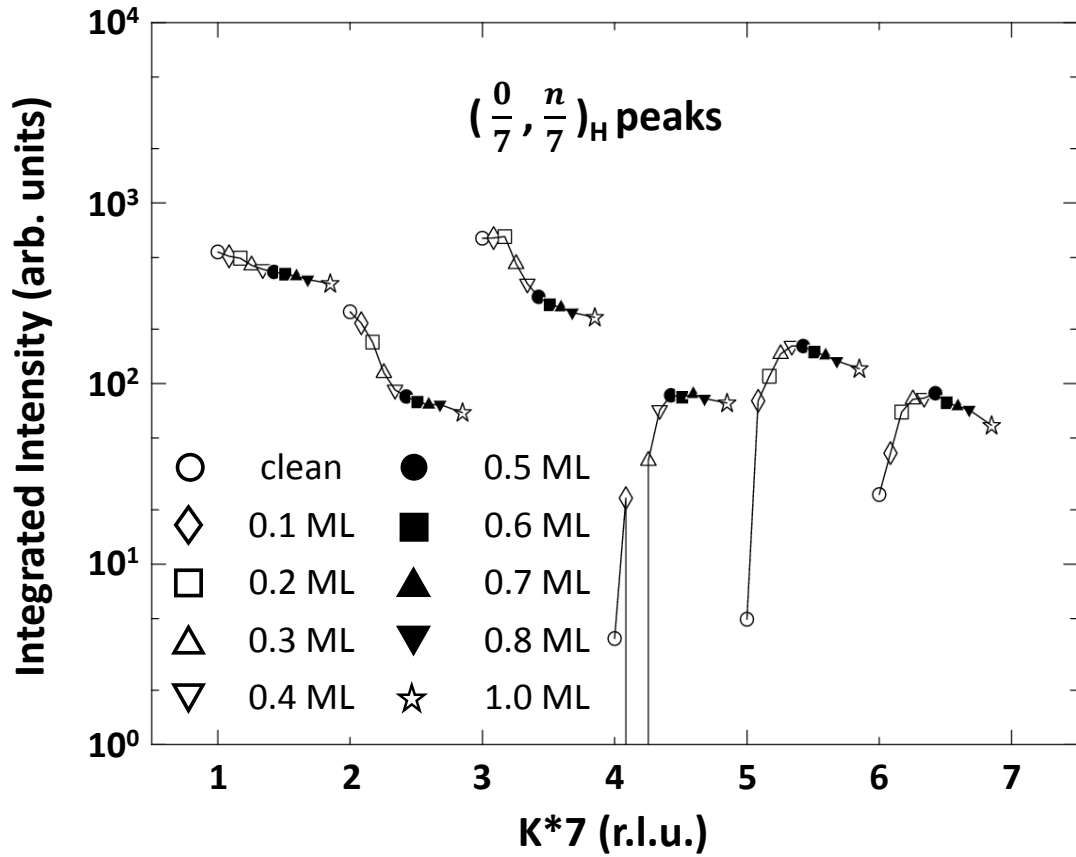


Figure 4.25: Si  $(\frac{0}{7}, \frac{n}{7})_H$  diffraction intensities measured as a function of coverage at 360K. The measured intensity is normalized by the upstream monitor, then Lorentz fitting is used to calculate the integrated intensity from the transverse scans. The first point is plotted at the k value of the measurement and the data points to the right, connected by lines, are for different coverages as indicated in the key.

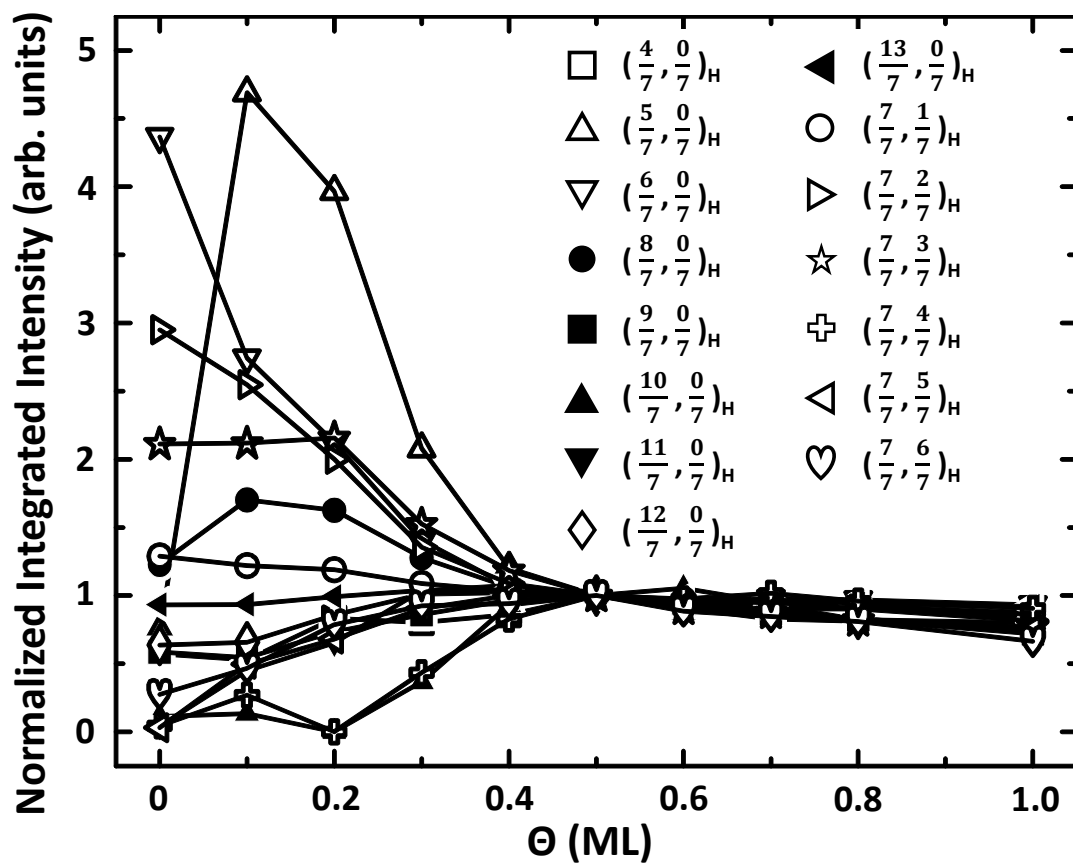


Figure 4.26: Seventh-order diffraction intensities measured as a function of coverage at 360K. The intensity of each reflection is normalized by its value at 0.5 ML. All intensities exhibit a strong variation below 0.4 ML, indicating the development and evolution of the Ag wetting layer that is commensurate with the Si(111)7x7. This evolution does not occur above 0.4 ML as the Ag wetting layer structure saturates and completes.

(wetting layer as well as the FCC islands), whereas the Ag crystal truncation rod is sensitive only to the atomic layers of the Ag islands that possess the FCC in-plane structure. By comparing the island height distribution from both specular reflectivity and the truncation rod, we would be able to determine the structure of the first layer of the Ag islands. If the first layer of the Ag islands is wetting layer structure, then the overall height profile from the Ag truncation rod will be one layer less than the profile from the specular reflectivity. Thus  $p_j$  distribution will be shifted by 1 in  $j$  between two measurements,  $p_j$  from the specular reflectivity should match the value of  $p_{j-1}$  from the truncation rod. If the first layer of the Ag islands is FCC structure, then we would expect identical  $p_j$  distributions from the specular reflectivity and the rod.

The reflectivity shown in Fig. 4.27a exhibits predominantly three atomic layers of Ag. As shown in Fig. 4.27b, the  $\text{Ag}(1,1)_H$  rod exhibits a single subsidiary maximum between Bragg peaks, similar to the reflectivity, indicating that there are predominantly three atomic layers of FCC Ag. Therefore, the FCC Ag islands are three atomic layers thick and because that is the same thickness as found in the reflectivity, the islands must start at the substrate, rather than on top of the wetting layer.

Fig. 4.27c quantitatively compares the island height distributions,  $p_j$ , from independently fitting the specular reflectivity and the  $\text{Ag}(1,1)_H$  crystal truncation rod data. As can be seen, the two height distributions are nearly identical for the heights of  $p_2$  and higher that correspond only to the incommensurate FCC Ag islands. To make the comparison, the height distribution determined from the truncation rod was normalized so that it has the same  $\sum_{j=2} p_j$  as that obtained from the specular reflectivity. This was necessary because the reflectivity determines  $p_j$  absolutely

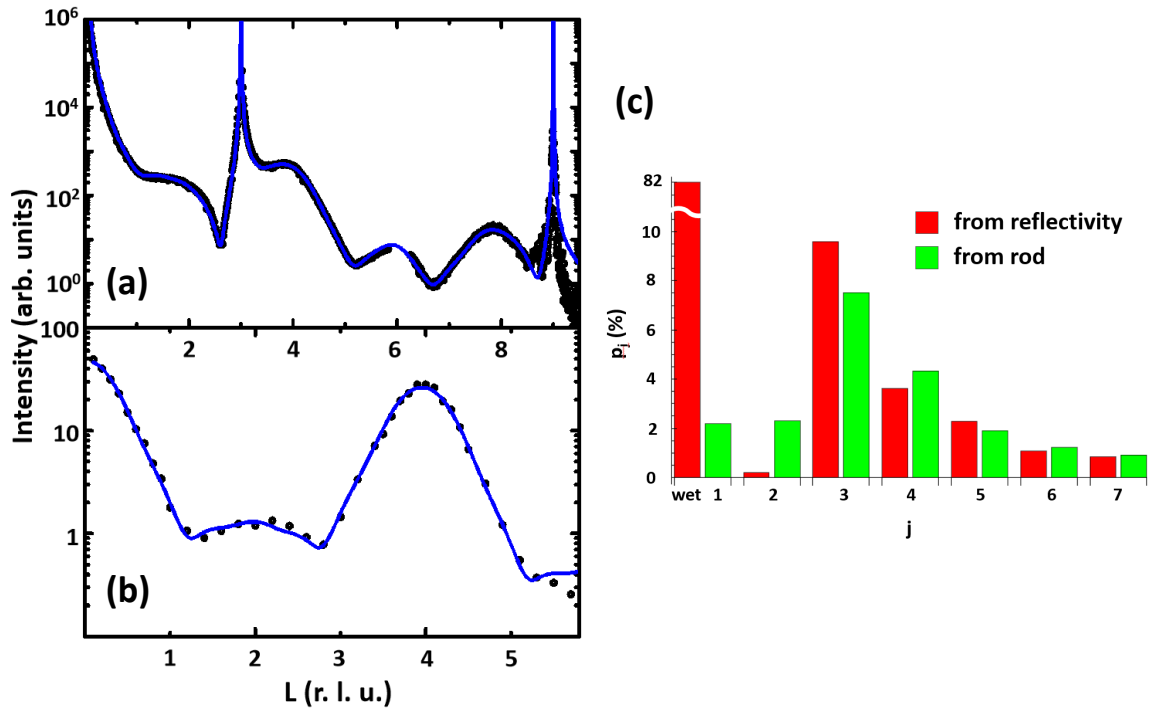


Figure 4.27: Specular reflectivity and crystal truncation rod measurements from a sample having 0.9 ML Ag on Si(111)7x7 deposited at 360K. (a) Specular reflectivity, (b) Ag(1,1)<sub>H</sub> rod measured with fixed incident angle (after geometry correction). Solid curves are the best fit. (c) Comparison of the island height distribution,  $p_j$ , obtained from the specular reflectivity and the crystal truncation rod measurements. The two measurements yield nearly identical height distributions, indicating that the FCC Ag islands extend to the substrate interface rather than reside on top of the wetting layer.



whereas the rod leaves an unknown scale factor. Of course,  $p_1$  obtained from the specular reflectivity is very large because it includes the wetting layer that covers the majority of the surface. Interestingly, there is a small but non-zero  $p_1$  (2% coverage) from the truncation rod measurement, which we suggest might arise from a small amount of re-ordering of the commensurate wetting layer into incommensurate Ag in the immediate proximity of the island, perhaps in the form of a narrow annular ring around the island.

We conclude that the first layer of the incommensurate FCC Ag islands is located within the same layer as the commensurate Ag wetting layer so that the FCC Ag islands are in direct contact with the substrate – the islands do not reside on top of the commensurate Ag wetting layer. Our results also imply that the formation of Ag FCC islands converts the commensurate Ag 7x7 wetting layer directly beneath the island into the FCC structure of the Ag island. Indeed, this loss of wetting layer can be detected in the coverage-dependence of the seventh order diffraction intensity from the wetting layer. From Fig. 4.27 we estimate that  $\sim 20\%$  of the surface is covered by islands at 0.9 ML coverage, which is in good agreement with the slow decrease of the seventh-order diffraction intensity between 0.5 and 1.0 ML in Fig. 4.26.

## 4.7 Ag domain rotation

### 4.7.1 60 degree rotation

Ag(111) domain rotations is observed in our experiments. Fig. 4.28 shows the measurement of the  $\text{Ag}(1,0)_H$  crystal truncation rod on the sample of 0.9 ML deposition

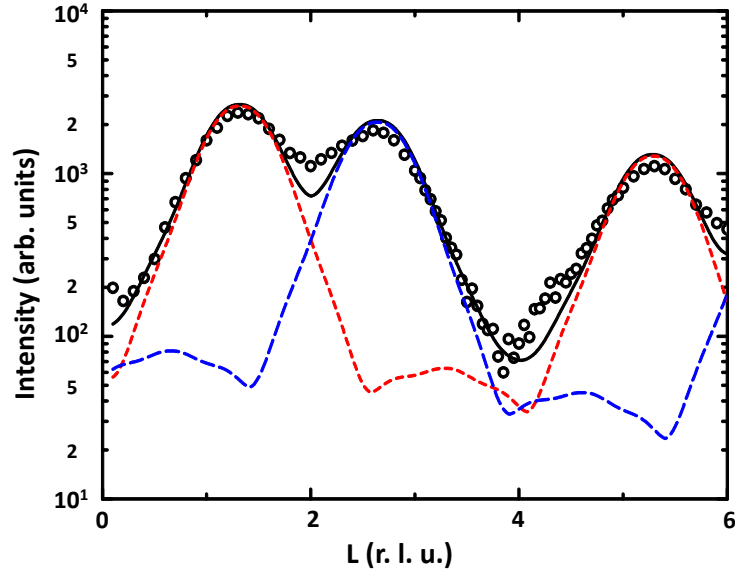


Figure 4.28: Ag  $(1,0)_H$  crystal truncation rod measurement (after geometry correction) done with fixed exit angle on the sample having 0.9 ML Ag on Si(111)7x7 deposited at 360K. The solid curve is the best fit. The dashed curves show the relative contributions of Ag $(1,0)_H$  (shorter dash) and Ag $(0,1)_H$  (longer dash) rods due to the 60-degree rotated domains.

at 360K where both specular reflectivity and truncation rod are measured.

Unlike the Ag $(1,1)_H$  rod, which is six-fold symmetric, the Ag $(1,0)_H$  rod is three-fold symmetric with Bragg peaks expected at  $L=1.328$  and  $L=5.311$  ( $L=1$  and  $4$  in Ag coordinates) along the rod. However, it can be seen that there is an additional peak at  $L=2.656$  observed in Fig. 4.28, which corresponds to the related, but inequivalent, Ag $(0,1)_H$  rod. The fitted curve uses the  $p_j$  distribution obtained from the fit to the Ag $(1,1)_H$  rod along with approximately equal contributions (4.1 to 3.8 ratio) of the Ag $(1,0)_H$  and Ag $(0,1)_H$  rods. Therefore, the Ag islands consist of 60-degree rotated domains, which is consistent with the nucleation of FCC islands on the six-fold symmetric Si(111)7x7.

### 4.7.2 15.7 degree rotation

Another type of Ag(111) domain rotation is also observed. Fig. 4.29 shows an azimuthal scan performed at  $L=0.1$  along a circle in the HK plane having the radius of  $\text{Ag}(1,1)_H$  for bulk Ag. It reveals the orientational alignment of the islands relative to the substrate. The large peaks are 60 degrees apart and reveal that the FCC Ag islands are aligned along the substrate crystallographic axes such that the  $\text{Ag}[1,1]_H$  and  $\text{Si}[1,1]_H$  are parallel. The 60 degree separation is also consistent with the six-fold symmetry expected for the  $\text{Ag}[1,1]_H$  rod. The width of these peaks correspond to an orientational disorder (mosaicity) of  $\sim 3.7$  degrees in the plane of the surface; orientational fluctuations do not occur out of the surface plane.

By contrast, the commensurate Ag wetting layer is perfectly aligned orientationally with the  $\text{Si}(111)7\times 7$ , which has narrow ( $\sim 0.03$  degrees) seventh-order peaks, as shown in Fig. 4.30. These peaks do not broaden with Ag deposition indicating that, as the wetting layer is formed, Ag decorates the  $\text{Si}(111)7\times 7$  without reducing the original domain size.

Fig. 4.29 also shows weaker “satellite” peaks having an orientation  $15.7 \pm 0.2^\circ$  on either side of the  $\{1,1\}_H$  directions and it reveals a smaller population, about 18%, of rotated islands. The main peak and the satellites exhibit the same radial position, as shown in Fig. 4.31, indicating that the satellites are due to truly rotated domains rather than a superstructure: both populations of Ag islands are observed to have the conventional in-plane Ag lattice constant to within our resolution of  $\pm 0.3\%$ .

Satellites are also observed at the same rotation angle when Ag is deposited at temperatures lower than in Fig. 4.29, although, the satellite intensities are weaker. Therefore, the population of the rotated domains decreases with decreasing temper-

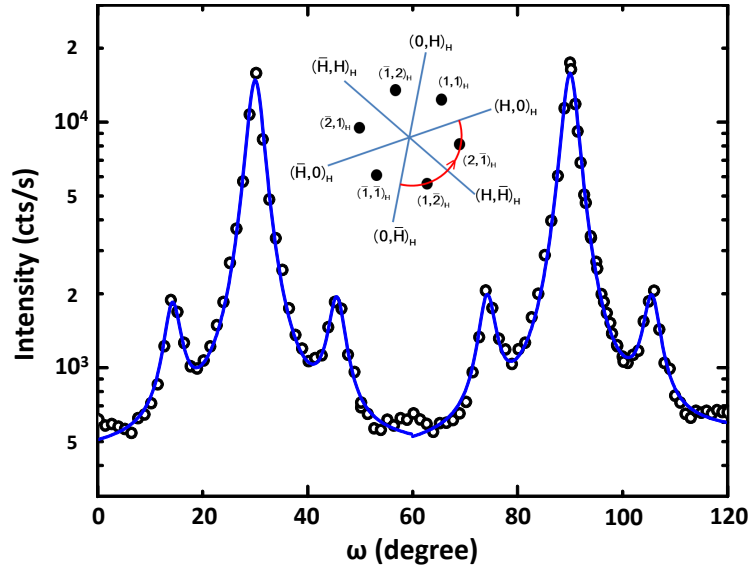


Figure 4.29: A scan performed azimuthally at  $L=0.1$  in the HK plane with the scattering vector magnitude fixed at  $\text{Ag}(1,1)_H$  for a sample where 1.8 ML of Ag was deposited at 400K. The peaks at 30 degrees and 90 degrees are the  $\text{Ag}(1,2)_H$  and  $\text{Ag}(2,1)_H$  reflections, respectively, which are equivalent by symmetry to the  $\text{Ag}(1,1)_H$ . The smaller peaks correspond to a low population of Ag islands that are rotated by  $\pm 15.7$  degrees relative to the orientation of the majority population. The solid curves are six Lorentzians, all having the same FWHM of 3.7 degrees, fitted to the data. The inset shows the scan direction in the HK plane.

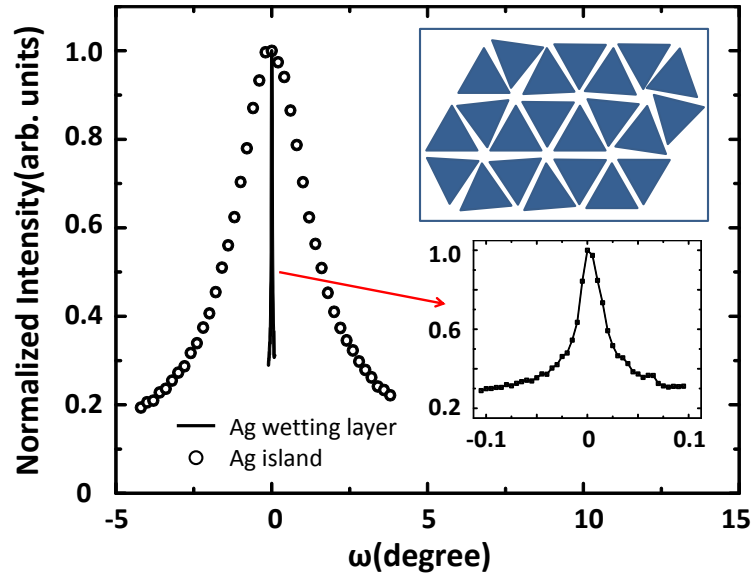


Figure 4.30: The large in-plane orientational disorder of the FCC Ag islands is observed by comparing scans performed azimuthally in the surface plane through the  $\text{Ag}(2, \bar{1})_H$  peak of the FCC Ag islands and the  $(\frac{8}{7}, 0)_H$  peak of the Ag/Si(111)7x7 wetting layer at  $L=0.1$ . The  $\eta$  scan through  $\text{Ag}(2, \bar{1})_H$  peak is almost identical with the azimuthal scan shown in Fig. 4.29, although they are measured on the same sample surface, they are not the exact same data. The Ag island peak extends more than 3 degrees, which is two orders of magnitude broader than the Ag wetting layer that is commensurate with the Si(111)7x7. The upper inset schematically shows the Ag island mosaicity in the surface plane. The lower inset provides an expanded view of the Ag wetting layer peak.

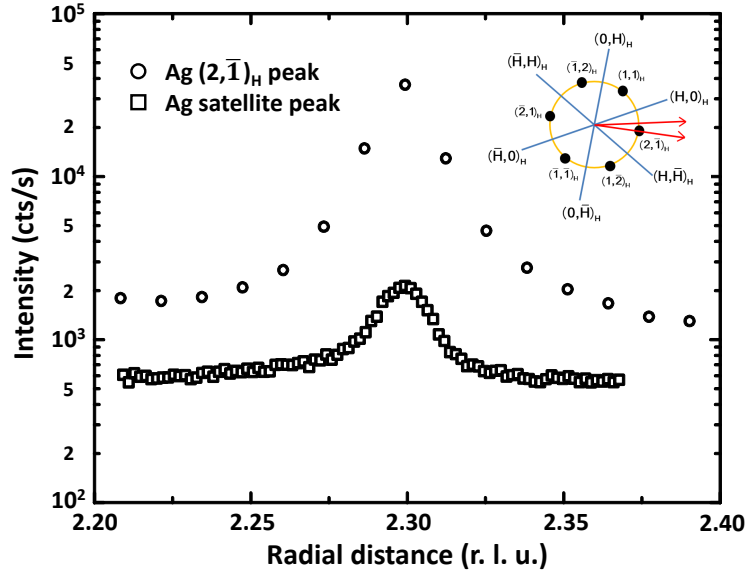


Figure 4.31: Radial scans at  $L = 0.1$  through the  $\text{Ag}(2, \bar{1})_H$  peak and its neighboring 15.7-degree rotated peak demonstrate that their corresponding island populations have the same lattice constant, which is that of bulk Ag. The inset shows the directions of the radial scans in the HK plane.

ature, suggesting a kinetic barrier to their formation.

We suggest that the strength of the interaction at the interface between the FCC Ag islands and the substrate is weak relative to the energy scale of the commensurate Ag wetting layer interaction with the  $\text{Si}(111)7 \times 7$ . It is noted that the wetting layer always forms completely before the islands appear, therefore, indicating that the Ag in the wetting layer interacts more strongly with the substrate. Finally, this weaker interaction is also revealed by the mosaicity of the islands.

### 4.7.3 Coincidence Site Lattice calculations

It is interesting to speculate on the epitaxial relationship of the small population of domains that are rotated relative to the substrate. If we rotate two lattices on top

of each other, for certain angles some lattice points of lattice 1 coincide exactly with some lattice points of lattice 2. This kind of superstructure is called coincidence site lattice (CSL). CSL theory is often used for calculating grain boundaries between the same material, here we will apply the concept of CSL to calculate Ag(111) rotated on top of Si(111).

In a 2D hexagonal coordinate system as shown in Fig. 3.4b, the length of a vector  $\vec{R} = n_1\vec{a}_1 + n_2\vec{a}_2$  is given as  $R = a\sqrt{n_1^2 + n_2^2 - n_1n_2}$  where  $|a_1| = |a_2| = a$ . In order to find possible coincidence site lattices for all rotations, we only need to explore whether there are two different pairs of values for  $n_1$  and  $n_2$  that give the same length  $R$ . If such pairs exist, we have two different vectors  $\vec{R}_1$  and  $\vec{R}_2$  with the same length  $R$ , the two vectors coincide with each other after a rotation of angle  $\theta = \cos^{-1}\frac{\vec{R}_1 \cdot \vec{R}_2}{R^2}$ .

The in-plane lattice constants are taken as  $a_{Si} = \frac{5.431}{\sqrt{2}} \text{ \AA}$ , and  $a_{Ag} = \frac{4.090}{\sqrt{2}} \text{ \AA}$ . The lattice constant ratio of Si to Ag is 4:3 to within 0.4%. Fig. 4.32 illustrates this close alignment for the unrotated domains, which is the majority population of domains observed in the measurement of Fig. 4.29.

We calculated all possible coincidence site lattices with supercells containing less than 100 atoms ( $R^2 < 100$  in Si lattice unit). Accepting only those for which the ratio of supercell areas ( $R^2$ ) is the same to within  $\pm 1\%$ , we have found a 15.8 degree rotated coincidence domain that is very close to the 15.7 degrees found experimentally, schematically shown in Fig. 4.32. The next two possible coincidence domain rotations nearby are 14.4 degrees and 16.6 degrees, schematically shown in Fig. 4.33. A Si(111)7x7 cell is drawn to compare with the size of Ag supercell in the figures. As can be seen, the 15.8-degree rotated supercell is quite close in area to the 7x7, although it is slightly smaller.

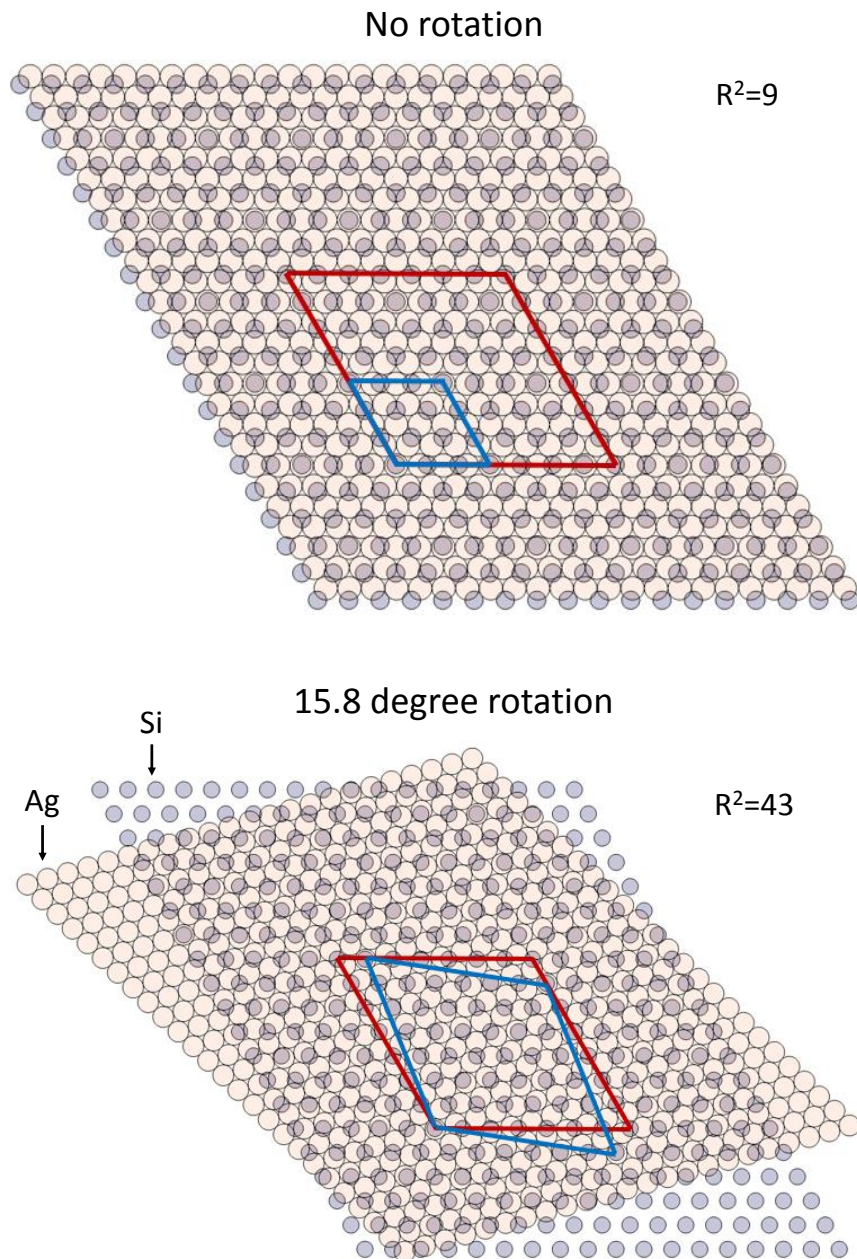
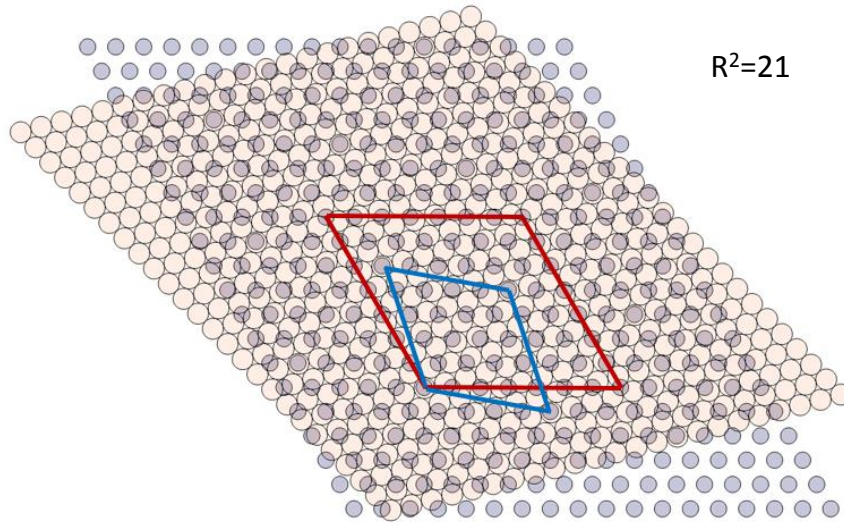


Figure 4.32: Schematic diagram showing the coincidence lattices of Si(111) and Ag(111), which have lattice constants in the ratio of 4:3. The large circles are Ag and the smaller circles are Si. Coincidence lattices without rotations are shown, and coincidence lattices rotated by 15.8 degrees are also shown. The Ag supercell is shown in blue, and a Si(111)7x7 unit cell is shown in red for reference. The size of the supercell is indicated by the number of Si atoms, represented by  $R^2$ . As can be seen, the size of the Ag supercell for 15.8 degree rotation is close to the size of a Si(111)7x7 unit cell.



14.4 degree rotation



16.6 degree rotation

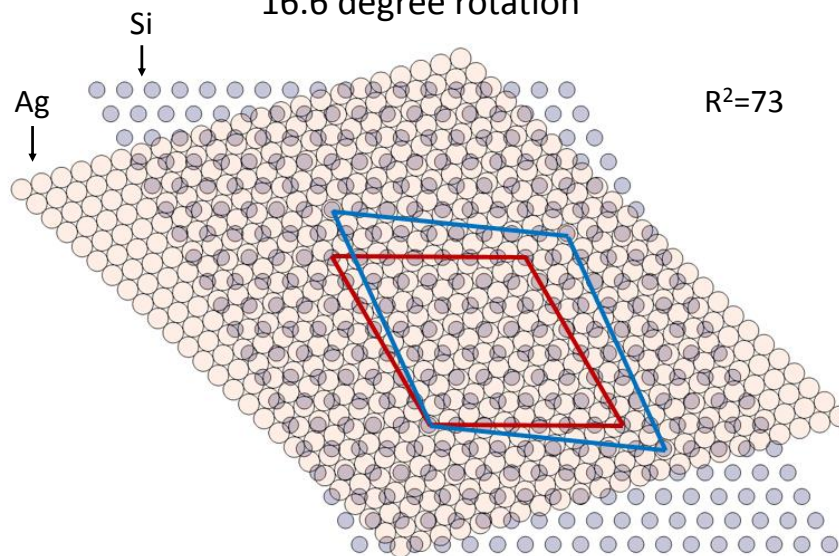


Figure 4.33: Schematic diagram showing the coincidence lattices of Si(111) and Ag(111), with the rotation of 14.4 and 16.6 degrees. The Ag supercell is shown in blue, and a Si(111)7x7 unit cell is shown in red for reference. The size of the supercell is indicated by the number of Si atoms, represented by  $R^2$ .

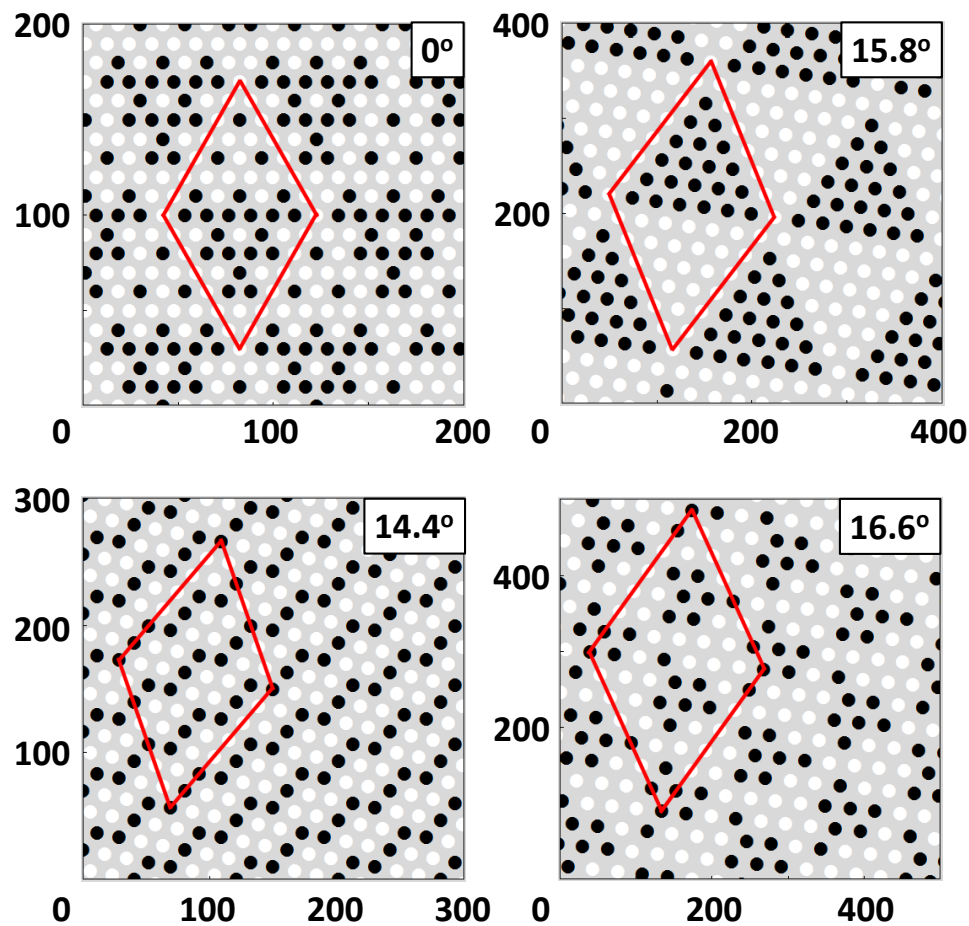


Figure 4.34: The coincidence of Ag supercells with the Si 1a layer are shown for 4 different rotation angles: 0 degrees; 14.4 degrees; 15.8 degrees; and 16.6 degrees. All circles represent the corners of the Ag supercells and the filled circles show where the Ag supercells are coincident with the Si 1a atomic positions. The numeric scale on the axes is given in units of Angstroms. The solid lines outline periodic domains that result from the Ag coincidence lattice superimposed on the 7x7 period. It can be seen that clusters of coincident supercells occur for 0 degree and 15.8 degree rotations but not for 14.4 degree and 16.6 degree.

We also looked into how Ag supercells match with the Si 7x7 structure. Fig. 4.34 shows points of coincidence of the corners of Ag supercells with Si 1a positions. Interestingly, from the Ag coincidence lattice superimposed on the 7x7 period, there are always 21 out of 49 corners of the Ag supercells that are coincident with Si 1a positions, as indicated by the red lines in the figure. But it is striking that relatively large clusters of coincident supercells are only present for the 0 degree and 15.8 degree rotation but not for the nearby 14.4 degree and 16.6 degree rotation. This superimposed periodicity of coincidence may extend to infinity if there is no lattice mismatch. Because the lattice mismatch is bigger for the unrotated case than for the three rotated cases, it can be seen that the coincidence already disappear near the edges of the plotted area for the 0 degree rotation. The coincidence may come back after a long distance which is not shown in the plot, because the lattice mismatch does not mess up the periodicity of coincidence.

## 4.8 Conclusion: Explanation for the height selection

Our in situ x-ray scattering experiments demonstrate that the minimum preferred island height is a *trilayer* rather than the *bilayer* that has been widely assumed in the literature. But we still have to answer the question: what caused the height selection?

Our experiments did not observe the expansion of the Ag inter-atomic layer spacing. Without the anomalous lattice expansion, an *oscillating* energy landscape arising from QSE will not explain the minimum nanocrystal thickness of Ag(111) on Si(111)

7x7. However, we now show that QSE determines the preferred minimum crystal thickness, although, the interface and a different energy landscape must be considered. At the interface there will be equilibrium between the wetting layer and the FCC nanocrystal phases. Because the commensurate wetting layer completes first, its energy/area is significantly lower than for *any* thickness of incommensurate Ag(111). After the wetting layer phase saturates, FCC Ag nanocrystalline islands form upon further coverage, although, not on top of the Ag wetting layer because that interfacial energy is apparently unfavorable as shown by experiment. Instead, the local wetting layer dissolves and it is replaced by incommensurate FCC Ag islands that are in weaker contact with the substrate – there is a coexistence between these two phases.

The important role of quantum confinement is revealed by the excellent agreement between our experimentally observed island height distributions and recent density functional theory (DFT), which includes the effect of electron confinement, performed for free-standing Ag(111) films by Han and Liu [44]. The DFT shows (see Fig. 4.35b) that the energy/area is essentially independent of thickness for layers having 3 ML or more – there is no oscillation with thickness. Including a much lower-energy commensurate wetting layer (not considered in the DFT) will lead to a two-phase coexistence line between the wetting layer and islands having 3 ML or more. At the lowest temperatures, 3 ML will be the thinnest preferred thickness. At higher temperatures, thicker layers will be populated as the mobility increases, which agrees with our experimental observation in Fig. 4.11. It should be noted that a strong substrate interaction, which is apparently small here, can change the growth behavior. Indeed, if a stronger *commensurate* interaction with the substrate is assumed, DFT

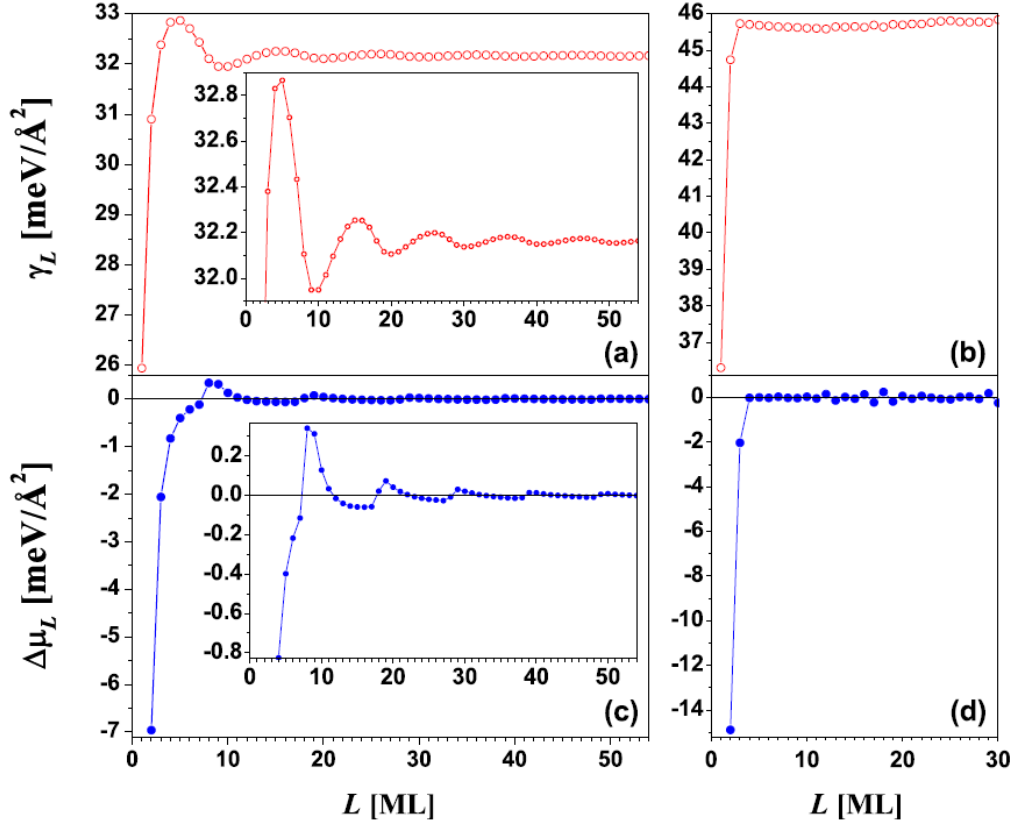


Figure 4.35: Surface free energy  $\gamma_L$  versus Ag(111) nanofilm thickness  $L$  from (a) electron-gas model without charge spilling (EGM) and (b) density functional theory (DFT) calculations, respectively. Stability index  $\Delta\mu_L$  versus  $L$  from (c) EGM and (d) DFT calculations, respectively. The insets in (a) and (c) provide expanded views.

The surface free energy of a nanofilm is defined as  $\gamma = \frac{E - NZ\sigma_{bulk}}{2A}$  and calculated at discrete thickness  $L$ .  $E$  is the total energy of a periodic  $D \times D$  supercell,  $NZ$  is the total electron number in the supercell,  $A = D^2$  is the area of the bottom or top face of the supercell, and  $\sigma_{bulk} = \frac{3}{5}E_F$  is the energy per electron for bulk metal from the Drude-Sommerfeld model.

The stability index is defined as  $\Delta\mu_L = \frac{E_{L+1} + E_{L-1} - 2E_L}{A}$ . For  $\Delta\mu_L < 0$ , a film with thickness  $L$  is unstable as it can lower its energy by bifurcating into films of thickness  $L-1$  and  $L+1$ ; for  $\Delta\mu_L > 0$ , the film is stable against such a bifurcation.

Reprinted with permission from Han and Liu[44]. Copyright 2009 by the American Physical Society.

[45] shows a significantly different energy/area with thickness of the Ag island.

Therefore, the evidence is now clear that quantum confinement of the conduction electrons influences the growth behavior of *both* Pb(111) and Ag(111): their different growth behaviors (Pb having bilayer oscillations and Ag exhibiting only the first tri-layer) is a consequence of their different electronic structures. The Pb/Si(111)7x7 system exhibits *persistent* bilayer growth oscillations because such oscillations are clearly present in the electronic structure of Pb(111) [44]. In the case of Ag(111), however, such oscillations are entirely absent in the thickness-dependent electronic structure[44]. The minimum stable height, which is a Ag tri-layer, is due to QSE of the islands that are in coexistence with the wetting layer.

## Chapter 5

# Poisson-like island height distribution

Our experiments showed that the minimum preferred island height is a trilayer. The predominance of trilayer islands is observed at low coverage and the 3 layers can already be observed at a coverage that is barely above the wetting layer saturation coverage, as shown in Fig. 4.6. But even with average heights greater than 3 layers, we can still see the system manifesting the 3-layer minimum height from the statistics of the island height distributions in the temperature and coverage dependence studies.

## 5.1 The mean and variance from island height distributions

### 5.1.1 Normalized island height distribution

In order to study the statistics of the island height distributions, we introduce normalized island height distribution  $p'_j$ . Because the islands coexist with the wetting layer, we need to include the fraction of surface occupied by the wetting layer  $p_{wet}$  to get  $p_{wet} + \sum p_j = 1$ . We already discussed in chapter 4 that it is difficult to distinguish  $p_1$  from  $p_{wet}$  in a reflectivity measurement so we absorbed  $p_1$  into  $p_{wet}$ . The normalized island height distribution  $p'_j = \frac{p_j}{\sum_{j=2} p_j}$ , and  $\sum_{j=2} p'_j = 1$ . The normalized island height distribution  $p'_j$  (or island population) describes the fraction of the islands with height  $j$ , whereas  $p_j$  describes the fraction of the surface that has islands with height  $j$ . Now with  $p'_j$ , the mean island height  $\bar{n}$  is calculated as  $\sum j p'_j$ , and the variance  $s^2$  is calculated as  $\sum j^2 p'_j - \bar{n}^2$ .

### 5.1.2 Constant difference between the mean and the variance

After looking over the normalized island distribution from all the measurements, we discover that the mean and the variance of our data is always different by a value that is close to 3, as shown in Fig. 5.1. It is interesting that the variance being a constant difference from the mean occurs for all of the growth conditions that we have studied.

The constant difference between the mean and the variance breaks down at low temperatures. As shown in the Fig. 5.1, the variance gets closer to 0 as the temperature decreases, the decreasing trend can no longer be maintained after certain temperature point because the variance can not go below 0, so the curve must bend



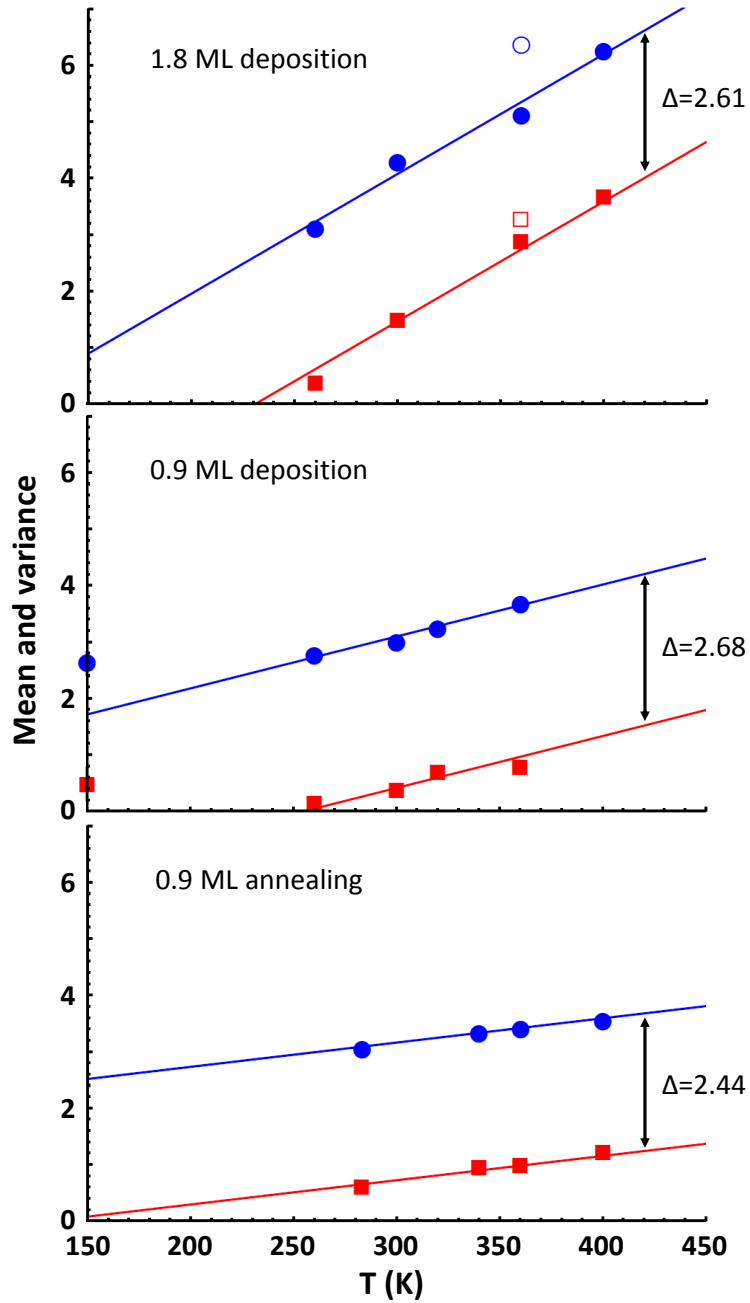


Figure 5.1: The mean (circles) and the variance (squares) calculated from island population of (a) 1.8 ML Ag deposited at different temperatures. 2.7 ML deposited at 360K is plotted in open circle and open square. (b) 0.9 ML Ag deposited at different temperatures, and (c) annealing at different temperatures for 0.9 ML Ag deposited at 150K. Same slope is used for the line going through the mean and the variance in each data set.

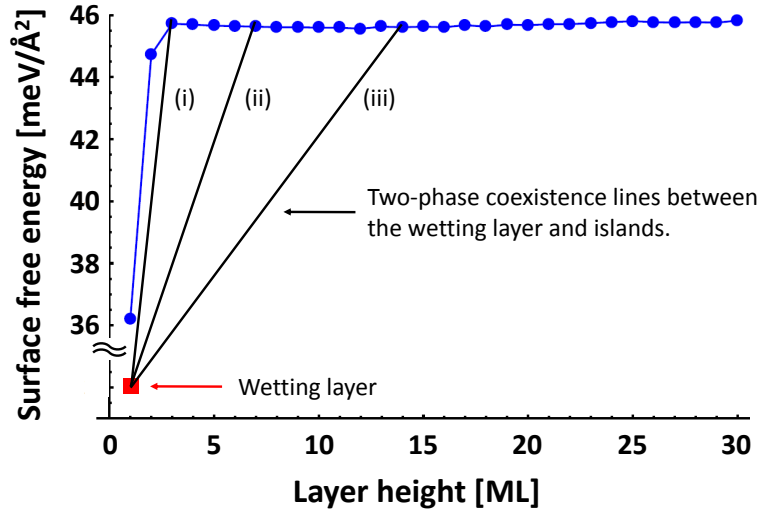


Figure 5.2: Ag(111) surface free energy versus layer height. The blue circles are replotted from thickness-dependent DFT calculations by Han and Liu[44] for free standing Ag(111). A point for the energy/area of the wetting layer is shown qualitatively. A two-phase coexistence will occur between the wetting layer and islands. At the lowest temperature, coexistence line (i) will represent the system; but faster mobility will enable taller islands, represented by the coexistence lines (ii) and (iii) that indicate the progression of the coexistence line with increasing temperature.

over. Also at low temperatures, the atoms do not have enough mobility, the Ag film has large roughness, which breaks the constant difference.

Our results reveal an increase of the mean island height with the increasing temperature, which comes from the increased mobility at higher temperature. The DFT calculations by Han and Liu show that the energy/area for free standing Ag(111) film is independent of thickness for islands higher than 3 layers[44], as replotted in Fig. 5.2. Although the DFT did not consider a wetting layer, experimentally we know that the wetting layer has a much lower energy/area than any thickness of Ag(111) film and it is indicated schematically in Fig. 5.2. The wetting layer and Ag(111) islands will coexist and, for coverage greater than the wetting layer saturation coverage, a point

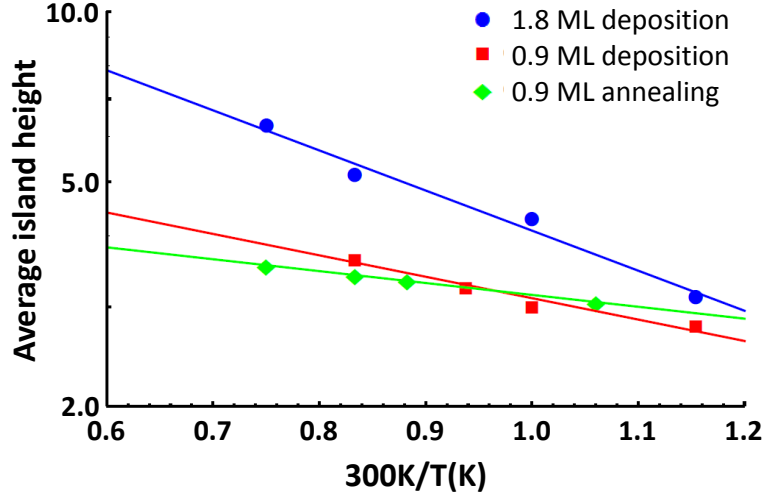


Figure 5.3: Mean island height (log scale) versus inverse temperature for different coverages and for annealing.

along a line (a coexistence line) connecting the wetting layer and a particular island height will have a lower energy than any configuration above that line. If there was unlimited mobility so that the system was truly in equilibrium, then the equilibrium state would be an infinitely tall island (of infinitesimal diameter) coexisting with the wetting layer. However, mobility plays a decisive role and at the lowest temperature we expect a coexistence line such as (i) in Fig. 5.2, which corresponds to the 3 layer minimum height observed in the experiments. As the mobility increases with increasing temperature, one expects the coexistence line to evolve to the right, as indicated by (ii) and (iii) in Fig. 5.2.

Assuming the mean island height is proportional to  $e^{-\frac{E_b}{k_B T}}$ , an energy barrier value  $E_b$  is extracted from the slope in the mean island height versus inverse temperature plot shown in Fig. 5.3. Considering all the errors propagated from fitting of the specular reflectivity and normalization of  $p'_j$ , the error bars are estimated to be at

least 5 meV. The energy barrier for deposition of 0.9 ML is determined as  $21.7 \pm 5$  meV;  $42.2 \pm 5$  meV for 1.8 ML deposition and  $12.5 \pm 5$  meV for 0.9 ML deposition.

## 5.2 Trials with simple statistic models

### 5.2.1 Shifted Poisson distribution model

We examined a number of different height distribution models in order to understand the origin of the result in Fig. 5.1. We first looked at the Poisson distribution model, for which the mean and variance are equal. If the island height follows a Poisson distribution with an average height of  $\bar{n}$ , the probability to have an island of height  $j$ , where  $j=0,1,2,\dots$ , is given by

$$P_j = \frac{\bar{n}^j e^{-\bar{n}}}{j!}. \quad (5.1)$$

$P_j$  is used here to describe the calculated distribution from models and it will be compared with the experimental data  $p'_j$ . The Poisson distribution significantly misses our data as shown in Fig. 5.4. The continuous curve in the figure is generated from replacing the discrete factorial function with the continuous Gamma function with definition  $j! = \Gamma(j + 1)$ .

The experimental island height distribution looks as if the Poisson distribution is shifted which suggests its relationship to a constant difference between the mean and variance. Fig. 5.4 shows a Poisson distribution that is shifted horizontally by  $\Delta = \bar{n} - s^2$ , given as

$$P_j = \frac{(s^2)^{j-\Delta} e^{-s^2}}{\Gamma(j - \Delta + 1)}. \quad (5.2)$$

It can be seen that the shifted Poisson distribution is able to match the right hand

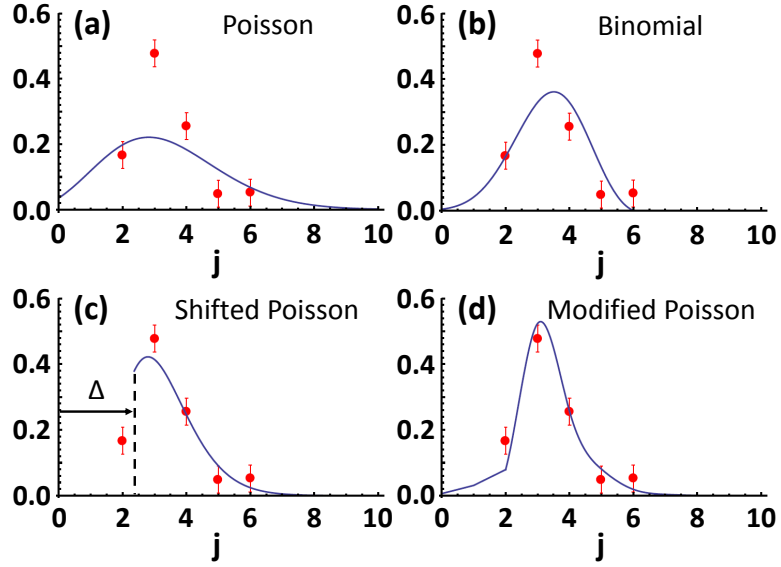


Figure 5.4: Different island height distribution models  $P_j$  (solid curve) with the data (circles) of  $\bar{n}=3.33$  and  $s^2=0.97$  from 0.9 ML Ag deposited at 150K then annealed to 340K. (a)The Poisson distribution significantly misses the data. (b)The Binomial distribution fails to reproduce the pronounced preference of 3 layer islands. (c)The shifted Poisson distribution matches only the right hand side of the data. (d)The modified Poisson distribution matches the data well. (The first three models could produce continuous curves directly using a Gamma function whereas the modified Poisson distribution model is calculated discretely and the plotted curve is an interpolation between discrete points.)

side of the data, although this procedure leaves the left hand side of the distribution undefined.

### 5.2.2 Binomial distribution model

Since a Binomial distribution model is used to describe the island height distribution from a thick film, we also want to see how well it works in the thin film case. The

Binomial distribution has two independent parameters, and is given as

$$P_j = \frac{M!}{j!(M-j)!} p^j (1-p)^{M-j}, \quad (5.3)$$

where  $M$  is an integer that gives the maximum island height and  $p$  is the probability of success. The mean value of the island height is  $\bar{n} = Mp$  and the variance is  $s^2 = Mp(1-p)$ .

The parameters  $M$  and  $p$  in the binomial distribution model can be calculated from the mean and variance of the data. Since we have a constraint that the maximum island height  $M$  must be an integer, the parameter  $M$  of the Binomial distribution model is calculated as  $M = \frac{\bar{n}}{1 - s^2/\bar{n}}$  rounded up to the nearest integer, and parameter  $p$  is calculated from the integer  $M$  as  $p = \frac{\bar{n}}{M}$ .

As shown in Fig. 5.4, a low average island height, the Binomial distribution model fits better than the Poisson distribution, it can be seen that the shape of the distribution is not correct where the width of the distribution is too broad and its height is too low. The Gamma function is used to generate a continuous curve as before.

### 5.3 Modified Poisson distribution model

The fact that a shifted Poisson distribution captures many of the features of the experimental data suggests a useful strategy for a model. We have found that a modified Poisson distribution that has unequal probabilities for the growth of different layers well describes our experimental results. We are going to explain the constant difference between the mean and the variance from the statistics embedded in the

normalized island distribution. And we are going to show that even at high coverage or high temperature where the dominant island is no longer 3-layer in height, statistics from island population still carry the information that the minimum preferred island height is 3 layers.

### 5.3.1 The derivation of the conventional Poisson distribution

We will first derive the conventional Poisson distribution before presenting the modified Poisson distribution model. The conventional Poisson distribution is obtained[46] by considering the differential probability,  $\delta p$ , that evolves with time,  $\delta t$ .  $\delta p = \lambda \delta t$ , where  $\lambda$  is the probability per time that an atomic layer forms on top of a preexisting atomic layer. Note that lambda is independent of the particular layer position. The probability of having 0 layer island (bare substrate) after deposition time  $t+dt$  is

$$P_0(t + dt) = P_0(t)(1 - \lambda dt). \quad (5.4)$$

Solving the differential equation  $\frac{dP_0(t)}{dt} = -\lambda P_0(t)$ , the probability to have bare substrate is

$$P_0(t) = e^{-\lambda t}. \quad (5.5)$$

There are two events that contribute to the change of the possibility to have 1-layer island after deposition time  $t+dt$ : adding one more layer on top of bare substrate and not adding one more layer on top of 1-layer island.

$$P_1(t + dt) = P_0(t)\lambda dt + P_1(t)(1 - \lambda dt). \quad (5.6)$$

We need to solve the differential equation  $\frac{dP_1(t)}{dt} + \lambda P_1(t) = \lambda P_0(t)$ . A general way to solve  $\frac{dy(x)}{dx} + ay(x) = f(x)$  is to let  $y(x) = g(x)e^{-ax}$ , after substitution  $\frac{dy(x)}{dx} = \frac{dg(x)}{dx}e^{-ax} - ag(x)e^{-ax}$ , we get  $\frac{dg(x)}{dx} = f(x)e^{ax}$ . So  $y(x) = e^{-ax}[g(0) + \int_0^x f(x')e^{ax'} dx']$ . The initial condition defines  $P_0(0) = 1$ , and  $P_j(0) = 0$  for  $j \geq 1$ , at the end the solution is

$$P_1(t) = e^{-\lambda t} \int_0^t \lambda P_0(t') e^{\lambda t'} dt' = \lambda t e^{-\lambda t}. \quad (5.7)$$

In general the probability to have  $j$ -layer island after deposition time  $t$  is given as

$$P_j(t) = e^{-\lambda t} \lambda \int_0^t P_{j-1}(t') e^{\lambda t'} dt'. \quad (5.8)$$

The probability to have 2-layer island is

$$P_2(t) = e^{-\lambda t} \lambda \int_0^t P_1(t') e^{\lambda t'} dt' = \frac{1}{2} (\lambda t)^2 e^{-\lambda t}. \quad (5.9)$$

Solving equation 5.8 recursively leads to

$$P_j(t) = \frac{(\lambda t)^j}{j!} e^{-\lambda t}, \quad (5.10)$$

which is the conventional Poisson distribution. The proportionality constant  $\lambda$  describes the probability to add one layer of island in certain amount of deposition time. But only the product of  $\lambda t$  may be properly defined, which is the mean and variance of the distribution,  $\lambda t = \bar{n} = s^2$ .



### 5.3.2 Poisson distribution with different layer probabilities

In the above derivation of the Poisson distribution, the probability parameter  $\lambda$  is assumed to be the same for all layer heights. In order to achieve a shifted distribution, we explore a  $\lambda_j$  that depends on layer height,  $j$ . The probability to have no island is

$$P_0(t) = e^{-\lambda_0 t}, \quad (5.11)$$

and the probability to have an island with height  $j$  is

$$P_j(t) = e^{-\lambda_j t} \lambda_{j-1} \int_0^t P_{j-1}(t') e^{\lambda_j t'} dt'. \quad (5.12)$$

In the limit of all  $\lambda_j$  equal to each other, this gives the conventional Poisson distribution.

The next three terms in the modified Poisson distribution are given as

$$\begin{aligned} P_1(t) &= \lambda_0 \frac{e^{-\lambda_0 t} - e^{-\lambda_1 t}}{\lambda_1 - \lambda_0}, \\ P_2(t) &= \lambda_1 \lambda_0 \left[ \frac{e^{-\lambda_0 t} - e^{-\lambda_2 t}}{(\lambda_1 - \lambda_0)(\lambda_2 - \lambda_0)} - \frac{e^{-\lambda_1 t} - e^{-\lambda_2 t}}{(\lambda_1 - \lambda_0)(\lambda_2 - \lambda_1)} \right], \\ P_3(t) &= \lambda_2 \lambda_1 \lambda_0 \left[ \frac{e^{-\lambda_0 t} - e^{-\lambda_3 t}}{(\lambda_1 - \lambda_0)(\lambda_2 - \lambda_0)(\lambda_3 - \lambda_0)} - \frac{e^{-\lambda_2 t} - e^{-\lambda_3 t}}{(\lambda_1 - \lambda_0)(\lambda_2 - \lambda_0)(\lambda_3 - \lambda_2)} \right. \\ &\quad \left. - \frac{e^{-\lambda_1 t} - e^{-\lambda_3 t}}{(\lambda_1 - \lambda_0)(\lambda_2 - \lambda_1)(\lambda_3 - \lambda_1)} + \frac{e^{-\lambda_2 t} - e^{-\lambda_3 t}}{(\lambda_1 - \lambda_0)(\lambda_2 - \lambda_1)(\lambda_3 - \lambda_2)} \right]. \end{aligned} \quad (5.13)$$

As can be seen from  $P_1$ ,  $P_2$  and  $P_3$ , we expect more and more terms to show up in the expression for higher island distributions. It is impractical to manually derive the analytical forms for all island distributions, some software must be used to do the work. Also there are a lot of subtraction and division between all similar terms like

$\frac{e^{-\lambda_0 t} - e^{-\lambda_1 t}}{\lambda_1 - \lambda_0}$ , the precision in the calculations is also a concern especially when  $\lambda_j$ s are close.

### 5.3.3 Calculation of modified Poisson distribution

An empirical summation form is figured out for all the probabilities in the modified Poisson distribution, and we need to do some tests to verify the summation form. One simple test is to give similar values to the  $\lambda$ s,  $\lambda_j = \lambda_0(1 + j\varepsilon)$  with  $\varepsilon \ll 1$ , and see whether we can reproduce the Poisson distribution. If we take  $\varepsilon = 0.01$  and  $\lambda_0 t = 5$ , the possibility generated in Microsoft Excel gets extremely off when it reaches  $P_{10}$ . If the value of  $\varepsilon$  is decreased in order to increase the accuracy, the precision limit blows off quicker, with  $\varepsilon = 0.001$ , the possibility starts to get extremely off as early as  $P_7$ .

We need good decimal digits precision in the calculations so that the final result are accurate enough. The precision standard is looked up online and it is found that many hardware floating point units use the IEEE Standard for Floating-Point Arithmetic (IEEE 754). Single-precision floating-point format occupies 4 bytes (32 bits) in computer memory. It has 1 bit of Sign bit, 8 bits of Exponent width and 24 bits (23 explicitly stored) of Significand precision. This gives from 6 to 9 significant decimal digits precision. Double-precision floating-point format occupies 8 bytes (64 bits) in computer memory. It has 1 bit of Sign bit, 11 bits of Exponent width and 53 bits (52 explicitly stored) of Significand precision. This gives from 15 to 17 significant decimal digits precision. Quadruple-precision floating-point format occupies 16 bytes (128 bits) in computer memory. It has 1 bit of Sign bit, 15 bits of Exponent width and 113 bits (112 explicitly stored) of Significand precision. This gives from 33 to 36 significant decimal digits precision.

C/C++ is a solid coding tool, on the x86 architecture, most C compilers implement long double as the 80-bit extended precision type. Compilers may also use long double for a 128-bit quadruple precision format. On some machines, long double is implemented as a double-double arithmetic, where a long double value is regarded as the exact sum of two double-precision values, giving at least a 106-bit precision. But in general, Long double gives less than 34 significant decimal digits precision.

Microsoft Excel is used for quick tests and plots, it works with 8-byte numbers by default which gives 15 significant figures, which means although it will display 30 decimal digits only the first 15 digits are meaningful.

Mathematica is a powerful computer software, it evaluates numerically to 50-digit precision! So in the end Mathematica is chosen to calculate the distributions in replacement of C/C++. With the 50 decimal precision in Mathematica, at  $\lambda_0 t = 5$  and  $P_n$  up to  $n=10$ , we can go up to  $\varepsilon=1/200,000$  and get a 0.01% difference (from the conventional Poisson distribution) for  $P_{10}$ .

Mathematica provides us more than the decimal digits precision. The ability to do integrals carrying  $\lambda_j$  parameters in analytical form without assigning values completely removes the need of a empirical summation form of the distribution. All the results shown in this chapter are calculated directly with integrals following equation 5.12.

For the final results, the mean and variance of the modified Poisson distribution are calculated from  $P_0$  up to  $P_{10}$ . A normalization is done to make sure  $\sum_{j=0}^{10} P_j = 1$  so that the mean and variance are calculated the same way as the normalized  $p'_j$ . The distribution  $P_j$  is discrete, so we used cubic spline interpolation to generate a curve going through the data when we plot the  $P_j$  values with our  $p'_j$  distribution. A linear

interpolation is used instead in the regions where the distribution drops to 0 quickly that the cubic spline creates some artifacts.

### 5.3.4 The effect of the $\lambda_j$ parameters

Now we explore how the  $\lambda_j$  parameters modify the Poisson distribution with a fixed mean value ( $\bar{n}=6.3$  is chosen here). The mean value of the modified Poisson distribution is calculated from  $P_j$ , different  $\lambda t$  parameter is tested until the generated distribution provides the desired mean value. Because there is a large degeneracy in choosing the  $\lambda_j$ , we examine the distribution for just two values of  $\lambda_j$ , one value for  $0 \leq j < j_{max}$  and one for all other  $j$ ,  $\lambda_j = \lambda$ . As can be seen in Fig. 5.5a for  $j_{max}=1$ , having  $\lambda_0 > \lambda$  suppresses  $P_j$  relative to the Poisson distribution for low values of  $j$ . Furthermore, Fig. 5.5 shows that increasing  $j_{max}$  increases the range at low  $j$  over which the island height distribution is suppressed, which is precisely the effect observed in the experimental data. Increasing  $j_{max}$  also decreases the variance, thereby increasing  $\Delta$ .

We never observe a strong suppression of  $p'_3$  in the data, and the average difference between the mean and variance is 2.58 from our measurements, as shown in Fig. 5.1. The model with  $\lambda_0, \lambda_1, \lambda_2 > \lambda$ , the rest  $\lambda_j = \lambda$  for  $j \geq 3$  matches the characteristics of the experimental island height distribution and gives the proper range of  $\Delta$ .

### 5.3.5 Final model for Modified Poisson distribution

Assigning  $\lambda_0 = \lambda_1 = \lambda_2$  different than  $\lambda$ , with  $\lambda_0 > \lambda_j$  for  $j \geq 3$  can be explained by having a different probability to nucleate on top of the wetting layer and the initial

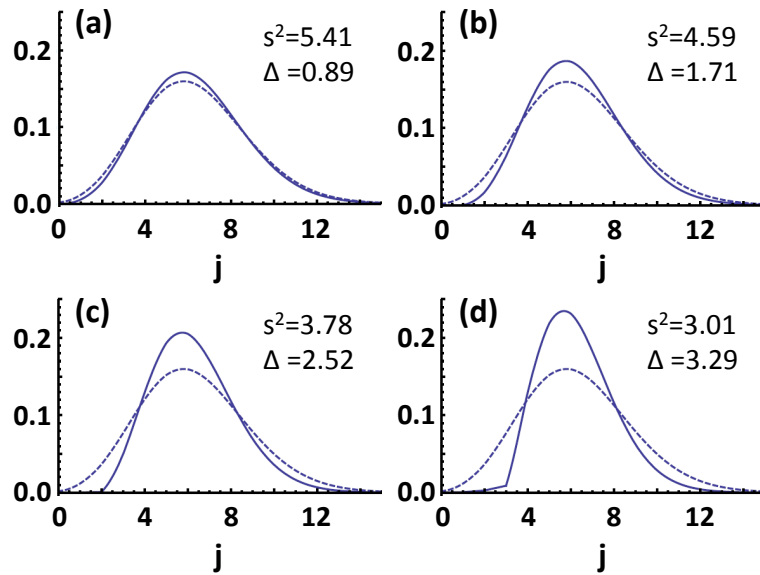


Figure 5.5: Using a mean of 6.3, the modified Poisson distribution (solid curve) is compared with the Poisson distribution (dashed curve with  $\bar{n} = s^2 = 6.3$ ). (a)  $\lambda_0 = 2.5\lambda$  and  $\lambda_j = \lambda$  for  $j \geq 1$ , (b)  $\lambda_0 = \lambda_1 = 2.5\lambda$  and  $\lambda_j = \lambda$  for  $j \geq 2$ , (c)  $\lambda_0 = \lambda_1 = \lambda_2 = 2.5\lambda$  and  $\lambda_j = \lambda$  for  $j \geq 3$ , and (d)  $\lambda_0 = \lambda_1 = \lambda_2 = \lambda_3 = 2.5\lambda$  and  $\lambda_j = \lambda$  for  $j \geq 4$ . It can be seen that the increasing the number of initial  $\lambda_j$  that are different than  $\lambda$  suppresses the initial  $P_j$  and increases the difference  $\Delta$  between the mean and the variance.

1 and 2 layer islands, then when islands grow higher the probability to nucleate on top becomes normal. Because Ag wets the whole surface first then when islands form they consume the wetting layer, the meaning of  $\lambda_0$  is related with the probability to form an island after the wetting layer saturation.

$\lambda_0 < \lambda$  was also tested, which creates a high  $P_0$ . After proper normalization  $\sum_{j=1}^{10} P_j = 1$ , we find that the distribution  $P_j$  is very off compared with  $p'_j$ . And  $P_j$  even has  $\bar{n} < s^2$  at relatively high  $\bar{n}$  around 6 ML. The only way the modified Poisson distribution works for both low and high average island height is that  $\lambda_0$ ,  $\lambda_1$ , and  $\lambda_2$  all bigger than  $\lambda$ . This higher probability to nucleate at the initial growth of the islands makes the first 3 layers of islands easier to grow, and it leads to the lowest preferred height of 3-layer islands!

In order to remove degeneracy and reduce parameters of the model,  $\lambda_0 = \lambda_1 = \lambda_2$  is used, so there are only two parameters in the final model:  $\lambda_0/\lambda$  and  $\lambda t$ .  $\lambda_0/\lambda$  and  $\lambda t$  to are tuned to match the mean and variance of our data. Fig. 5.6 shows the comparison of the best fit of the model to our data. As can be seen, the agreement is quite good. In particular, for low  $\bar{n}$  conventional Poisson or Binomial distributions will not match the data, as was demonstrated in Fig. 5.4. The parameters of the model are shown in Fig. 5.7. As can be seen,  $\lambda t$  increases with temperature. Since the mobility of atoms increases with the temperature, it makes sense that the overall probability of island growth  $\lambda t$  also increases with temperature. And the probability to grow the first 3 layers of islands is relatively high when there is not enough mobility to grow taller islands.

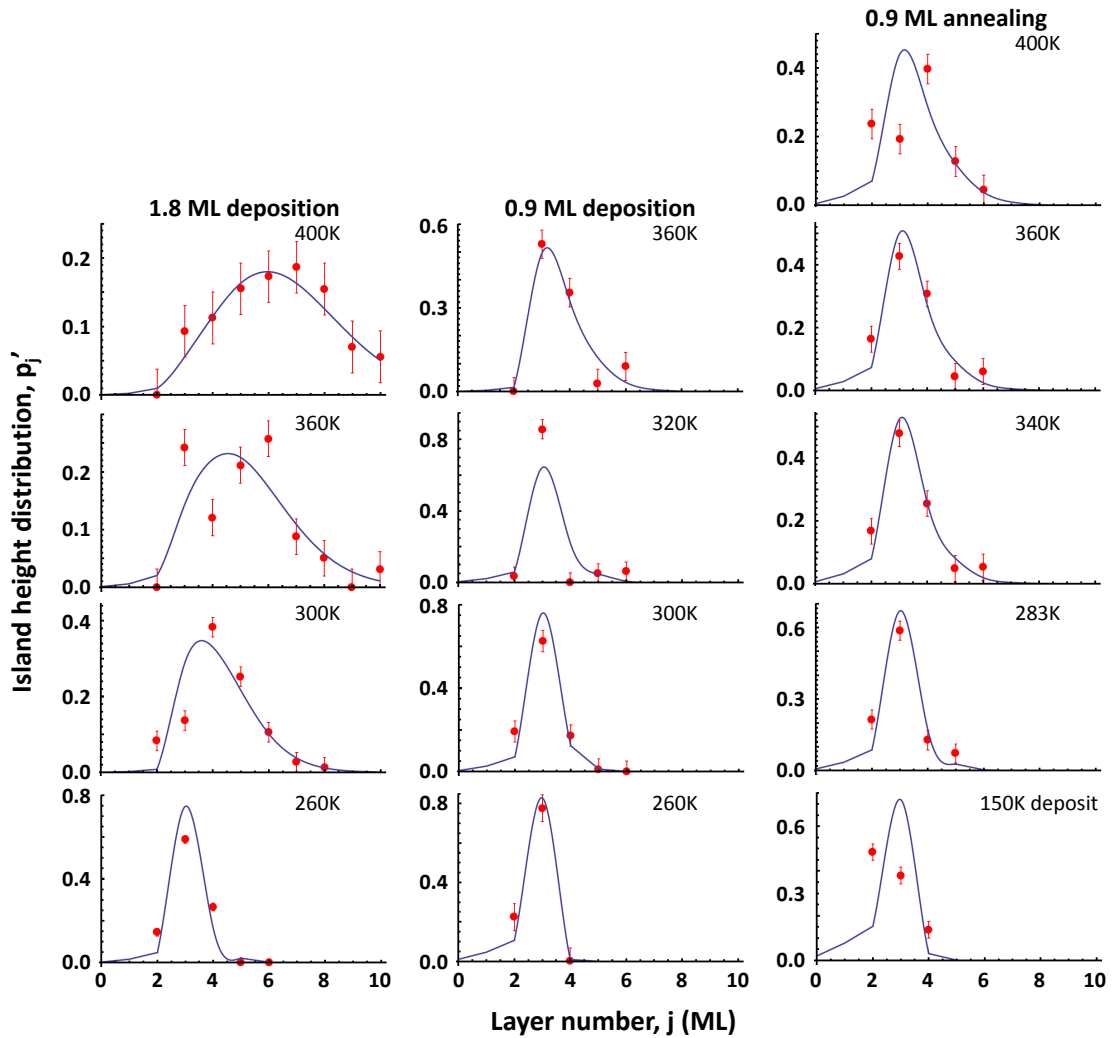


Figure 5.6: Normalized island height distribution  $p'_j$  for 1.8 ML Ag deposited at different temperatures, 0.9 ML Ag deposited at different temperatures, and 0.9 ML Ag deposited at 150K then annealed to different temperatures. A cubic spline curve from modified Poisson distribution model is plotted with the data, linear interpolation is used in the regions where cubic spline creates artifacts.

Data					Fit by matching mean and variance					
coverage	temperature	mean	variance	difference	$\lambda t$	$\lambda_0/\lambda$	mean	variance	difference	
1.8	400	6.27	3.70	2.58	5.62	1.45	6.27	3.70	2.57	
1.8	360	5.13	2.90	2.23	3.76	1.90	5.13	2.91	2.22	
1.8	300	4.29	1.51	2.79	2.01	4.2	4.29	1.50	2.79	
1.8	260	3.12	0.40	2.72	0.42	14	3.12	0.39	2.73	
2.7	360	6.39	3.30	3.08	5.13	2.0	6.39	3.28	3.11	
0.9	360	3.68	0.81	2.87	1.15	6.6	3.68	0.828	2.85	
0.9	320	3.25	0.71	2.53	0.79	6.8	3.24	0.700	2.54	
0.9	300	3.00	0.40	2.60	0.33	16	3.01	0.406	2.60	
0.9	260	2.78	0.17	2.60	0.06	80	2.77	0.389	2.38	
0.9	150	2.65	0.50	2.15	0.10	40	2.66	0.564	2.10	
Anneal 0.9	283	3.06	0.62	2.43	0.55	9.0	3.06	0.602	2.46	
Anneal 0.9	340	3.34	0.97	2.37	1.11	4.6	3.33	0.970	2.36	
Anneal 0.9	360	3.41	1.01	2.40	1.22	4.3	3.41	1.03	2.38	
Anneal 0.9	400	3.55	1.25	2.30	1.51	3.5	3.55	1.25	2.30	

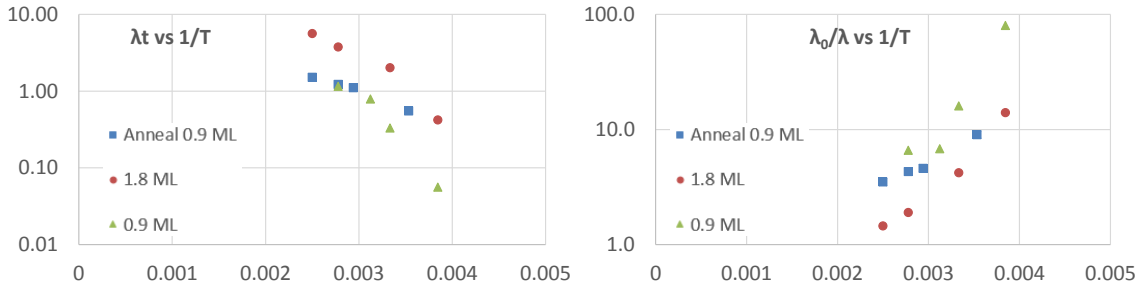


Figure 5.7: Modified Poisson distribution model parameters for the fit to our data. The Arrhenius plots for  $\lambda t$  vs  $1/T$  and  $\lambda_0/\lambda$  vs  $1/T$  show a linear relationship.



## 5.4 Conclusion

In the end, a modified Poisson distribution model is able to describe the island height distributions from our specular reflectivity measurements. A higher probability to grow the first 3 layers of Ag islands is required to reproduce the statistics of the island height distribution. The statistics embedded within the island height distribution reveals the preference of 3-layer islands as the lowest stable height even when the predominant island height is higher than 3 layers.

# Chapter 6

## Ag/Ag homoepitaxial results

In order to design and engineer the desired nanostructures, it is critical to understand the kinetic mechanisms that control the growth and evolution of nanoscale materials. Consequently, epitaxial growth has been an active field of both experimental and theoretical researches (for a recent review, see Ref#[47]). Much of the theoretical work was done by kinetic Monte Carlo (KMC) simulations, which rely on the knowledge of the basic kinetic mechanisms that are operative on the surface. A lot of parameters used in the simulations are best obtained through comparison to experiments. But in all cases, the assumed mechanisms in the simulations do not allow the incorporation of missing atoms (vacancies) in the film growth. On the experimental side, most of the investigations are carried out by scanning probe techniques which could only look at the surface, whereas x-ray measurements are sensitive to both the surface and the subsurface, as well as strains in the film. It has been shown that the mechanism of “downward funnelling” forbids vacancy formation in the simulations. However, if it is restricted, then vacancy clusters are reproduced[48].

We want to investigate the origin and the relevance of large strains that have been discovered in earlier x-ray scattering studies performed by our group[49, 50, 51]. Trying to explain the diffuse intensity measured from relatively thin films, we present our approaches to analytical and numerical calculations of the displacement field near a surface. Data analysis is also performed on the accelerated molecular dynamics simulation results to study the displacement field from the simulated surface morphology. Tests are done in the search for an efficient means of calculating diffuse scattering intensity from analytical displacement field.

## 6.1 Background

While studying the homoepitaxial growth of Cu(001), Ag(001), and Ag(111) at low temperatures ( $\sim 100$  K), our group observed a pronounced asymmetry and interference fringes around the Bragg peaks in the reflectivity measurements, as shown in Fig. 6.1. The periodicity of the interference fringes corresponds to the film thickness, and the asymmetry and the fringes were explained by a surface normal compressive strain distributed uniformly through the deposited film. This compressive strain  $\frac{\Delta d}{d} = \frac{d_{film} - d_{bulk}}{d_{bulk}}$  is about -1% in the films grown on all three systems[49, 50, 51].

Since a negative volume change is necessary to produce the observed contraction of lattice constant, our group attribute the origin of the substantial compressive strain to a large number of vacancies incorporated in the growing film. The vacancy concentration was originally estimated to be  $\sim 2\%$  based on the magnitude of the strain[50] assuming a point defect model and assuming mono-vacancies, although subsequent diffuse x-ray scattering studies[52, 53] showed that the strains were gen-

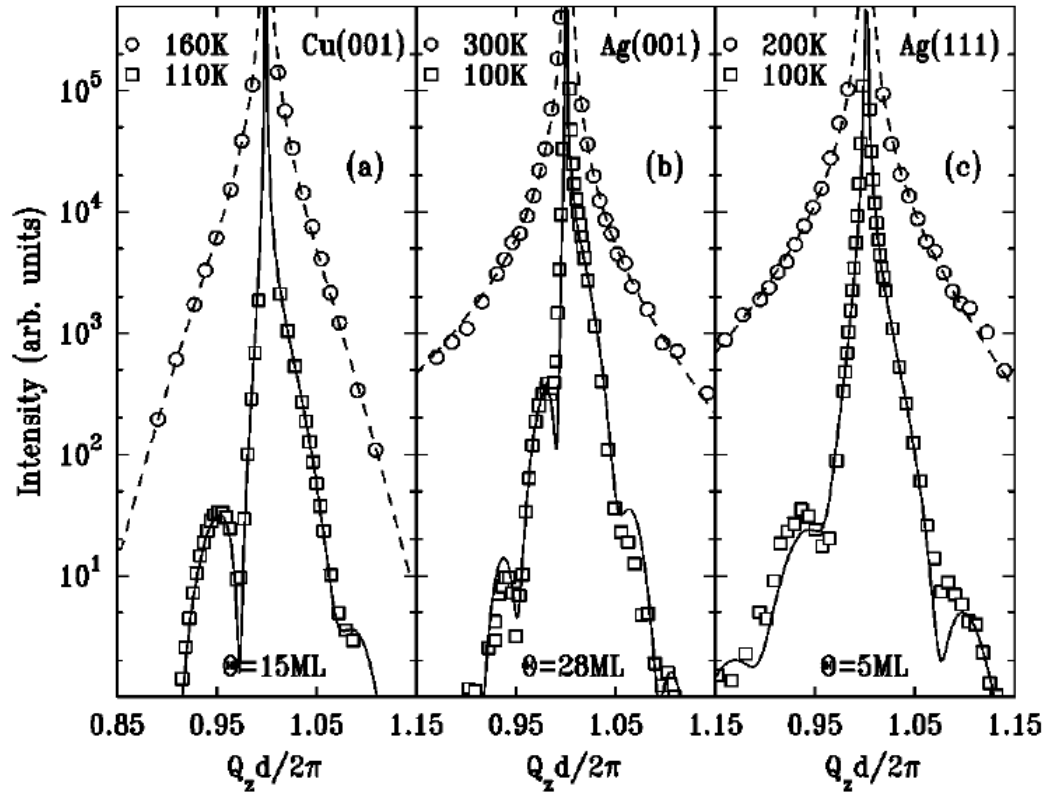


Figure 6.1: Specular x-ray reflectivity from (a) Cu/Cu(001), (b) Ag/Ag(001), and (c) Ag/Ag(111) films. Compared with higher temperatures, the lower temperature reflectivity profiles exhibit interference fringes and an asymmetry about the Bragg reflection. A large surface-normal compressive strain in the deposited film is necessary to fit the data. Reprinted with permission from Botez et al.[50]. Copyright 2007, AIP Publishing LLC.

erated by a much smaller concentration of large clusters. The 100K-deposited sample was annealed to a higher temperature known for vacancy annealing, and the vacancy concentration indeed disappeared.

Our group performed x-ray diffuse scattering measurements on 100 ML Ag(001) homoepitaxial films, and revealed unexpectedly large local volume dilatation of  $750 \text{ \AA}^3$  and small concentration 0.05% for the average vacancy clusters[52, 53], which leads to the vacancy concentration being much less than our previous estimation of 2% for mono-vacancies[50].

An alternative explanation was suggested by Amar et al.[54]. Their accelerated molecular dynamics (MD) and temperature-accelerated dynamics (TAD) simulation results suggest that the nanoscale surface roughness caused by large off-normal deposition angles would lead to compressive strain comparable in size to that observed in our x-ray measurements, because the reflectivity calculated from their simulation results was able to match our experimental data. The simulation results are shown in Fig. 6.2.

An important aspect of the claim by Shim et al. that the surface roughness is the origin of the experimentally observed strain relies on having a grazing angle of deposition. They see significant effects for 60 degree deposition (relative to normal) but the x-ray experiments were performed for a much smaller angle of 30 degrees. Therefore, it is likely that the surface roughness effect is not entirely responsible for the observed strain. Although the research to this point is somewhat incomplete, the goal of the following section is to begin analyzing how to distinguish strain due to vacancy clusters from strain arising from nano-surface roughness.

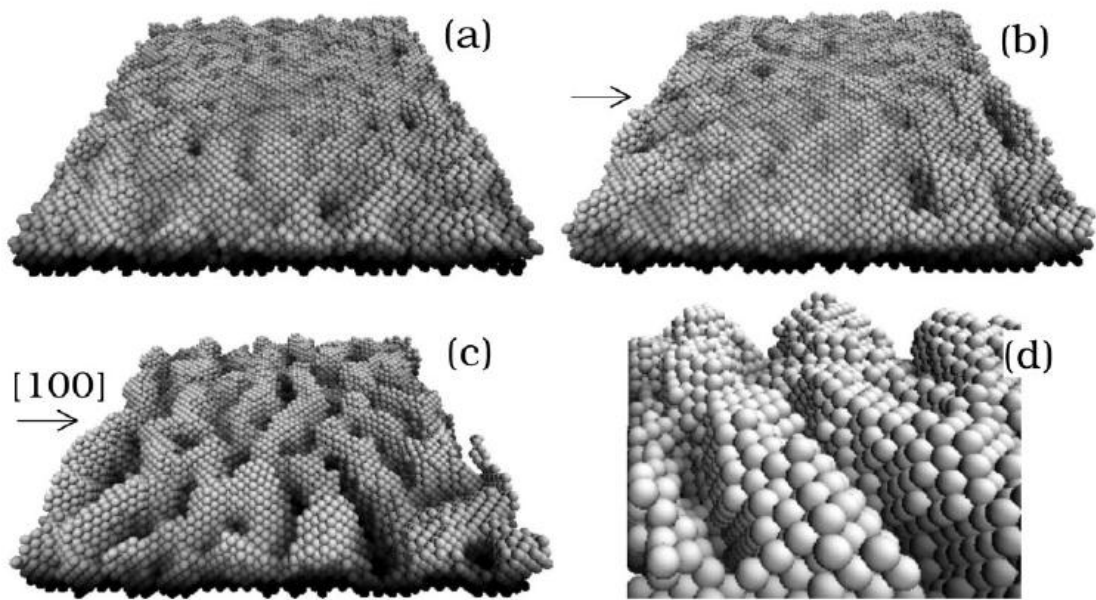


Figure 6.2: Surface morphology for 7 ML Cu/Cu(100) films simulated at  $T=40$  K with TAD for case of (a) normal incidence (b) deposition angle  $\theta = 30^\circ$  and (c)  $\theta = 60^\circ$ . (d) shows blow-up of portion of (c). Arrows in (b) and (c) indicate azimuthal orientation of deposition. Reprinted with permission from Shim et al.[54]. Copyright 2008 by the American Physical Society.

## 6.2 Ag/Ag diffuse scattering

X-ray diffuse scattering directly measures the local displacement field from the defects[55], thus it is an ideal tool to obtain information about vacancy cluster size and provide conclusive evidence of vacancy incorporation. It is important to recognize the crucial difference between reflectivity and diffuse measurements: Bragg peaks come from the *average* long-range order of the atomic positions in the crystal structure in the crystal structure whereas the diffuse scattering arises from the short-range disorder, which in this case is due to the *local* elastic distortion (displacement of the atoms away from the bulk position) around the vacancy cluster.

Because the vacancy cluster size is unexpectedly large (about 40 missing atoms), the resulting large displacement field violates assumptions used in the diffuse scattering theories[53]. All the analytical equations to calculate diffuse scattering employed small displacement approximation, which assumed  $\vec{Q} \cdot \vec{t}(\vec{r}) \ll 1$ , where  $\vec{Q}$  is the momentum transfer and  $\vec{t}(\vec{r})$  is the elastic displacement at a distance  $r$  from a point defect. In our case, since the vacancy clusters are really large, the displacement field  $\vec{t}(\vec{r})$  is also large, we could not apply the small displacement approximation. A new method needs to be developed, and this has not been done by anyone until Kim came up with a numerical way to calculate the intensities shown in Fig. 6.3.

When Kim et al.[52, 53] performed the calculations on 100 ML homoepitaxial films, it was unnecessary to use a thin film model because of the large film thickness. He took the equations for bulk materials from Dederichs[55] and Krivoglaz[56] where no assumption is made about the size of the displacement field, and performed

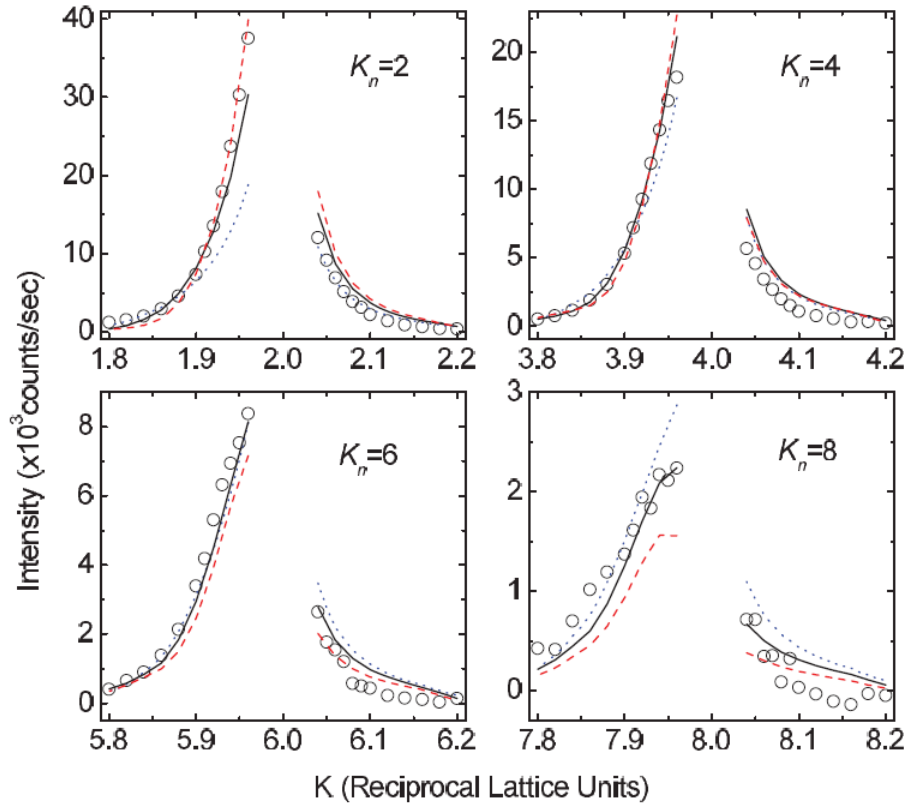


Figure 6.3: Comparison of the measured diffuse scattering intensity (circles) and the numerically calculated intensities (lines) of 100 ML Ag(001) homoepitaxial films. Dotted (blue), solid (black), and dashed (red) lines are for vacancy strength  $-b = 30$ , 60, and 100, respectively. Reprinted with permission from Kim et al.[53]. Copyright 2012 by the American Physical Society.



numerical calculations from here.

$$\begin{aligned}
I(\vec{Q})_{Diff} &= N e^{-2M} |f|^2 \int \frac{d\vec{R}}{V_c} e^{i\vec{q}\cdot\vec{R}} [e^{\phi(\vec{R})-\phi(\infty)} - 1], \\
\phi(\vec{R}) &\equiv c \int \frac{d\vec{r}}{V_c} \{e^{i\vec{Q}\cdot[\vec{t}(\vec{R}+\vec{r})-\vec{t}(\vec{r})]} - 1 - i\vec{Q}\cdot[\vec{t}(\vec{R}+\vec{r})-\vec{t}(\vec{r})]\}, \\
\phi(\infty) &\equiv -2M \equiv -2c \int \frac{d\vec{r}}{V_c} \{1 - \cos[\vec{Q}\cdot\vec{t}(\vec{r})]\}, \\
\vec{q} &\equiv \vec{Q} - \vec{Q}_n, \quad \vec{t}(\vec{r}) = b \frac{\vec{r}}{r^3},
\end{aligned} \tag{6.1}$$

where N is the number of atoms,  $e^{-2M}$  is the static Debye-Waller factor, f is the atomic form factor,  $V_c$  is the volume per atom, c is the concentration of the defects,  $\vec{t}(\vec{r})$  is the elastic displacement field assuming a spherical point defect, and b gives the strength and sign (negative for vacancies, positive for interstitials) of the defect. Without making any approximations, we need to do all the integrations numerically.

### 6.3 Ag/Ag coverage-dependent diffuse scattering data

If the vacancy cluster size is large, then we should see a change in the diffuse intensities when the film becomes thin, on the order of the vacancy cluster size. We performed diffuse scattering measurements on the in-situ scattering facility located at 6IDC at the Advanced Photon Source for thin Ag(001) homoepitaxial films having thickness of 5, 10, and 20 ML, along (0, K, 0.1) at four different Bragg peak locations K=2, 4, 6, and 8. As shown in Fig. 6.4, the 100 ML film shows a higher intensity on the low Q side of the Bragg position, which is a signature of vacancy clusters. The 100 ML thickness is larger than the estimated vacancy cluster size. However, it can be seen

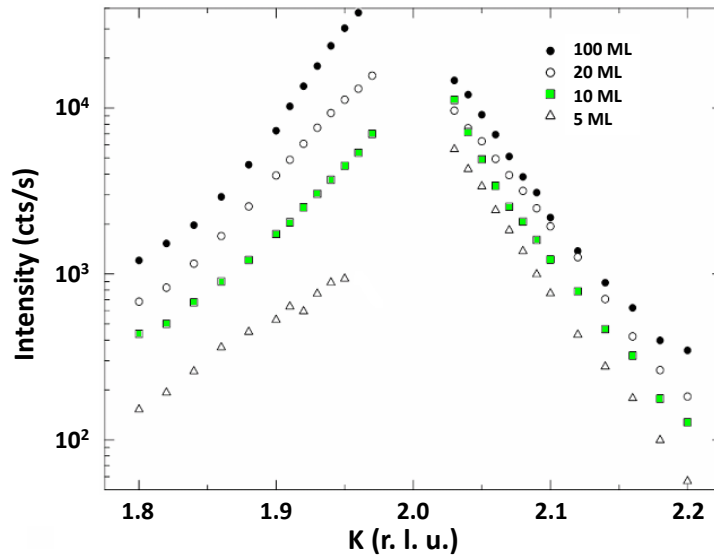


Figure 6.4: X-ray diffuse scattering measurements for Ag/Ag(001) obtained along  $(0, K, 0.1)$ , at coverages of 5 ML, 10 ML, 20 ML, and 100 ML. The asymmetry between the low K and high K side is switched from the coverage of 20 ML to 10 ML.

that the asymmetry progressively switches to the other side of the Bragg position as the film thickness decreases to a value that is smaller than the vacancy cluster size estimated in the previous diffuse scattering study. Therefore, the origin of this switch in asymmetry is an important question that we seek to explain.

In the thick film case where 100 ML is deposited, the film could be treated as bulk material, but now for our thin film data with coverage of 5 ML, 10 ML, and 20 ML, the thin film interface effect has to be taken into account. There are two separate effects that must be considered: elastic boundary conditions and issues related to scattering theory from thin films – both topics will be addressed below.

### 6.3.1 Elastic boundary conditions at the stress free surface

In an infinite isotropic elastic medium with a surface imagined at  $z=0$  (+ $z$  direction is downward), the displacement field at  $\vec{r}$  from a spherical point defect with strength  $b$  located at  $(0, 0, d)$  is given as[57]

$$\vec{u}_\infty(\vec{r}) = \frac{br_-^2}{r_-^3} = b \frac{x\hat{x} + y\hat{y} + (z-d)\hat{z}}{[x^2 + y^2 + (z-d)^2]^{1.5}}, \quad (6.2)$$

where  $b$  is the strength of the defect, and  $r_- = \sqrt{x^2 + y^2 + (z-d)^2}$ .

The strain tensor can be calculated as

$$\begin{aligned} u_{xx} &= \frac{\partial u_x}{\partial x} = \frac{b}{r_-^3} \left(1 - \frac{3x^2}{r_-^2}\right), \\ u_{yy} &= \frac{\partial u_y}{\partial y} = \frac{b}{r_-^3} \left(1 - \frac{3y^2}{r_-^2}\right), \\ u_{zz} &= \frac{\partial u_z}{\partial z} = \frac{b}{r_-^3} \left[1 - \frac{3(z-d)^2}{r_-^2}\right], \\ u_{xy} &= \frac{1}{2} \left(\frac{\partial u_x}{\partial y} + \frac{\partial u_y}{\partial x}\right) = -\frac{3bxy}{r_-^5}, \\ u_{xz} &= \frac{1}{2} \left(\frac{\partial u_x}{\partial z} + \frac{\partial u_z}{\partial x}\right) = -\frac{3bx(z-d)}{r_-^5}, \\ u_{yz} &= \frac{1}{2} \left(\frac{\partial u_y}{\partial z} + \frac{\partial u_z}{\partial y}\right) = -\frac{3by(z-d)}{r_-^5}. \end{aligned} \quad (6.3)$$

Assuming the deformation is homogeneous, the stress tensor can be calculated from the strain tensor from Landau and Liftshitz[58] equation 5.13 as

$$\begin{aligned} \sigma_{xz} &= \frac{E}{1-\sigma} u_{xz}, \\ \sigma_{yz} &= \frac{E}{1-\sigma} u_{yz}, \\ \sigma_{zz} &= \frac{E}{(1+\sigma)(1-2\sigma)} [(1-\sigma)u_{zz} + \sigma(u_{xx} + u_{yy})], \end{aligned} \quad (6.4)$$

where  $E$  is Young's modulus, and  $\sigma$  is the Poisson's ratio. The stress components at the surface  $z=0$  could be calculated as

$$\begin{aligned}\sigma_{xz} &= \frac{3E}{1-\sigma} \frac{bx d}{r_0^5}, \\ \sigma_{yz} &= \frac{3E}{1-\sigma} \frac{by d}{r_0^5}, \\ \sigma_{zz} &= \frac{E}{1-2\sigma} \frac{b}{r_0^3} - \frac{E}{(1+\sigma)(1-2\sigma)} \frac{3b}{r_0^5} [(1-\sigma)d^2 + \sigma(x^2 + y^2)],\end{aligned}\tag{6.5}$$

with  $r_0 = \sqrt{x^2 + y^2 + d^2}$ .

To make a real surface at  $z=0$ , we need to apply an elastic boundary condition at the surface such that all stress components equal zero. We need to apply a force  $(-\sigma_{xz}, -\sigma_{yz}, -\sigma_{zz})$  at every point over the whole  $x$ - $y$  plane at  $z=0$  in order to achieve a stress free surface.

The displacement field inside the film from a *point* force  $(F_x, F_y, F_z)$  (the force is applied to an area so small that it can be regarded as a point) acting on the surface at the origin  $(0, 0, 0)$  is given by Landau and Lifshitz[58] equation 8.18 as

$$\begin{aligned}u_x &= \frac{1+\sigma}{2\pi E} \left\{ \left[ \frac{xz}{r^3} - \frac{(1-2\sigma)x}{r(r+z)} \right] F_z + \frac{2(1-\sigma)r+z}{r(r+z)} F_x + \frac{[2r(\sigma r+z) + z^2]x}{r^3(r+z)^2} (xF_x + yF_y) \right\}, \\ u_y &= \frac{1+\sigma}{2\pi E} \left\{ \left[ \frac{yz}{r^3} - \frac{(1-2\sigma)y}{r(r+z)} \right] F_z + \frac{2(1-\sigma)r+z}{r(r+z)} F_y + \frac{[2r(\sigma r+z) + z^2]y}{r^3(r+z)^2} (xF_x + yF_y) \right\}, \\ u_z &= \frac{1+\sigma}{2\pi E} \left\{ \left[ \frac{2(1-\sigma)}{r} + \frac{z^2}{r^3} \right] F_z + \left[ \frac{1-2\sigma}{r(r+z)} + \frac{z}{r^3} \right] (xF_x + yF_y) \right\},\end{aligned}\tag{6.6}$$

with  $r = \sqrt{x^2 + y^2 + z^2}$ .

Landau and Lifshitz gives solution of displacement field  $u_i = G_{ik}(x, y, z)F_k$  if a surface force (stress)  $\vec{P} = \vec{F}\delta(x)\delta(y)$  is applied. The  $G_{ik}$  components can be deter-

mined once all the terms are matched to equation 6.6. For a force distribution  $P(x,y)$ , the displacement field needs to be integrated over the whole surface,

$$u_i = \iint G_{ik}(x - x_0, y - y_0, z) P_k(x_0, y_0) dx_0 dy_0. \quad (6.7)$$

For  $\vec{P}(x_0, y_0)$  acting at  $(x_0, y_0, 0)$ , the  $G_{ik}(x - x_0, y - y_0, z)$  components are

$$\begin{aligned} G_{xx} &= \frac{1 + \sigma}{2\pi E} \left[ \frac{2(1 - \sigma)r + z}{r(r + z)} + \frac{2r(\sigma r + z) + z^2}{r^3(r + z)^2} (x - x_0)^2 \right], \\ G_{xy} &= \frac{1 + \sigma}{2\pi E} \frac{2r(\sigma r + z) + z^2}{r^3(r + z)^2} (x - x_0)(y - y_0), \\ G_{xz} &= \frac{1 + \sigma}{2\pi E} \left[ \frac{(x - x_0)z}{r^3} - \frac{(1 - 2\sigma)(x - x_0)}{r(r + z)} \right], \\ G_{yx} &= \frac{1 + \sigma}{2\pi E} \frac{2r(\sigma r + z) + z^2}{r^3(r + z)^2} (x - x_0)(y - y_0), \\ G_{yy} &= \frac{1 + \sigma}{2\pi E} \left[ \frac{2(1 - \sigma)r + z}{r(r + z)} + \frac{2r(\sigma r + z) + z^2}{r^3(r + z)^2} (y - y_0)^2 \right], \\ G_{yz} &= \frac{1 + \sigma}{2\pi E} \left[ \frac{(y - y_0)z}{r^3} - \frac{(1 - 2\sigma)(y - y_0)}{r(r + z)} \right], \\ G_{zx} &= \frac{1 + \sigma}{2\pi E} \left[ \frac{(x - x_0)z}{r^3} + \frac{(1 - 2\sigma)(x - x_0)}{r(r + z)} \right], \\ G_{zy} &= \frac{1 + \sigma}{2\pi E} \left[ \frac{(y - y_0)z}{r^3} + \frac{(1 - 2\sigma)(y - y_0)}{r(r + z)} \right], \\ G_{zz} &= \frac{1 + \sigma}{2\pi E} \left[ \frac{2(1 - \sigma)}{r} + \frac{z^2}{r^3} \right], \end{aligned} \quad (6.8)$$

with  $r$  now being defined as  $r = \sqrt{(x - x_0)^2 + (y - y_0)^2 + z^2}$ . Notice that  $G_{xy} = G_{yx}$ , while  $G_{xz} \neq G_{zx}$ , and  $G_{yz} \neq G_{zy}$ .

In order to simplify the calculations, an image defect could be added to cancel out some components of the force distribution. Depending on the sign of the strength of the image defect, 2 choices could be made. Option 1 is to add an im-

age defect with strength  $-b$  at location  $(0, 0, -d)$  to make  $\vec{u}_\infty(\vec{r}) = b\frac{\vec{r}_-}{r_-^3} - b\frac{\vec{r}_+}{r_+^3}$ , with  $r_\pm = \sqrt{x^2 + y^2 + (z \pm d)^2}$ . The force needed at  $(x_0, y_0, 0)$  to cancel out the stress components from this displacement field becomes

$$\begin{aligned} -P_x = \sigma_{xz} &= \frac{6E}{1-\sigma} \frac{bx_0d}{r_0^5}, \\ -P_y = \sigma_{yz} &= \frac{6E}{1-\sigma} \frac{by_0d}{r_0^5}, \\ -P_z = \sigma_{zz} &= 0, \end{aligned} \tag{6.9}$$

with  $r_0 = \sqrt{x_0^2 + y_0^2 + d^2}$  now. The extra displacement field required to create a stress free surface is given as

$$\begin{aligned} u_x &= \iint (G_{xx}P_x + G_{xy}P_y)dx_0dy_0, \\ u_y &= \iint (G_{yx}P_x + G_{yy}P_y)dx_0dy_0, \\ u_z &= \iint (G_{zx}P_x + G_{zy}P_y)dx_0dy_0. \end{aligned} \tag{6.10}$$

$u_x$  has 3 terms,  $u_y$  has 3 terms, and  $u_z$  has 4 terms.

Option 2 is to add an image defect with strength  $b$  at location  $(0, 0, -d)$  to make  $\vec{u}_\infty(\vec{r}) = b\frac{\vec{r}_-}{r_-^3} + b\frac{\vec{r}_+}{r_+^3}$ , with  $r_\pm = \sqrt{x^2 + y^2 + (z \pm d)^2}$ . The force needed at  $(x_0, y_0, 0)$  to cancel out the stress components from this displacement field becomes

$$\begin{aligned} -P_x = \sigma_{xz} &= 0, \\ -P_y = \sigma_{yz} &= 0, \\ -P_z = \sigma_{zz} &= \frac{E}{1-2\sigma} \frac{2b}{r_0^3} - \frac{E}{(1+\sigma)(1-2\sigma)} \frac{6b}{r_0^5} [(1-\sigma)d^2 + \sigma(x_0^2 + y_0^2)], \end{aligned} \tag{6.11}$$

with  $r_0 = \sqrt{x_0^2 + y_0^2 + d^2}$  now. The extra displacement field required to create a stress

free surface is given as

$$\begin{aligned}
u_x &= \iint G_{xz} P_z dx_0 dy_0, \\
u_y &= \iint G_{yz} P_z dx_0 dy_0, \\
u_z &= \iint G_{zz} P_z dx_0 dy_0.
\end{aligned} \tag{6.12}$$

$u_x$  has 6 terms,  $u_y$  has 6 terms, and  $u_z$  has 6 terms. Comparing the complexity of  $\vec{u}$ , it is more convenient for us to choose option 1 and go with an image defect with strength -b.

Now that the total displacement field satisfying the stress free boundary condition due to a single defect with strength b at (0, 0, d) is

$$\vec{u}_{total}(x, y, z, d) = b \frac{r_-^{\vec{r}}}{r_-^3} - b \frac{r_+^{\vec{r}}}{r_+^3} + u_x \hat{x} + u_y \hat{y} + u_z \hat{z}, \tag{6.13}$$

with  $r_{\pm} = \sqrt{x^2 + y^2 + (z \pm d)^2}$ . The x, y, and z component of the total displacement field are given as

$$\begin{aligned}
u_{total,x} &= \frac{bx}{[x^2 + y^2 + (z - d)^2]^{\frac{3}{2}}} - \frac{bx}{[x^2 + y^2 + (z + d)^2]^{\frac{3}{2}}} \\
&\quad - \frac{3bd}{\pi} \frac{1 + \sigma}{1 - \sigma} \iint \left\{ \frac{x_0}{r_0^5} \left[ \frac{2(1 - \sigma)r + z}{r(r + z)} + \frac{2r(\sigma r + z) + z^2}{r^3(r + z)^2} (x - x_0)^2 \right] \right. \\
&\quad \left. + \frac{y_0}{r_0^5} \frac{2r(\sigma r + z) + z^2}{r^3(r + z)^2} (x - x_0)(y - y_0) \right\} dx_0 dy_0,
\end{aligned} \tag{6.14}$$

$$\begin{aligned}
u_{total,y} = & \frac{by}{[x^2 + y^2 + (z - d)^2]^{\frac{3}{2}}} - \frac{by}{[x^2 + y^2 + (z + d)^2]^{\frac{3}{2}}} \\
& - \frac{3bd}{\pi} \frac{1 + \sigma}{1 - \sigma} \iint \left\{ \frac{x_0}{r_0^5} \frac{2r(\sigma r + z) + z^2}{r^3(r + z)^2} (x - x_0)(y - y_0) \right. \\
& \left. + \frac{y_0}{r_0^5} \left[ \frac{2(1 - \sigma)r + z}{r(r + z)} + \frac{2r(\sigma r + z) + z^2}{r^3(r + z)^2} (y - y_0)^2 \right] \right\} dx_0 dy_0, \tag{6.15}
\end{aligned}$$

$$\begin{aligned}
u_{total,z} = & \frac{b(z - d)}{[x^2 + y^2 + (z - d)^2]^{\frac{3}{2}}} - \frac{b(z + d)}{[x^2 + y^2 + (z + d)^2]^{\frac{3}{2}}} \\
& - \frac{3bd}{\pi} \frac{1 + \sigma}{1 - \sigma} \iint \left\{ \frac{x_0}{r_0^5} \left[ \frac{(x - x_0)z}{r^3} + \frac{(1 - 2\sigma)(x - x_0)}{r(r + z)} \right] \right. \\
& \left. + \frac{y_0}{r_0^5} \left[ \frac{(y - y_0)z}{r^3} + \frac{(1 - 2\sigma)(y - y_0)}{r(r + z)} \right] \right\} dx_0 dy_0, \tag{6.16}
\end{aligned}$$

$r = \sqrt{(x - x_0)^2 + (y - y_0)^2 + z^2}$  and  $r_0 = \sqrt{x_0^2 + y_0^2 + d^2}$  are both functions of  $x_0$  and  $y_0$ .

The next step is to calculate the dot product between the momentum transfer  $\vec{Q}$  and the displacement field  $\vec{u}_{total}$ . If we take  $Q_z \approx 0$  and  $Q_x = 0$ ,  $\vec{Q} = K\hat{y}$ , we only keep the y component for  $\vec{u}_{total}$ . In equation 6.15 we can normalize all the x, y, z,  $x_0$ ,  $y_0$ ,  $r_0$  and r by d to make the coordinates dimensionless. Separating  $\vec{Q} \cdot \vec{u}_{total}$  into 3



terms,

$$\begin{aligned}
\vec{Q} \cdot \vec{u}_{total} &= Term1 + Term2 + Term3, \\
Term1 &= \frac{Kb}{d^2} \frac{y}{[x^2 + y^2 + (z - 1)^2]^{\frac{3}{2}}}, \\
Term2 &= -\frac{Kb}{d^2} \frac{y}{[x^2 + y^2 + (z + 1)^2]^{\frac{3}{2}}}, \\
Term3 &= -\frac{3Kb}{\pi d^2} \frac{1 + \sigma}{1 - \sigma} \iint \left\{ \frac{x_0}{r_0^5} \frac{2r(\sigma r + z) + z^2}{r^3(r + z)^2} (x - x_0)(y - y_0) \right. \\
&\quad \left. + \frac{y_0}{r_0^5} \left[ \frac{2(1 - \sigma)r + z}{r(r + z)} + \frac{2r(\sigma r + z) + z^2}{r^3(r + z)^2} (y - y_0)^2 \right] \right\} dx_0 dy_0,
\end{aligned} \tag{6.17}$$

where  $\vec{Q} \cdot \vec{u}_{total}$  has the order of  $\frac{Kb}{d^2}$ , which agrees with the expectation.

Term 1 and 2 can be directly calculated, Term 3 needs to be integrated. We plot the Integrand in Term 3 in 3D at different  $x, y, z$  values, as shown in Fig. 6.5. The horizontal axes are  $x_0$  and  $y_0$  in units of  $d$ , the vertical axis is the value of the Integrand  $\left\{ \frac{x_0}{r_0^5} \frac{2r(\sigma r + z) + z^2}{r^3(r + z)^2} (x - x_0)(y - y_0) + \frac{y_0}{r_0^5} \left[ \frac{2(1 - \sigma)r + z}{r(r + z)} + \frac{2r(\sigma r + z) + z^2}{r^3(r + z)^2} (y - y_0)^2 \right] \right\}$ , which is in units of  $1/d^5$ . It can be seen that Integrand=0 everywhere except near  $x_0, y_0 = 0$ , and some singularity appears near  $x_0 = x$ , and  $y_0 = y$ . We only need to do integrals in these regions to get Term 3. Looking at the vertical scales in Fig. 6.5, after integration the result may still be very small.

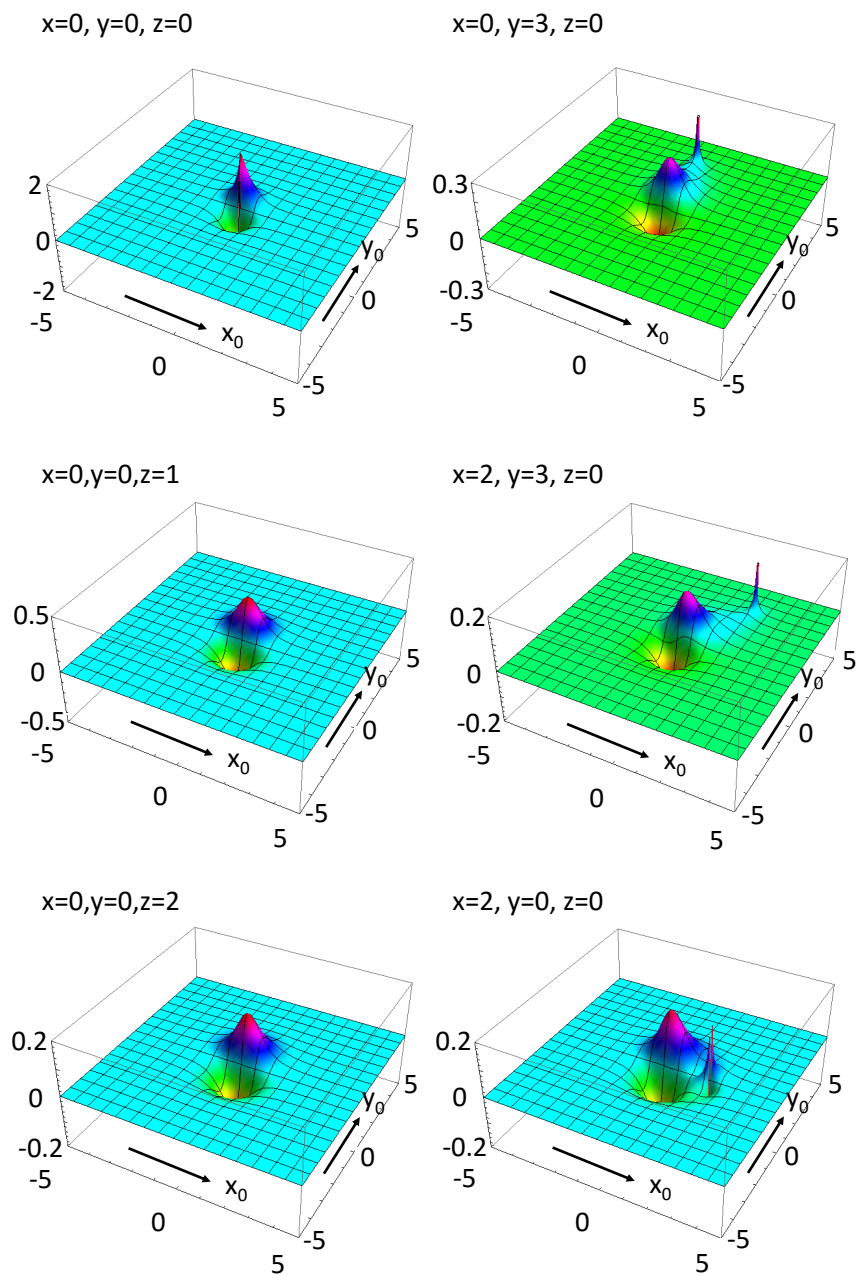


Figure 6.5: The Integrand in Term 3 of equation 6.17 plotted in 3D at different  $x$ ,  $y$ ,  $z$  values. The horizontal axes are  $x_0$  and  $y_0$ , the vertical axis is the value of the Integrand. All the coordinates  $x$ ,  $y$ ,  $z$ ,  $x_0$  and  $y_0$  are in units of  $d$ , the vertical axis is in units of  $1/d^5$ . Notice that the upper and lower limit of the vertical axis is not the same for all cases.

### 6.3.2 Thin film scattering effect

The second surface effect comes from the scattering process itself, similar to crystal truncation rods, for thin films<sup>1</sup>,

$$I_{diff}(\vec{Q}) = N |f|^2 \sum_{z,z'} e^{iQ_z(z-z')} \sum_{\vec{\rho}'_i} e^{i\vec{Q}\cdot\vec{\rho}'_i} \exp\left\{ \sum_{z_0} c(z_0) \int \frac{d^2\rho'}{\Omega_A} [e^{i\vec{Q}\cdot(\vec{t}_{z_0}(\vec{\rho}'_i+\vec{\rho}',z)-\vec{t}_{z_0}(\vec{\rho}',z'))}-1] \right\}, \quad (6.18)$$

where N is the number of atoms, f is the atomic form factor,  $\vec{\rho}'$  and  $\vec{\rho}''$  are in-plane Bravais lattice vectors,  $c(z)$  is the vacancy concentration that varies along the surface normal direction.  $\Omega_A$  is the in-plane area per atom, and  $z_0, z, z'$  describe the position of atomic planes along the surface normal direction.

### 6.3.3 Numerical integration

When Kim performed the numerical calculation for 100 ML film[52, 53], as we can see from equation 6.1, integration over space is done to calculate  $\phi(\vec{R})$ , then  $\phi(\vec{R})$  is integrated again to calculate diffuse intensity. Considering x, y, z directions in the space, a 6-dimension integral is needed for the numerical calculation! Kim found some tricks from the isotropy of the coordinate system and reduced the integration to 5 dimensions by using a polar coordinate for an integration over space. The final calculation took a whole month when it was run on a cluster of 32 computers with 400 MHz CPU.

Now if we consider the elastic boundary effect for the displacement field by using equation 6.17, we already need to do an integration over space to get  $\vec{Q}\cdot\vec{u}_{total}$ . Then as in the bulk case, we still need to do two rounds of integration over space to get the

---

<sup>1</sup>From Paul's notes

diffuse intensity. This time because of the anisotropy in the  $z$  direction, we could not reduce the dimension of integration any more, we need to do a 8-dimension integral to calculate the diffuse intensity of one defect at a certain height  $d$ . If some averaging of the defect height is needed, then 9 dimensions of integration is necessary. For numerical integration purpose, assuming we take 100 points in each dimension, the amount of calculation is at least a factor of  $10^6$  more than what is required in Kim's work. Even if we could get a computing power that is 1000 times faster than before, the remaining factor of 1000 for the computing time is still unrealistic.

Unfortunately, we could not perform a directly calculation of the diffuse intensity from theoretical equations. We have to take some indirect approaches by looking at the results from some simple models or simulations.

## 6.4 Analysis of Amar's simulation results

The simulation data from Amar's group[59] is analyzed in order to study the displacement field from the surface morphology. We received and analyzed three simulation data files of low-temperature Cu/Cu(100) growth with a deposition angle of 60 degrees, which are the exact simulation data published in Shim et al.[54]. One simulation, MDCu, corresponds to a MD run at 110 K with long range attraction for system size  $L = 192$  at a coverage of 7 ML and includes 13 layers of substrate. Two other simulations using TAD were also received: a 6 ML film at 77 K and a 7 ML film at 40K; both having a deposition rate of 5000 ML/s and a system size of  $L=72$  with 6 layers of substrate.

The MD simulation data is chosen for a detailed analysis, because the simulation

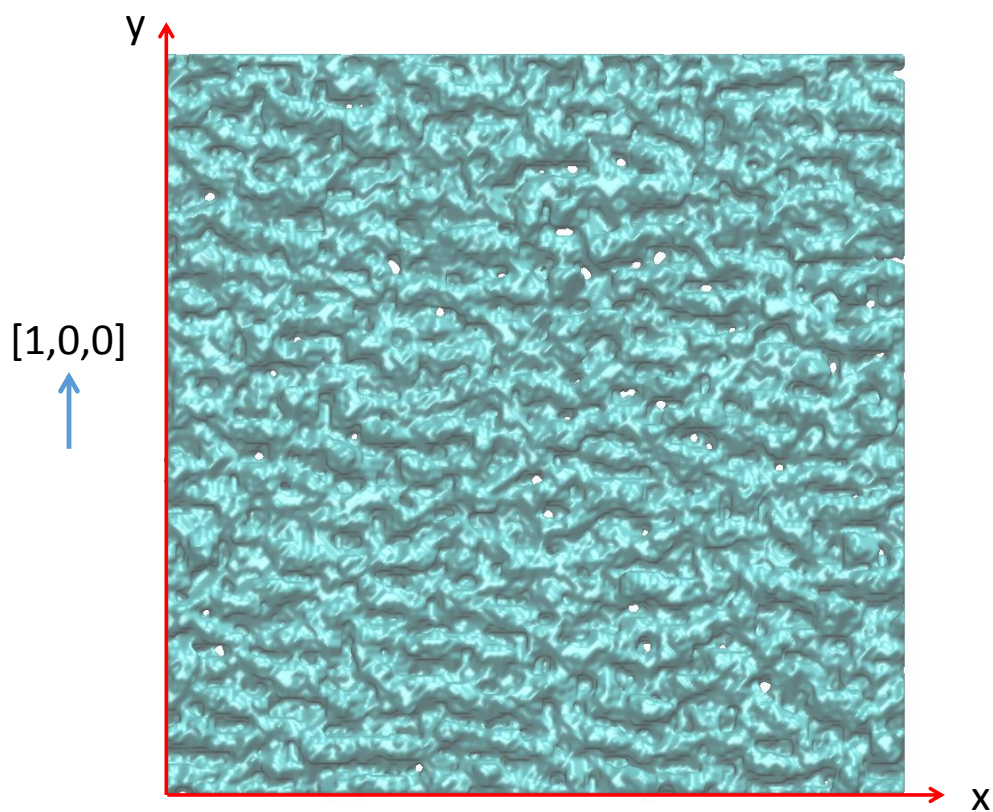


Figure 6.6: Top view of the MD simulation result for 7 ML deposited film of Cu/Cu(100) with a deposition angle of 60 degrees from Amar[59]. The arrow indicates the assumed azimuthal orientation of deposition. Only the film part of the data is plotted, the substrate is not included in the figure, that is the reason why some holes can be seen. There are a lot of ridges created across the whole surface. Figure is created with Visual Molecular Dynamics (VMD) software[60].

is done at a temperature that is closer to our experiment and the system is larger than the other two. In a cubic coordinate system for Cu(100) there are atoms on the half integer sites because Cu has FCC structure. Just for convenience, the simulation coordinate system is chosen that all atomic sites have integer values. The x,y,z coordinate are in units of half lattice constant. The Cu atoms fill only half of the sites, there are  $0.5 \times 192 \times 192 = 18,432$  atoms per layer for bulk. The system has a total of 368,672 atoms for film plus substrate. There are 26 layers in the system. Layer 0 through 12 is the substrate, they have full density as bulk. The atoms in layer 0-2 were constrained at ideal bulk positions whereas atoms in the rest of the substrate layers were allowed to have some displacement from ideal positions. Layers 13-25 are the deposited film, it has a total of 129,056 atoms. There are 7 ML worth of atoms in 13 layers. Note that there are progressively fewer atoms in the top layers due to surface roughness. For example, the top layer only has 6 atoms in it.

A top view of the MD simulation result is shown in Fig. 6.6, which is generated by Visual Molecular Dynamics (VMD) software[60]. The +x, +y directions are shown in-plane, and the +z direction is out of the page. It shows a large amount of ridges across the whole surface. As shown in Fig. 6.2, the ridges generated from the deposition angle are perpendicular to the azimuthal orientation of deposition for the TAD simulation. So it is assumed that the simulated deposition is in the y-z plane for this MD simulation.

### 6.4.1 The average surface normal strain

Using the x,y,z coordinate system from the simulation results, we calculated the atomic displacement from ideal positions. Realizing that there could be both positive

(% of lattice constant)

Layer	# of atoms	Total Displacement			Layer Average Displacement			
		x	y	z	x	y	z	
Substrate	0	18432	0.0	0.0	0	0.000	0.000	0.000
	1	18432	0.0	0.0	0	0.000	0.000	0.000
	2	18432	0.0	0.0	0	0.000	0.000	0.000
	3	18432	40.0	43.3	170	0.002	0.002	0.009
	4	18432	90.1	74.4	471	0.005	0.004	0.026
	5	18432	116.1	113.4	722	0.006	0.006	0.039
	6	18432	149.3	149.3	968	0.008	0.008	0.053
	7	18432	182.5	186.2	1207	0.010	0.010	0.066
	8	18432	212.0	218.4	1447	0.012	0.012	0.079
	9	18432	237.8	250.7	1659	0.013	0.014	0.090
	10	18432	267.3	280.2	1862	0.015	0.015	0.101
	11	18432	289.4	312.4	2064	0.016	0.017	0.112
	12	18432	306.0	330.9	2221	0.017	0.018	0.121
Film	13	18336	355.7	377.7	1834	0.019	0.021	0.100
	14	17924	342.3	323.5	-810	0.019	0.018	-0.045
	15	17175	314.3	407.0	-6544	0.018	0.024	-0.381
	16	16247	211.2	808.3	-15110	0.013	0.050	-0.930
	17	15137	206.6	1158.0	-25430	0.014	0.077	-1.680
	18	13707	8.4	1411.8	-35981	0.001	0.103	-2.625
	19	11760	-268.7	1170.1	-43159	-0.023	0.100	-3.670
	20	9120	-44.0	829.9	-43913	-0.005	0.091	-4.815
	21	5864	231.6	894.3	-35184	0.040	0.153	-6.000
	22	2819	-37.1	1195.3	-20579	-0.013	0.424	-7.300
	23	818	-145.6	177.5	-6830	-0.178	0.217	-8.350
	24	143	-21.0	-20.9	-1316	-0.147	-0.146	-9.200
	25	6	15.7	-8.6	-81	2.615	-1.435	-13.550
Film Total	129056	1169.6	8724.0	-233103				
Average		0.0091	0.0676	-1.806		7.002ML		

Figure 6.7: The total displacement from ideal positions calculated for all atoms in each layer of the Cu/Cu(100) MD simulation result from Amar[59]. The layer average displacement is calculated from dividing the total displacement in each layer by the number of atoms in the layer. A total average displacement of the film is also calculated from summing up all the displacements from Layer 13 through 25 then dividing it by 129,056, which is the total number of atoms in the film.

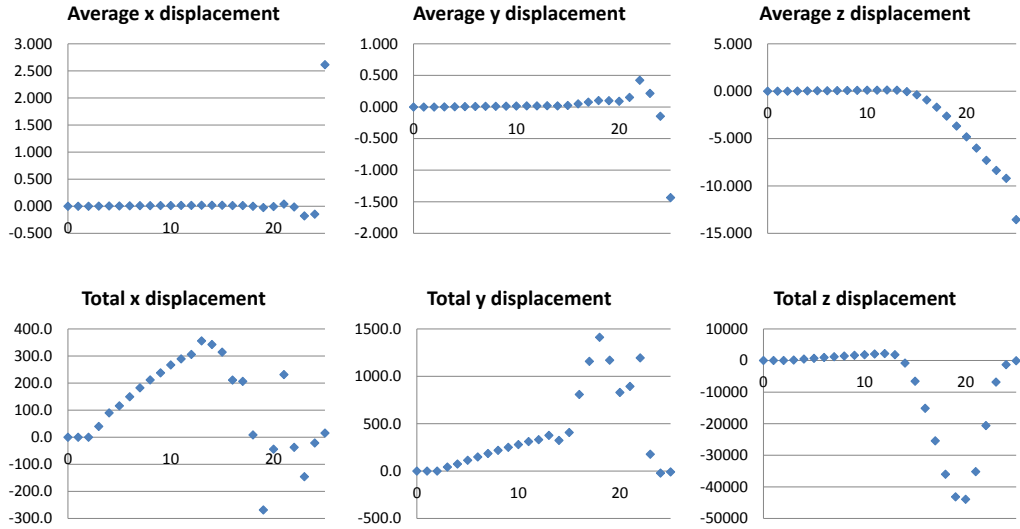
(% of lattice constant)

Layer	# of atoms	Total  Displacement			Layer Average  Displacement			
		x	y	z	x	y	z	
Substrate	0	18432	0	0	0	0.000	0.000	0.000
	1	18432	0	0	0	0.000	0.000	0.000
	2	18432	0	0	0	0.000	0.000	0.000
	3	18432	219	249	198	0.012	0.014	0.011
	4	18432	561	594	627	0.030	0.032	0.034
	5	18432	842	893	1032	0.046	0.048	0.056
	6	18432	1134	1198	1475	0.062	0.065	0.080
	7	18432	1428	1530	1972	0.078	0.083	0.107
	8	18432	1751	1898	2525	0.095	0.103	0.137
	9	18432	2147	2387	3170	0.117	0.130	0.172
	10	18432	2663	3097	3917	0.145	0.168	0.213
	11	18432	3419	4230	4802	0.186	0.230	0.261
	12	18432	4636	6083	5889	0.252	0.330	0.320
Film	13	18336	6463	8856	7279	0.353	0.483	0.397
	14	17924	8263	11561	8962	0.461	0.645	0.500
	15	17175	9618	13311	12366	0.560	0.775	0.720
	16	16247	10398	14297	18359	0.640	0.880	1.130
	17	15137	10974	14759	27020	0.725	0.975	1.785
	18	13707	12131	15557	36940	0.885	1.135	2.695
	19	11760	12936	16817	44806	1.100	1.430	3.810
	20	9120	13042	17966	46512	1.430	1.970	5.100
	21	5864	10731	15891	38409	1.830	2.710	6.550
	22	2819	6921	10022	22834	2.455	3.555	8.100
	23	818	2806	4213	7853	3.430	5.150	9.600
	24	143	722	930	1544	5.050	6.500	10.800
	25	6	35	12	81	5.800	2.000	13.550
	Film Total	129056	105040	144192	272966			
Average		0.814	1.117	2.115	7.002 ML			

Figure 6.8: The total magnitude of displacement from ideal positions calculated for all atoms in each layer of the Cu/Cu(100) MD simulation result from Amar[59]. The layer average displacement magnitude is calculated from dividing the total displacement magnitude in each layer by the number of atoms in the layer. A total average displacement magnitude of the film is also calculated from summing up all the displacement magnitudes from Layer 13 through 25 then dividing it by 129,056, which is the total number of atoms in the film.



(a)



(b)

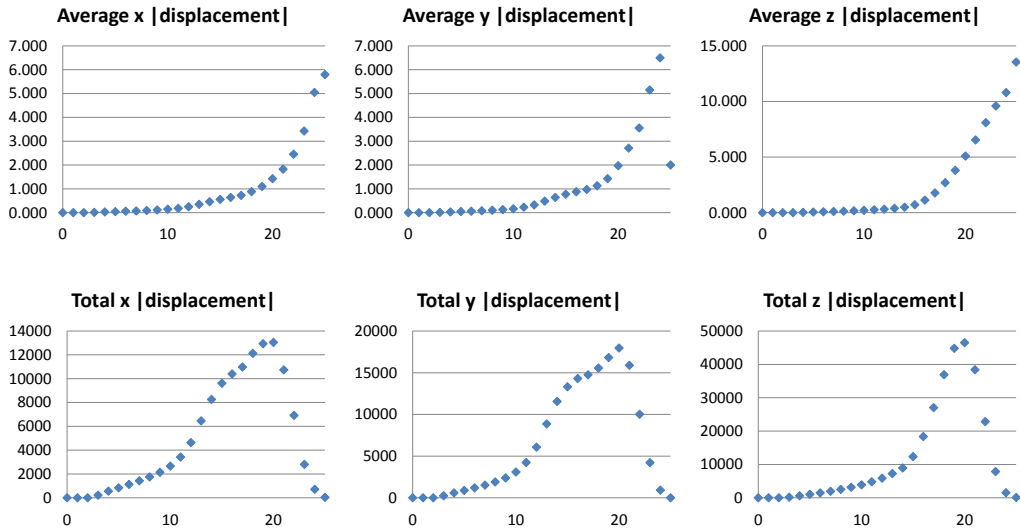


Figure 6.9: (a) The displacement and (b) the displacement magnitude versus layer height calculated from Cu/Cu(100) MD simulation result from Amar[59]. The vertical axes are displacement in percentage of the lattice constant, and the horizontal axes are the layer numbers. Part (a) is plotted from the table in Fig. 6.7, and part (b) is plotted from the table in Fig. 6.8. In both cases, it clearly shows a compressive strain along the z direction.

and negative displacements, two tables are created, one for average displacements and one for average magnitude of displacements. As shown in Fig. 6.7, all atomic displacements are added up in each layer to calculate a total displacement within the layer, a layer average displacement is also calculated by dividing the total displacement within a layer by the number of atoms in that layer. The average displacement (in unit of lattice constant) of all the atoms in the film part is 0.009% in the x direction, 0.068% in the y direction, and -1.81% in the z direction. And Fig. 6.8 shows that if we look at the average *magnitude* of the displacement, it is now 0.81% in the x direction, 1.12% in the y direction, and 2.12% in the z direction. This big increase of number in the x,y direction indicates that most displacements in the x,y direction are opposite to each other, so they almost completely cancel out when added up to calculate the total displacement. Whereas in the z direction, we truly see a downward (negative) displacement.

It is hard to conclude anything about the in-plane strain in the film from the statistics above. But in the z direction, it can be clearly seen that there is a compressive strain, as shown in Fig. 6.9. Using  $\frac{\Delta d}{d} = \frac{d_{film} - d_{bulk}}{d_{bulk}}$  where  $d_{film}$  is the average lattice spacing in the film, the average compressive strain in the z direction is calculated as 1.8%. And it should be pointed out that in Shim et al.[54], the average compressive strain is calculated over all film plus substrate. Since we should only calculate  $d_{film}$  from film part, and there is no strain in the substrate, the result they reported is much smaller than the correct value.

## 6.4.2 Local in-plane displacement

Since the statistics does not tell us anything about the overall average in-plane strain, we want to investigate the *local* in-plane strain. Our group performed x-ray diffuse measurements, and revealed unexpectedly large vacancy clusters of about 40 atoms with a small concentration of 0.05% [52, 53]. We want to see how well this simulation result agrees with our experimental results.

The easiest way to make the comparison is to directly calculate the diffuse intensity along in-plane directions from the simulated atomic positions. But there are 192 rows of atoms in the x-y plane, the finite size effect will introduce extra oscillations with the period of  $1/192=0.0052$  in  $Q$  (this will be discussed in section 6.5), even after some treatment to smooth out the curve, the result still does not look meaningful at all. So a deeper look into the local displacement in the simulation data is necessary.

The simulation data is a big 3-dimension array which can be sliced into different x-z (or y-z) planes. All the atoms that are within 0.5 of a certain y (or x) values are investigated (rounding to the nearest integer is used to determine which slice of cross section each atom belongs to). After looking through all x-z and y-z cross sections of the film, together with the in-plane displacement map (x-y cross sections), we are able to locate the features in different positions inside the film.

In the simulation coordinate system, all ideal atomic sites have integer values. Therefore when the atomic positions from simulations are plotted in Fig. 6.10, the grids of the coordinate indicate the ideal bulk positions. And two neighboring cross sections will be plotted together so there will be one atom at every grid point.

Two major sources for the in-plane displacements are observed: overhanging and surface roughness. Similar to what is shown in Fig. 6.10a, about 40 overhanging

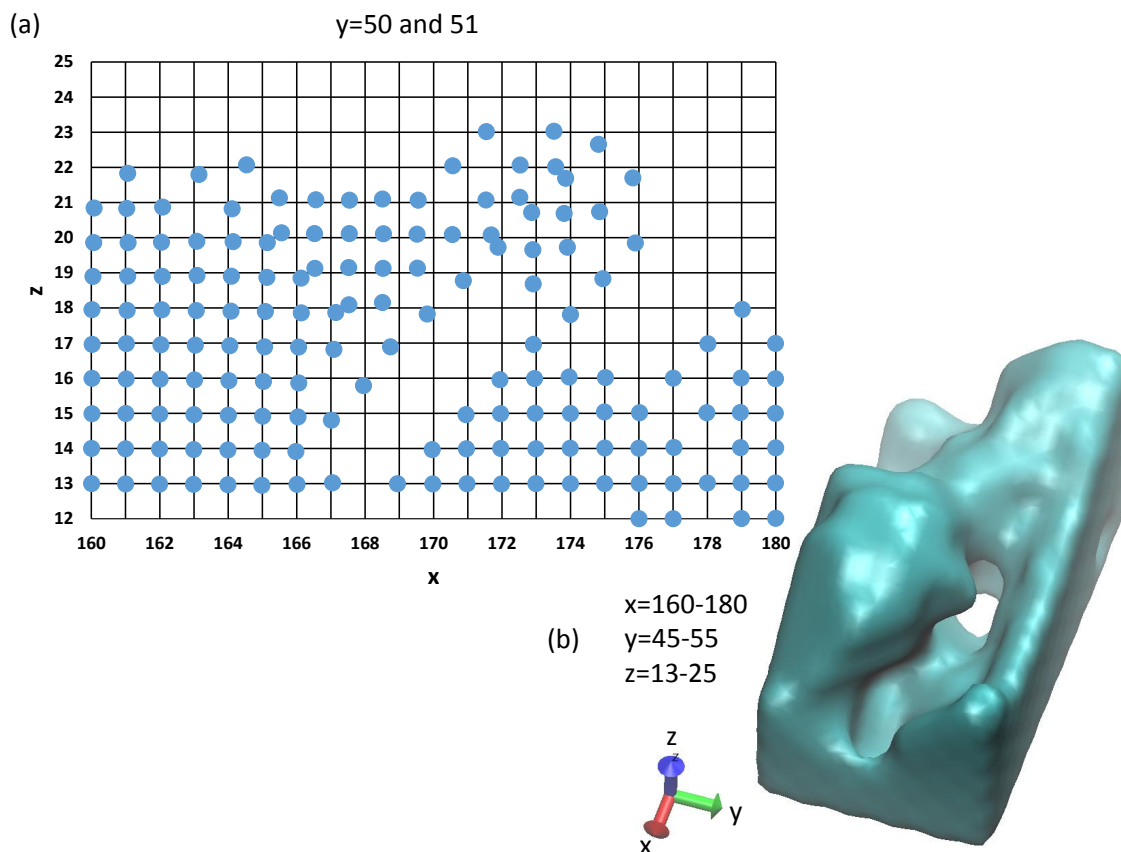


Figure 6.10: A typical example of overhanging and surface roughness in the simulation data from Amar[59]. (a) A 2D  $x$ - $z$  cross section of the film. Each grid point represents the ideal bulk position, and the circles are the atomic positions from simulations. The coordinate is in units of half lattice constant. Note that the nearest neighbor atoms are half lattice constant away in the  $y$  direction, they are not as close as it appears to be. Layers 12 and below are substrate, some atoms of layer 12 are not in the plot because their positions are slightly lower than the ideal position. (b) 3D view of the same region of the film created with VMD[60]. The 2D cross section is in the middle of the  $y$  range in the 3D view.

cites are found in the total of 129,056 atoms of the film. All of the overhanging are along the y direction which comes from the deposition direction. Only 7 ML film is deposited in the simulation, if further deposition is continued, it is reasonable to expect these overhangs to close and form vacancy clusters. In the 7 ML film, assume an average of 10 atoms are missing underneath each overhanging,  $40/129,056$  gives 0.03% of concentration of missing atom cites. This is not too far off from the average vacancy of 40 Ag atoms and the concentration of 0.05% of vacancy from 100 ML of Ag/Ag(001) in-situ diffuse experiment by our group[52, 53].

From Fig. 6.10a, it can also be seen that a lot of atoms are displaced far away from the ideal positions near the top of the film. These atoms still keep a close to bulk lattice spacing between themselves in the x direction, as if they are displaced together in groups. This planar displacement of surface roughness shows up pretty often in the film. And in fact, most of the super large in-plane displacements are from such surface roughness. The displacement could go as large as 25%-30% of lattice constant, although there are not many atoms that have super large in-plane displacement. And strangely almost all super large in-plane displacements are along the diagonal directions ( $\pm\hat{x} \pm \hat{y}$  directions).

We now move to investigate the in-plane displacement created from the missing atoms underneath the overhanging, as shown in Fig. 6.11. For the majority of the 40 overhanging cites, the estimated number of atoms missing is about 10. The displacement from 10 missing atoms is not big enough to stand out from the displacement background as shown in Fig. 6.12. (Fig. 6.10 belongs to the majority of the overhang cites.) Only two large hollows are observed where there are enough atoms missing in some extended region in the film. They are named “90-110 60-70” and “65-85

130-140” according to the x and y coordinate ranges. The region “90-110 60-70” that shown in Fig. 6.11 has about 20 missing atoms. The top opening of the hole is between x=99 to x=102, it is about four atoms wide in the x direction. A hollow forms further inside the hole between x=95 and 98. The cross sections of x=96 to 101 are shown in Fig. 6.11a.

Since the in-plane displacement is bigger along the y direction than along the x direction, how displacement field changes along the y direction is also investigated. The two regions with a big hollow are chosen for analysis and the displacements of atoms at certain x and z values are investigated along the y direction. Fig. 6.12 shows an example of such investigation around “90-110 60-70”, where the displacements of atoms at z=18, x=96 and 97 are investigated along the y direction as indicated by the red arrow in Fig. 6.11a. Fig. 6.12b shows the atomic displacement in the y direction, the atoms fluctuate about 3% of the lattice constant across the whole sample. The overall atomic displacement in the x direction is smaller than along y.

Fig. 6.12c shows that all atoms are, on average, displaced slightly negative in z direction, which corresponds to the developing average displacement in that layer and is consistent with Fig. 6.9a. However, the position of the defect has a displacement that is large and negative in the form of a peak; it does not have the cusp shape as in Fig. 6.12d. The difference between z and y (or x) direction must be due to the boundary conditions: there is a free surface along z but not along x-y.

It is clearly shown that in the y direction the atoms move towards the hollow from both sides, leading to positive displacement on one side, and negative displacement on the other side. We want to explore whether the y displacement follows the form of equation 6.15. The equations are derived with the assumptions that z=0 is at

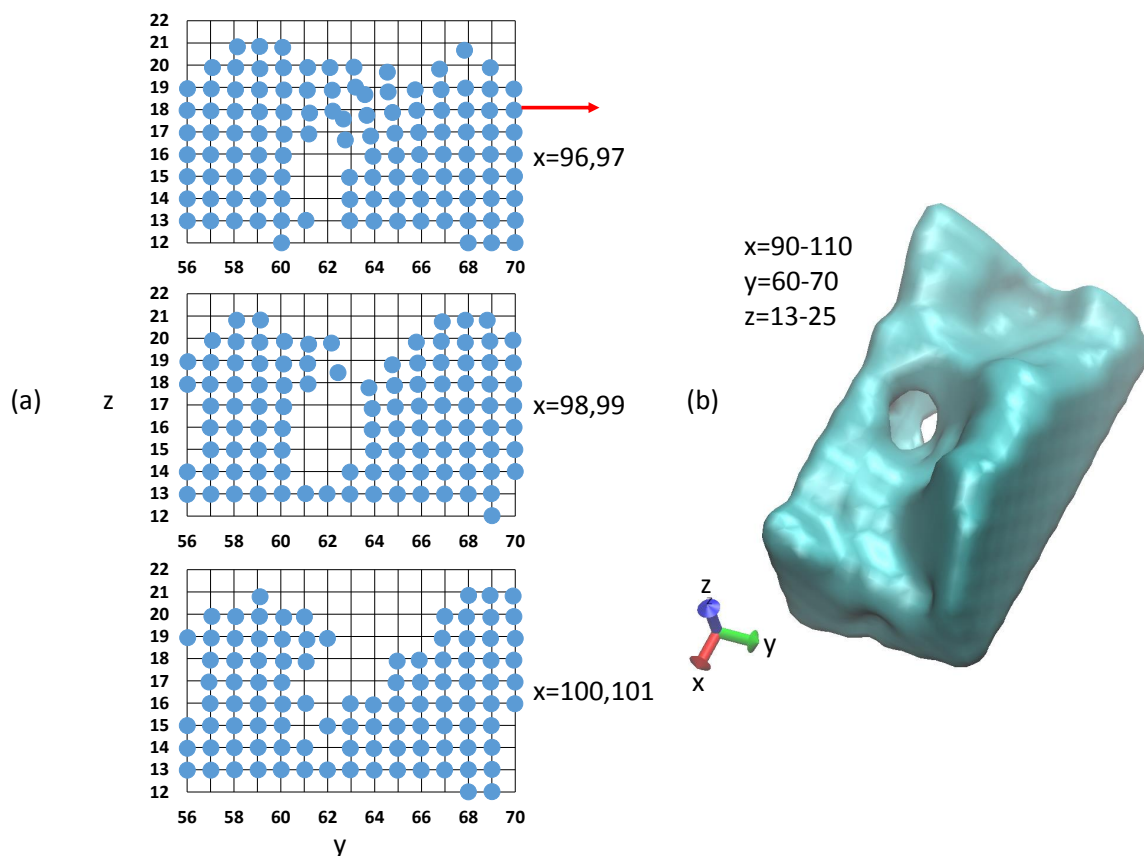


Figure 6.11: One example of a big hollow in the simulation data from Amar[59]. (a) 2D y-z cross sections near the hollow. Each grid point represents the ideal bulk position, and the circles are the atomic positions from simulations. The coordinate is in units of half lattice constant. Note that the nearest neighbor atoms are half lattice constant away in the y direction, they are not as close as it appears to be. Layer 12 and below are substrate, some atoms of layer 12 are not in the plot because their positions are slightly lower than the ideal position. (b) 3D view of the region that has a hollow.

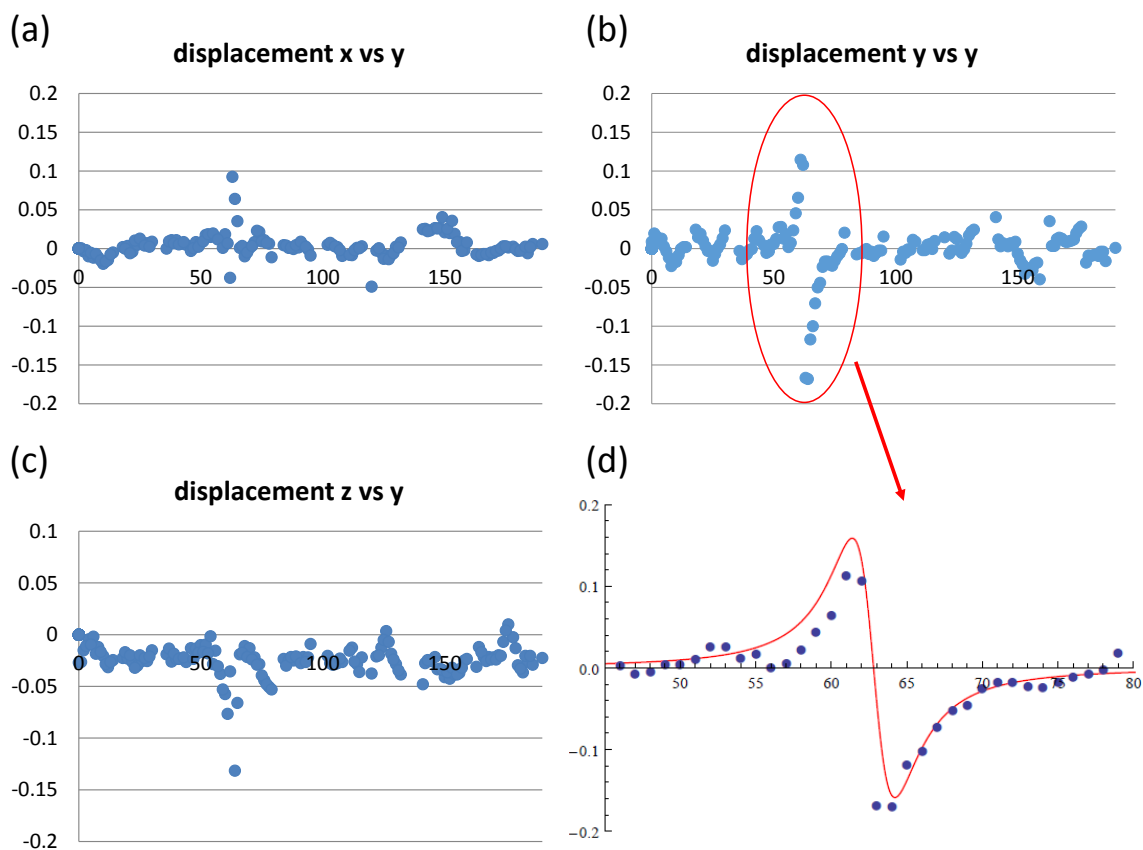


Figure 6.12: The (a) x component, (b) y component, and (c) z component of the displacement of atoms with height  $z=18$  and  $x=96$  and  $97$  investigated along the y direction as indicated by the red arrow in Fig. 6.11a. The vertical axes are in percentage of the lattice constant, the horizontal axes are the atomic positions. There is about 3% of the lattice constant of in-plane atomic fluctuation along the y direction. Less fluctuation is seen for displacement along the x direction, and only negative displacement is seen along the z direction. Part (d) shows a curve following the form of  $\frac{-1.6(y - 62.8)}{[(y - 62.8)^2 + 2^2]^{1.5}}$  for the y component displacements near the hollow.



the top of a uniform surface and the defect is at  $(0, 0, d)$ . Taking the defect center as  $(x_0, y_0, d)$ , Term 1 of  $u_y$  becomes  $\frac{b(y - y_0)}{[(x - x_0)^2 + (y - y_0)^2 + (z - d)^2]^{1.5}}$ , Term 2 becomes  $\frac{b(y - y_0)}{[(x - x_0)^2 + (y - y_0)^2 + (z + d)^2]^{1.5}}$ , assume Term 3 is very small and can be ignored for now. Our investigation is basically at fixed  $x$  values near the defect, take  $x = x_0$  (a small difference could be easily compensated by  $(z - d)^2$ ). Assume the height of the defect is at layer 16, our investigation is at layer 18, obviously  $(z + d)^2$  is a much large number than  $(z - d)^2$ . Therefore for locations  $y$  near the defect  $y_0$ , Term 1 dominates over Term 2. The equation  $\frac{-1.6(y - 62.8)}{[(y - 62.8)^2 + 2^2]^{1.5}}$  is used to plot the curve in Fig. 6.12d, which agrees well with the data. Since the displacement  $u_y$  is in units of the lattice constant  $a_c$  of Cu, and the coordinates are in units of half lattice constant  $a_c/2$ ,  $u_y a_c = \frac{b(y - y_0)(a_c/2)}{[(x - x_0)^2 + (y - y_0)^2 + (z - d)^2]^{1.5}(a_c/2)^3}$ ,  $b = -0.4a_c^3$ . Take the volume per atom of FCC Cu as  $\Omega = a_c^3/4$ ,  $b/\Omega = -1.6$  is dimensionless which can be compared between different systems. Our group's experiment [52, 53] gave  $b = -60 \text{ \AA}^3$ ,  $\Omega = (4.08^3/4) \text{ \AA}^3$  was used for Ag,  $b/\Omega = -3.534$ . The defect strength from the simulation has the same order of magnitude as our experiment.

### 6.4.3 Conclusion of the MD simulation

Simulation data of 7 ML Cu/Cu(100) deposited at 110K from Amar's group was studied. An average compressive strain of 1.8% in the surface normal direction is observed. The compressive strain in the  $z$  direction could reproduce the reflectivity measurement results in Ref#[50], the local strain observed in simulation data also agrees with the scattering theory.

Because of the large deposition angle in simulation, a large amount of ridges and overhangings are created. The missing atoms underneath the overhanging create in-

plane displacement that give rise to local strain. A hypothesis is made that when more material is deposited, some of the overhanging is going to close up and form vacancy.

## 6.5 Diffuse intensity calculation from simulated results

As discussed earlier in this chapter, we can not directly calculate the diffuse intensity in analytical (numerical) form from theory. So we explore what could be done with the atomic positions generated from models.

### 6.5.1 Finite Size Effect

One big problem of calculating x-ray scattering intensity from simulated atomic positions is that the number of atoms calculated is always much less than what is in the real sample and that will lead to unrealistic finite-size intensity oscillations.. For simplicity, let us take  $\vec{Q} = Q\hat{x}$ , the summation of  $e^{i\vec{Q}\cdot\vec{r}}$  just becomes  $\sum e^{iQx}$  and reduces the problem to one dimension. The fact that there are only finite numbers of calculated atomic positions introduces a step function to the electron density in the whole space  $\rho(r) = \rho_{\infty}(r)f(r)$ , where  $\rho_{\infty}(r)$  is the electron density from infinite numbers of atoms as in a real sample, and  $f(r)$  is a step like function and has value of one when  $r$  is within the calculated range of atomic positions and has the value of 0 when  $r$  is outside the calculated range.

In the way x-ray scattering intensities are calculated as shown in chapter 3, the structure factor of the whole crystal appears as the Fourier transform of the real space

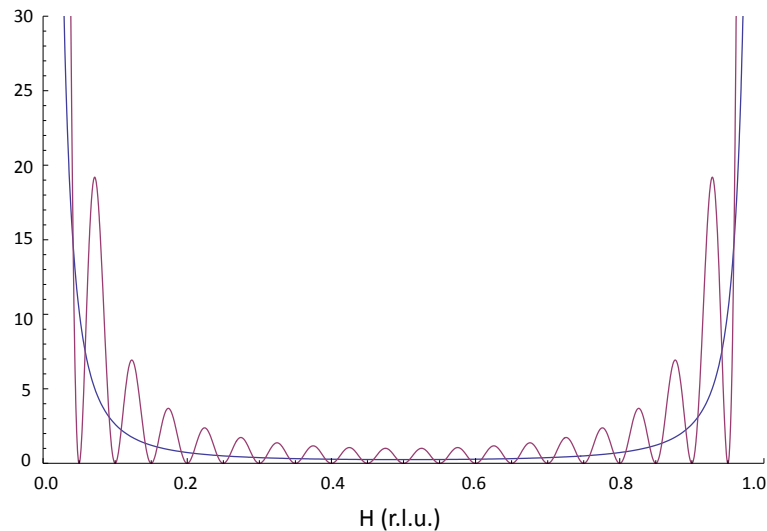


Figure 6.13: A simple example of Finite Size Effect. The intensity from a row of  $N$  atoms is shown as  $|\sum_{n=0}^{N-1} e^{i2\pi Hn}|^2$  for  $N=20$  and  $N=\infty$  (analytical form). The summation of only 20 atoms creates oscillations with the period of  $1/20$  whereas in ideal bulk case the intensity is flat between the Bragg peaks.

electron density function  $\rho(r)$ . After the Fourier transform the step like function  $f(x)$  becomes  $\frac{\sin(N\pi x)}{\pi x}$ , it is convoluted with the rest of information and creates oscillations. The period of the oscillation is inversely proportional to the number of summed atoms  $N$ . This is the so-called Finite Size Effect. (And ironically the more atoms you have, the more rapid the oscillation becomes.) When we want to calculate intensities along in-plane directions, this is where Finite Size Effect becomes a problem because we only have limited rows of atoms calculated in the  $x$  or  $y$  directions.

### 6.5.2 Treatment to smooth out the oscillations

Following equation 1 in Dederichs paper[55], the diffuse intensity can be calculated as

$$I_{diff} = \sum_m \sum_{m'} e^{i\vec{Q}\cdot(\vec{R}_m - \vec{R}_{m'})} (\langle e^{i\vec{Q}\cdot(\vec{u}_m - \vec{u}_{m'})} \rangle - \langle e^{i\vec{Q}\cdot\vec{u}_m} \rangle \langle e^{-i\vec{Q}\cdot\vec{u}_{m'}} \rangle), \quad (6.19)$$

where  $\vec{R}_m$  is the position of atom m in the ideal lattice,  $\vec{u}_m$  is the static displacement at this position, the atomic position  $\vec{r}_m = \vec{R}_m + \vec{u}_m$ , and the average is done over the whole sample. If all the atomic positions are given,  $\langle |\sum_m e^{i\vec{Q}\cdot\vec{r}_m}|^2 \rangle$  gives us the first term which is the total intensity,  $|\sum_m e^{i\vec{Q}\cdot\vec{R}_m}|^2 \langle e^{i\vec{Q}\cdot\vec{u}_m} \rangle^2$  gives us the second term which is the Bragg intensity. The total intensity minus the Bragg intensity gives us the diffuse intensity. And it should be pointed out that  $|\langle e^{i\vec{Q}\cdot\vec{u}_m} \rangle|^2$  is actually the static Debye-Waller factor  $e^{-2M}$ .

In an effort to explore a way to smooth out the rapid oscillations, we investigated a software package named DISCUS which claims to be able to generate diffuse scattering intensity maps from simulated structures. So the Cook Book Using the Program DISCUS[61] was looked through to learn how Finite Size Effect is dealt with. The method written in the book to get rid of Finite Size Effects is to choose the calculation grid size to be  $1/N$ .  $\frac{\sin(N\pi x)}{\pi x}$  has values of 0 when  $x = \text{integer}/N$ . As shown in Fig. 6.13,  $|\sum e^{iQr}|^2$  is calculated for a row of 20 atoms taking  $\vec{Q} = H\hat{x}$ , the intensities at  $H = \text{integer}/20$  is always at the extremes (peak and valley) of the oscillations. Choosing such grid size does eliminate Finite Size Effect in some way, but the intensity curve still does not follow the infinite crystal curve in the figure.

Another treatment from the DISCUS cookbook is to take the average  $\langle e^{i\vec{Q}\cdot\vec{u}_m} \rangle$

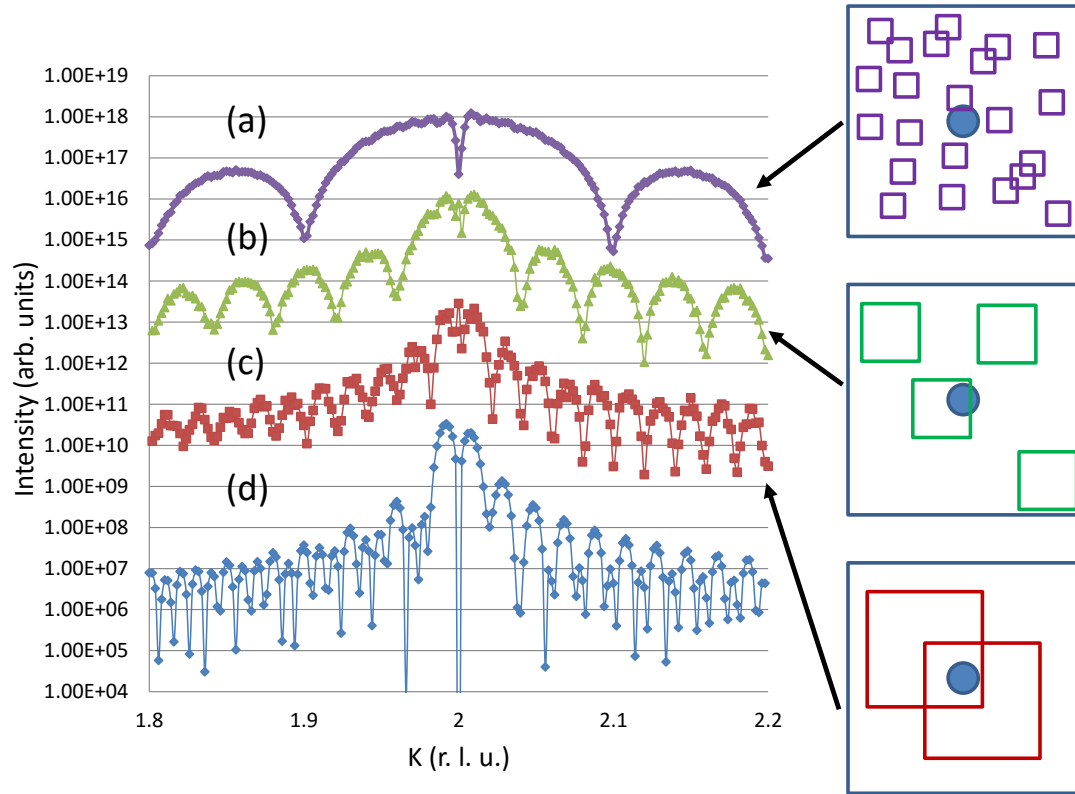


Figure 6.14: Diffuse intensity calculated from one defect with  $b=-60$  at the center of  $101^3$  atoms, a spherical displacement field  $\vec{u}(\vec{r}) = \frac{b\vec{r}}{r^3}$  is used. Summing over all the atoms creates rapid oscillations as shown in curve at the bottom, but averaging over the atoms in a number of small volumes that are randomly chosen creates oscillations from its own volume size. The intensity curves are from (a) averaging 200 times over a randomly chosen volume of 10 by 10 by 101, (b) averaging 32 times over a randomly chosen volume of 25 by 25 by 101, (c) averaging 8 times over a randomly chosen volume of 50 by 50 by 101, and (d) directly calculating the whole volume. Schematic diagrams are shown for averaging over a number of randomly chosen small volumes of 10 by 10 by 101, 25 by 25 by 101, and 50 by 50 by 101 in the whole volume of 101 by 101 by 101.

over a number of small volumes that are randomly chosen. A cubic array of 101 by 101 by 101 atoms with a spherical displacement field at the center is created for a test. The size of the chosen volume (especially the size of the x-y box) really affects the final intensity. As shown in Fig. 6.14, averaging 8 times over a randomly chosen volume of 50 by 50 by 101, averaging 32 times over a randomly chosen volume of 25 by 25 by 101, and averaging 200 times over a randomly chosen volume of 10 by 10 by 101 give very different results, because the small x-y box creates its own Finite Size Effect. Randomizing the volume size while randomly choosing the location of the volume was also tested, and the result does not seem meaningful. This treatment also does not help us smooth out the oscillations.

The last treatment we tried is to average over several data points to smooth out the oscillations. As shown in Fig. 6.15, taking an average value of several data points with different K values nearby (5 and 9 points were tested) with equal weighting helps, but taking an average of 9 data points nearby with Gaussian weighting works much better. The Gaussian weighting is calculated from  $e^{-\frac{x^2}{8}}$  with  $\sigma = 2$  for  $x=-4$  to 4. After normalization, the weighting of the 9 data points is taken as 0.0258, 0.0670, 0.1237, 0.1804, 0.2062, 0.1804, 0.1237, 0.0670, 0.0258, and the averaged value is used to represent the middle data point. The averaging is done for each point calculated at different K values, excluding the first and last 4 points which are removed for the smoothing. (Hundreds of data points are calculated in order to capture the features from the rapid oscillation, removing 8 points does not affect the results.) This 9 point Gaussian weighted averaging treatment to smooth out the calculated intensity curves is used for all the results shown later in this chapter.

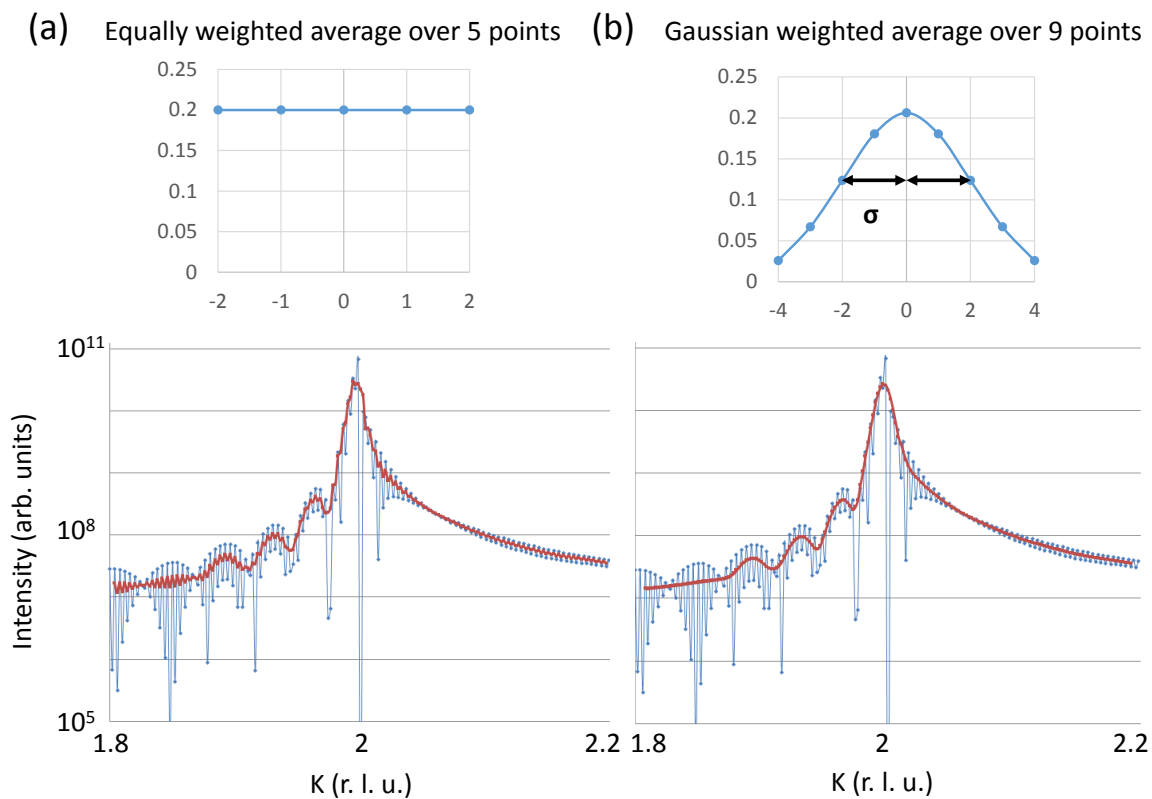


Figure 6.15: Averaging tests done to smooth out the oscillations from Finite Size Effects. The diffuse intensity is calculated from one defect with  $b=-60$  at the center of 501 by 501 by 41 atoms. Data points at different  $K$  values are averaged to represent nearby intensities. Gaussian weighted averaging over 9 points works better than equally weighted averaging over 5 points.

### 6.5.3 Random defect model

Tests to move one defect with a spherical displacement field to different locations in a 501 by 501 by 41 volume were investigated. As shown in Fig. 6.16, the location of the single defect has a big effect on the calculated diffuse intensity. The finite size of the system always creates a boundary for the displacement field, and depending on how far the defect is away from the boundary of the system, the fringes coming from this finite distance varies dramatically in the calculated intensity.

The location of the defect in the system affects the calculated diffuse intensity. On top of that, it is more realistic to have multiple defects randomly distributed throughout the whole volume, so a random defect model is created.

Let us first introduce how vacancy defects are added into an ideal system. The diffuse intensity is much more sensitive to the displacement field generated from the defect than the direct scattering from the defect atoms[57]. Therefore the direct scattering is neglected and the isotropic displacement from every defect  $\vec{t}(\vec{r}) = \frac{b\vec{r}}{r^3}$  is added at each atomic position, where  $\vec{r}$  is the vector from the defect location to different ideal atomic positions and  $b$  is the strength of the defect. The atoms at the vacancy sites are not removed from the atomic array in the calculations. A constraint is imposed that  $t=0$  when  $r=0$  exactly. Tests of actually removing atoms within  $r \leq 3$  lattice constant near defect locations were performed, and the intensity calculated at each data point differs by an average of 3% compared with no atom removal, which is a negligible difference.

To perform the calculation, we randomly generate the location of the defects, calculate the displacement field  $\vec{t}$  from each defect, and find the static displacement  $\vec{u}$  of each atom by summing up all the displacement fields, then we get the final atomic



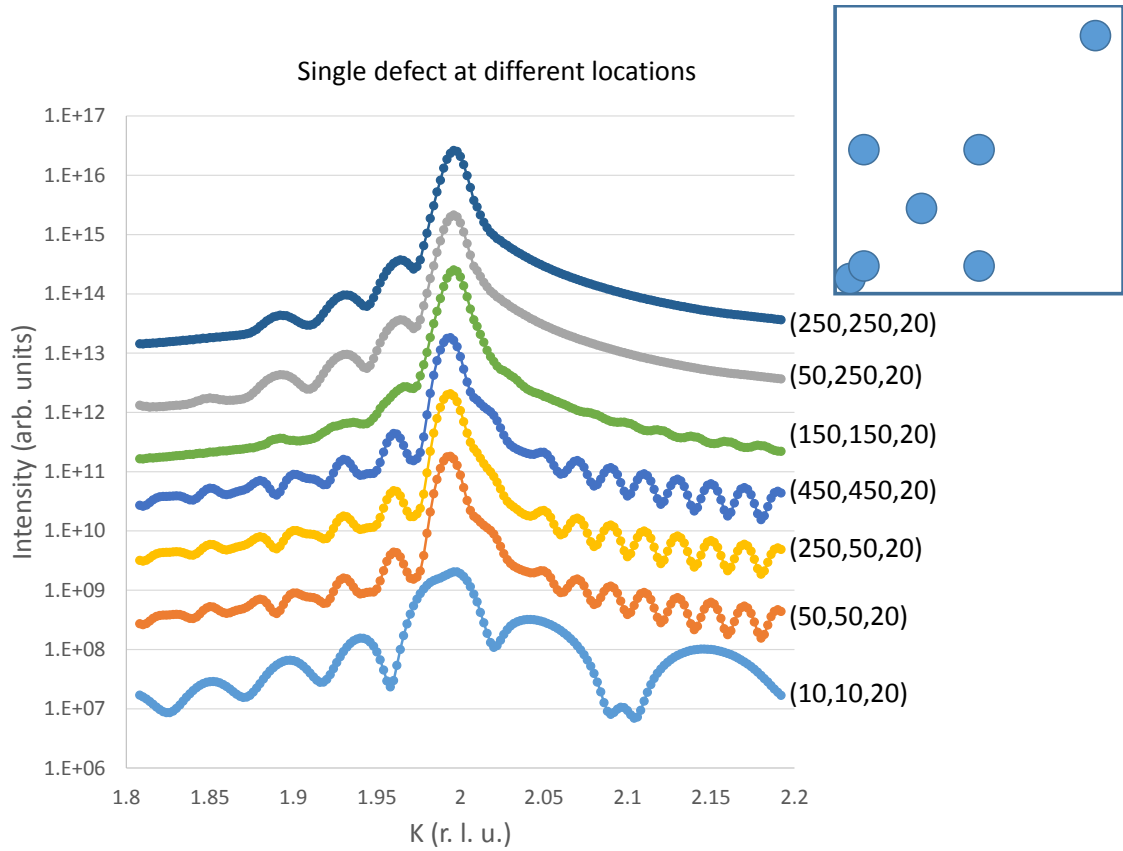


Figure 6.16: The diffuse intensity calculated from a defect with  $b=-60$  at different locations in the 501 by 501 by 41 atomic array. A schematic diagram in the top corner shows the different locations of the defect in the system, note that for each sample there is only one defect in the system. The intensity is calculated along the  $Q_y$  direction, so the x component of the distance between the defect location and the boundary of the system does not affect the calculated diffuse intensity. Defect at the same y location gives the same diffuse intensity, and defect at  $y=50$  and  $450$  also give identical diffuse intensities because the distance between the defect location and the boundary of the system is the same.

positions by adding the static displacement to the ideal atomic positions. In order to reduce the boundary effect seen in Fig. 6.16 and decrease the frequency of the rapid oscillation, we only use half of the volume in the center as the sample to calculate diffuse intensity while adding defects in the whole volume, which is illustrates in the schematic drawing of Fig. 6.17.

Our first test case was created by adding defects in a system of 126 by 126 by 126 ( $126^3=2$  million) volume, and calculate the diffuse intensity from the central 100 by 100 by 100 (1 million) atoms. Since the defects are randomly added to 2 million possible atomic locations, the calculated diffuse intensity would be different each time a sample is created, so that some statistical averaging is needed.

For each sample that is created, sum up the amplitude from all atoms,

$$A = \sum_m^{small\ volume} e^{i\vec{Q}\cdot\vec{r}_m}. \quad (6.20)$$

Then average over different samples and calculate the total intensity and the Bragg intensity,

$$I_{total} = \langle AA^* \rangle_{different\ samples}, \quad (6.21)$$

$$I_{Bragg} = \langle A \rangle_{different\ samples} \langle A \rangle_{different\ samples}^* .$$

The diffuse intensity is the difference between the total and the Bragg intensity,

$$I_{diffuse} = I_{total} - I_{Bragg}. \quad (6.22)$$

As the last step, 9 point Gaussian weighted averaging (as discussed in section 6.5) is done to smooth the curve.

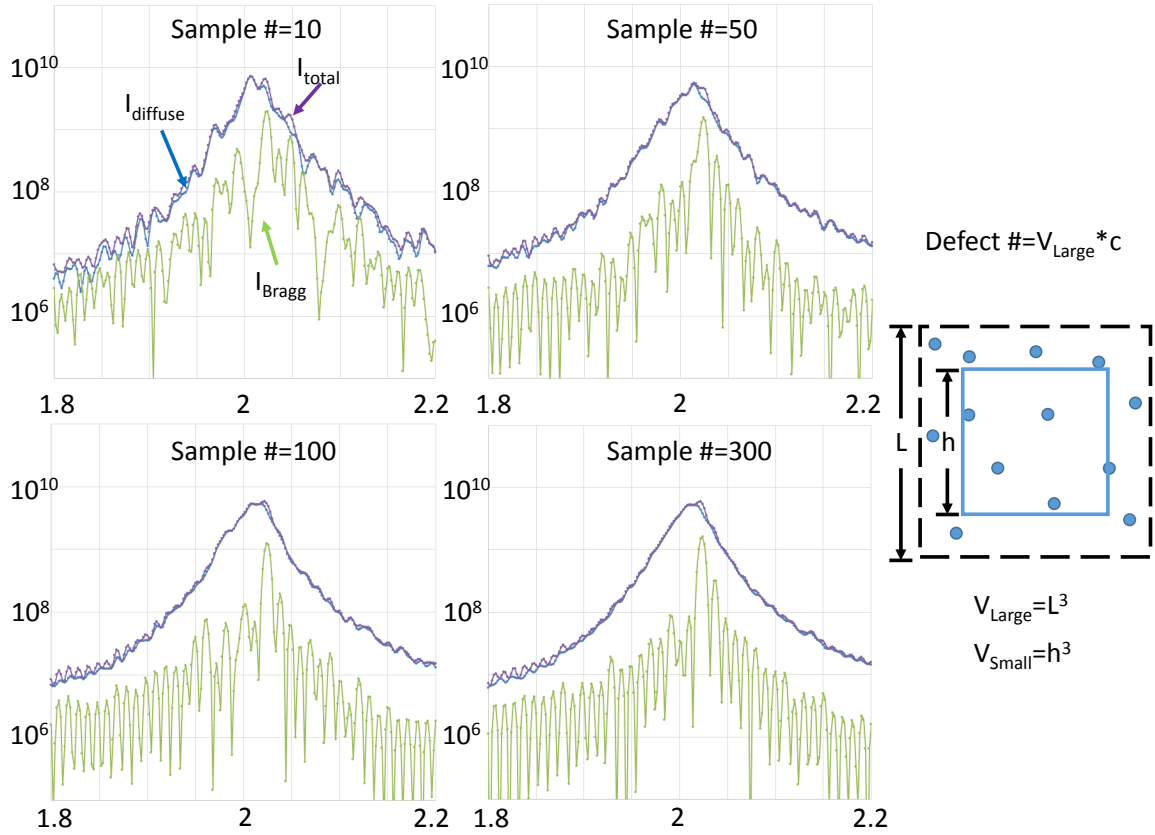


Figure 6.17: The intensities (without Gaussian weighted averaging) at different  $K$  values calculated from the random defect model with 100 defects having a defect strength  $b=-60$  and defect concentration  $c=0.00005$ . As shown in the schematic diagram, the defects are randomly added into the large volume with the defect number calculated from  $V_{Large}c$ . The total intensity and the Bragg intensity are calculated from averaging over a number of samples each containing all the atoms in the small volume. Averaging is done according to equation 6.21 to calculate the amplitudes from different samples. Averaging over 100 samples seems good enough to calculate the diffuse intensities. The Bragg peaks are dampened strongly from the static displacements of the atoms because  $b=-60$  is too large. The calculated diffuse intensity is very close to the Bragg intensity because of the large  $b$ . And it can be seen that the Bragg peaks are shifted from the integer locations because of the strain.

Tests with a defect concentration of  $c=0.00005$  (corresponds to 100 defects in the volume of 2 million atoms) were performed. As shown in Fig. 6.17, the difference between averaging over 100 samples (each has 1 million atoms) and 300 samples is not big, but averaging over 100 samples has big improvement from averaging over 50 samples. In order to save some computing time, averaging over 100 samples is chosen for the tests. (Some details about the calculation time is provided at the end of this chapter.)

To verify that our model is working, how the intensity and the location of the Bragg peak changes with defects is studied first. From the above test case, the Bragg intensity from summing 1 million atoms would be  $10^{12}$  without the static Debye-Waller factor. But as can be seen in Fig. 6.17, the Bragg peak intensity is much lower. From Ref#[53],  $M$  is calculated in closed form,

$$M = c \frac{4\pi R_c^3}{3\Omega}, \quad (6.23)$$

where  $R_c = \sqrt{Q|b|}$  and  $\Omega$  is the volume per atom. The defect strength  $b$  has the unit of  $\text{\AA}^3$ , which is the same as  $\Omega$ . As shown in Fig. 6.18, testing with a series of different  $b$  and  $c$  values and observing Bragg peaks up to  $K_n=8$ , our test result agrees with the theory.

For ideal bulk case Bragg peaks would only occur at integer points, but the local elastic displacements around the defects relates to the macroscopic homogeneous strain that leads to the shift of Bragg peaks, this could also be seen in Fig. 6.17 as the Bragg peak is not at the integer location of  $K=2$ . Also from Ref#[53], the relative

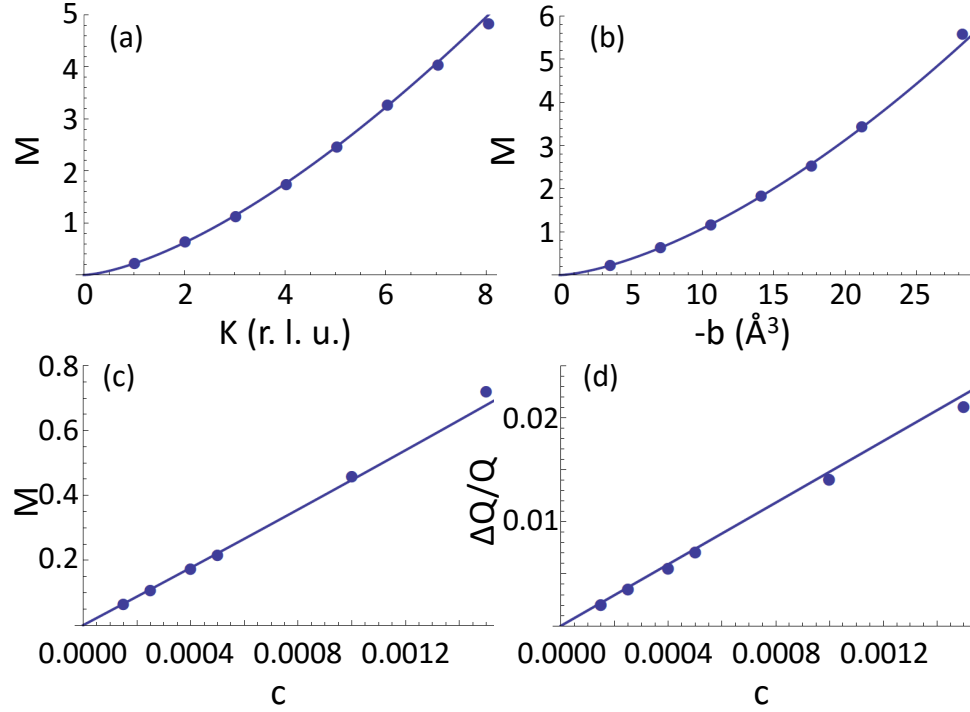


Figure 6.18: The observed shift and dampening of the Bragg peak from Random defect model. The test results are generated from adding defects in a volume of  $126^3$  atoms, calculating intensities from the central  $100^3$  atoms, and averaging over 100 samples. The intensities are calculated for momentum transfer  $Q$  along in-plane  $K$  direction. The static Debye-Waller factor  $e^{-2M}$  is calculated from the dampening of the Bragg peak intensity, and  $\Delta Q$  is observed from the shift of Bragg peak location. Part (a) shows the relationship between  $Q$  and  $M$ , the tests are done with  $b=-3.534$  and  $c=0.0005$ . Part (b) shows the relationship between  $-b$  and  $M$ , the tests are done with  $c=0.0005$  and  $K_n=1$ . Part (c) shows the linear relationship between  $c$  and  $M$ , the tests are done with  $b=-3.534$  and  $K_n=1$ . Part (d) shows the linear relationship between  $c$  and  $\frac{\Delta Q}{Q_n}$ , the results come from part (c). The solid line in part (a), (b), and (c) is a theoretical calculation from equation 6.23. The solid line in part (d) is a theoretical calculation from equation 6.25.  $\Omega = 1$  is used for all calculations.

lattice constant change can be described as

$$\frac{\Delta d}{d} = \frac{1}{3} \frac{\Delta V}{V} = \frac{1}{3} \frac{4\pi bc}{\Omega}, \quad (6.24)$$

for defects in infinite bulk material. The lattice constant is directly related to the Bragg peak position,  $Q = Q_n + \Delta Q = \frac{d}{d + \Delta d} Q_n$ , where  $Q_n$  is the bulk integer Bragg peak location,

$$\frac{\Delta Q}{Q_n} = -\frac{\Delta d}{d + \Delta d} \approx -\frac{\Delta d}{d} = -\frac{4\pi bc}{3\Omega}. \quad (6.25)$$

The shift of the Bragg peak location is proportional to  $c$ . As shown in Fig. 6.18, our test result also agrees with theory. (In our experiments, we did not observe any in-plane Bragg peak shift because of the epitaxial boundary condition. No boundary condition is applied for this test.)

Now we are ready to see whether the random defect model can reproduce our group's previous work[52, 53], using the observed defect strength  $b=60\text{\AA}^3$ , and the defect concentration  $c=0.0005$ . The volume per atom of Ag was calculated as  $\Omega = (4.08^3/4)\text{\AA}^3$ . In our model, the atomic array is using 1 as the lattice constant, it does not matter when calculating  $\vec{Q} \cdot \vec{r}$  since the resultant is a dimensionless quantity, but it matters for  $b$ . In order to match the defect strength, a normalization of  $b = \frac{-60}{4.08^3/4} = -3.534$  is needed in the dimensionless model where  $\Omega = 1$  ( $\frac{4\pi b}{\Omega}$  gives the number of atoms in the defect cluster). And  $c=0.0005$  corresponds to 1000 defects in the volume of 2 million atoms.

The intensities calculated from the random defect model are shown without Gaussian weighted averaging in Fig. 6.19. As can be seen, the Bragg intensity dampens more from the static Debye-Waller factor as we move to higher  $K_n$  values. The shift

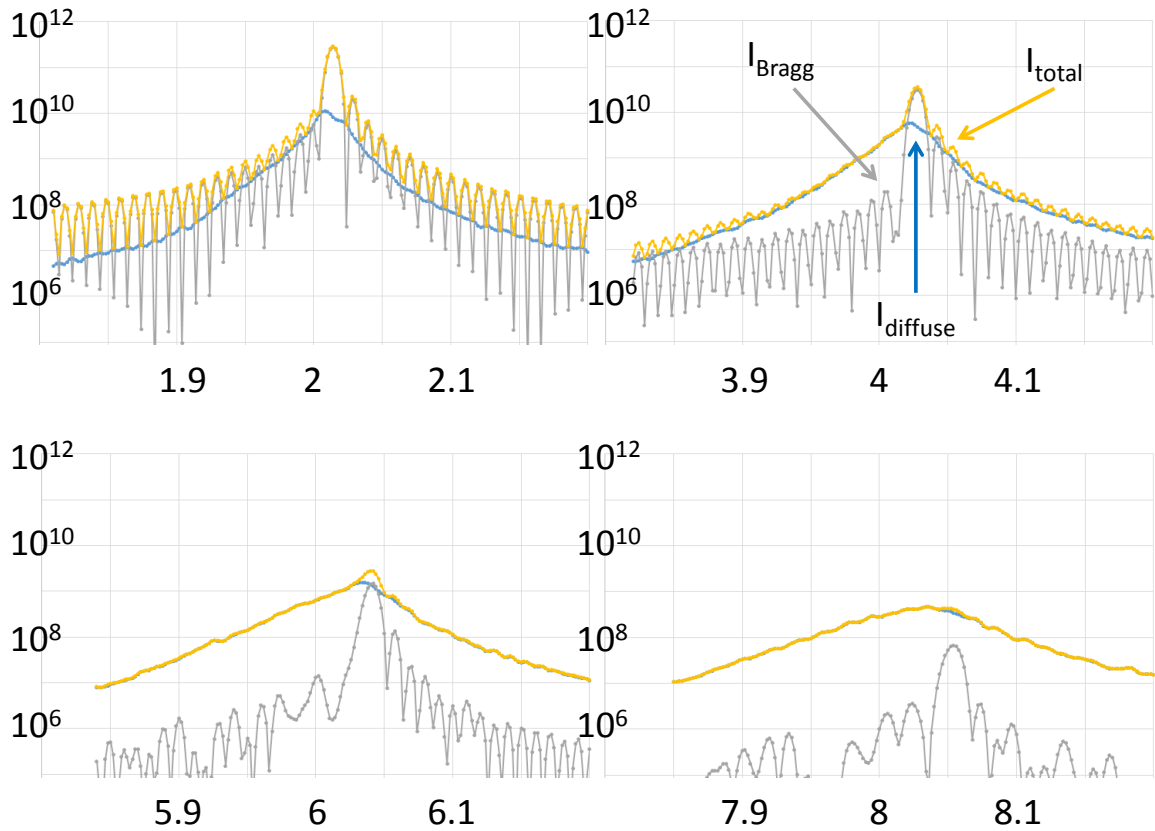


Figure 6.19: The intensities (without Gaussian weighted averaging) at different  $K$  values calculated from the random defect model with 1000 defects having a defect strength  $b=-3.534$  and defect concentration  $c=0.0005$ . Defects are added into the large volume of  $126^3$  atoms, the intensities are calculated from the central small volume of  $100^3$  atoms, and averaged over 300 samples.

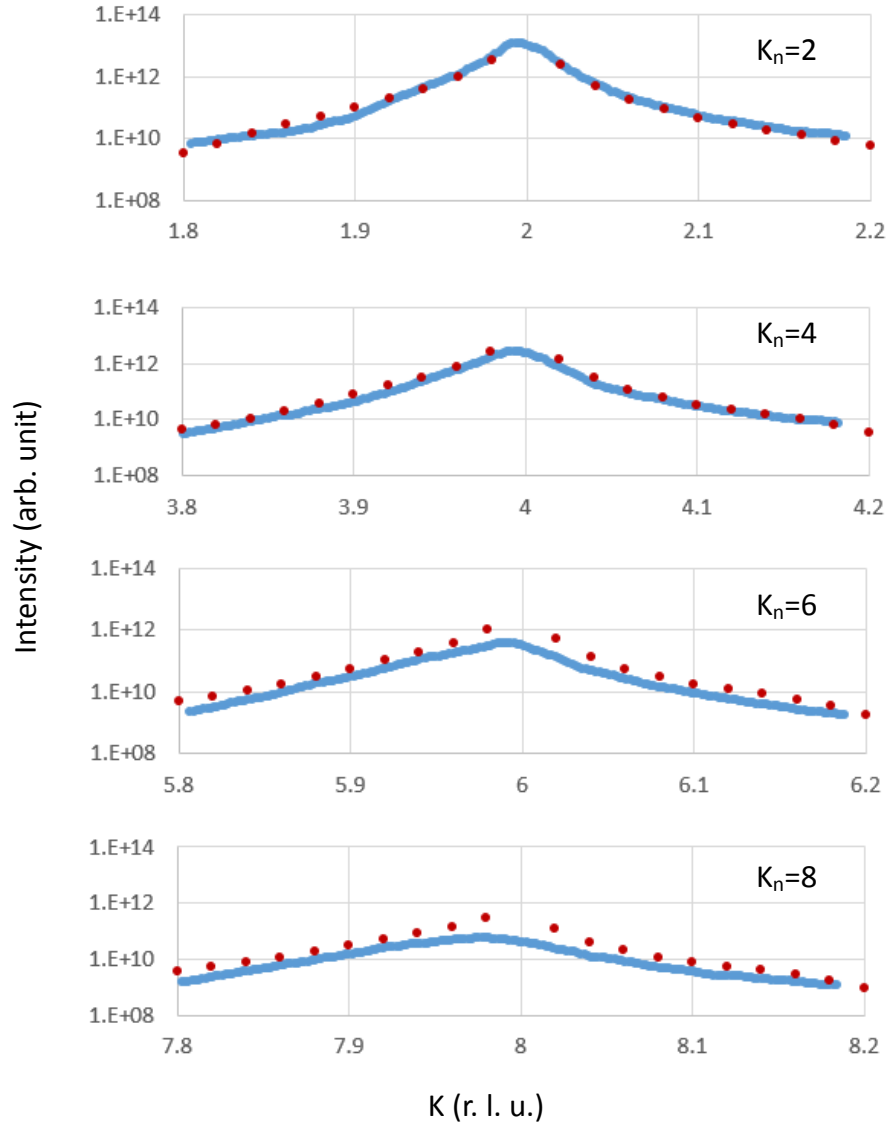


Figure 6.20: A comparison between the results from the random defect model and Kim's numerical calculation[52, 53]. The random defect model results are the diffuse intensities in Fig. 6.19 after Gaussian weighted averaging, and they include the Ag atomic form factor and the thermal Debye-Waller factor. The defect strength and concentration in the model are the same as what Kim used in Ref#[52]. The red dots are from Kim's calculation results, the blue lines are from the random defect model. One overall scale factor is used to generate all four model curves.



of the Bragg peak also increases with the  $K_n$  value. Taking the Ag atomic form factor and the thermal Debye-Waller factor into account, the random defect model results with Gaussian weighted averaging are compared with the results from Kim's numerical calculations for 100 ML Ag/Ag[52] in Fig. 6.20. It can be seen that the random defect model results are close to Kim's numerical calculations, although at the left side of  $K=2$ , the detailed shape of the two intensities are slightly different. One overall scale factor can not be used for all 4 intensity calculations at different  $K_n$  values to match Kim's results for reasons we do not understand. Roughly a factor of 2 difference is observed for  $K_n=6$  and 8 with the overall scale factor.

Tests were also performed to see whether a bigger volume of atoms would change the calculated intensities. We tried to add defects in a volume of  $504^3$  atoms, and calculate intensities from the central  $100^3$  atoms. We also tried to add defects in a volume of  $504^3$  atoms, and calculate intensities from the central  $160^3$  atoms. Tests were performed with the same defect strength  $b=-3.534$  and defect concentration  $c=0.00005$ . The tests were averaged over 100 samples. As shown in Fig. 6.21, there is some difference in the regions near the Bragg peak which are sensitive to the system size, but in the regions we are interested in which are away from the Bragg peak, the intensity is qualitatively the same for the 3 different test cases. So it is alright for us to use a relatively small system volume to do the calculations to save some computing time. It takes 1.5 hours to calculate 100 samples of  $100^3$  atoms each with 100 defects in  $126^3$  volume. It takes 7.5 hours to calculate 100 samples of  $100^3$  atoms each with 6400 defects in  $504^3$  volume. And it takes 29 hours to calculate 100 samples of  $160^3$  atoms each with 6400 defects in  $504^3$  volume. All calculations were done using an Intel Duo core computer with CPU at 3G Hz and 4GB memory.

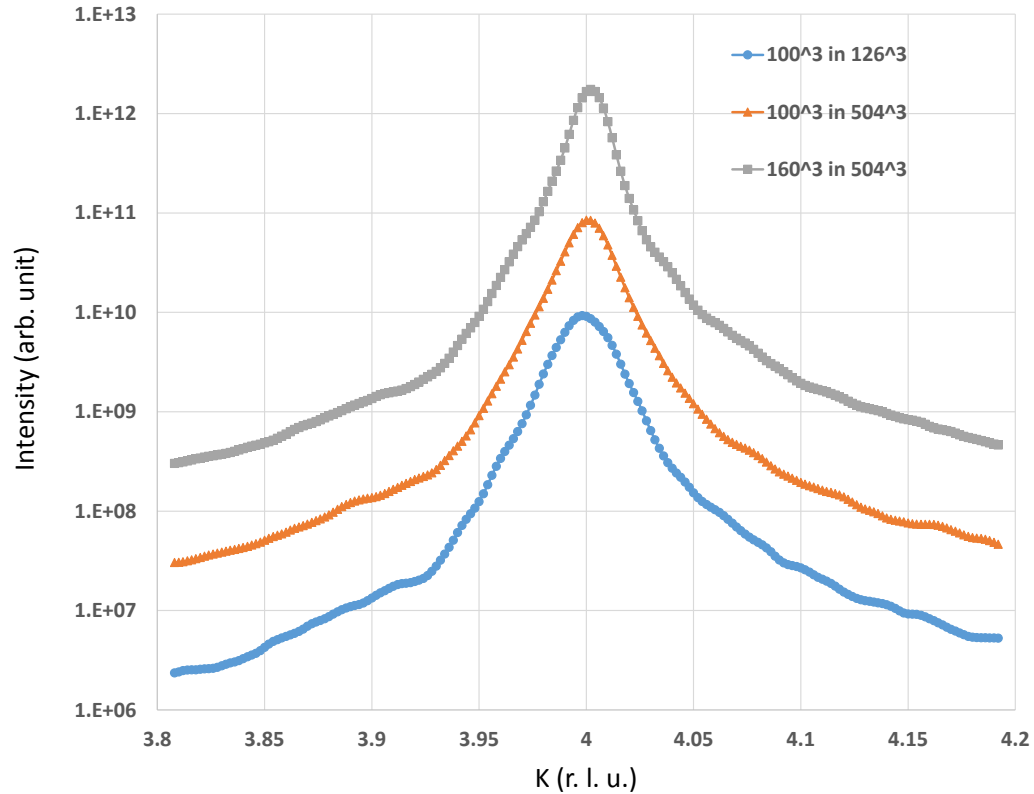


Figure 6.21: A comparison of the diffuse intensity of the random defect model with different system size and the same defect strength and defect concentration. The results are calculated from a sample of  $100^3$  atoms while defects are in  $126^3$  volume, a sample of  $100^3$  atoms while defects are in  $504^3$  volume, and a sample of  $160^3$  atoms while defects are in  $504^3$  volume. Averaged over 100 samples, the width of the central region is different due to system size, but the tails away from the Bragg peak where we are interested in are qualitatively the same.

#### 6.5.4 Conclusion

The finite size effect introduces extra oscillations when we calculate intensities from a number of atoms. Using a Gaussian weighted averaging method helps smooth out the oscillations in calculated curves. By randomly putting defects in a large volume and only calculate intensities from a small numbers of atoms also helps reduce the oscillations from the boundary of the system. By averaging over a number of simulated samples, we are able to reproduce a reasonable result for the 100 ML film which was treated as a bulk case. The right displacement fields is the only piece of information we miss in order to calculate the diffuse intensity for the thin film case.

# Appendix A

## Geometry Correction Calculations

Our diffractometer has 6 degrees of freedom to control the momentum transfer, 4 sample-orienting degrees of freedom and 2 independent detector degrees of freedom (although we don't use the  $\phi$  circle). It is a '4S+2D' type of six-circle diffractometer (referred as psi-circle diffractometer) as described in Ref#[62] instead of a six-circle surface diffractometer as described in Ref#[63]. As shown in Fig. A.1, the angles for the two diffractometers are a slightly different. Vlieg have a paper on how to do the geometry corrections for integrated intensities from a six-circle surface diffractometer[39], therefore some work needs to be done in order to use his equations in our psi-circle diffractometer.

### A.1 Motor angle conversion

One approach is to convert the angles between the two diffractometer systems, and use the converted angles in the equations.

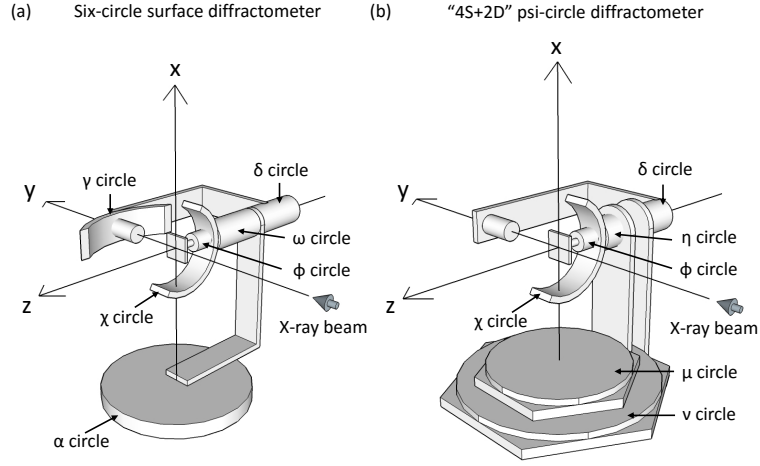


Figure A.1: Schematic drawings of (a) a six-circle surface diffractometer, and (b) a ‘4S+2D’ psi-circle diffractometer described in Ref#[39] and Ref#[62].

The major difference between a six-circle surface diffractometer and a psi-circle diffractometer is the detector angles. In a six-circle surface diffractometer, the  $\alpha$  circle moves the sample and the detector together, the detector related angles are  $\alpha$ ,  $\delta'$  ( $'$  is added here simply to distinguish from the other  $\delta$  angle), and  $\gamma$ . In psi-circle diffractometer, we have separate circles controlling the rotation of the sample ( $\mu$  circle) and the detector ( $\nu$  circle), we have 4 angles to control sample orientation and only 2 angles for the detector orientation,  $\nu$  and  $\delta$ .

We are going to use rotation matrices to describe the angle rotations. In reality the order of moving motors does not matter, because all the motor angles are with respect to fixed mechanical axes, moving  $\nu$  first then  $\delta$  is equivalent with moving  $\delta$  first then  $\nu$ . But when we use matrix calculations we have to pay special attention to the sequence we apply the rotations. Let us start the rotation from the initial position (as drawn in the Fig. A.1) where all angles are zero. For six-circle surface

diffractometer, the matrix operations are as follows, rotate counter-clockwise(CCW) around the x axis for angle  $\alpha$  (this must be done first because the axis of motor  $\alpha$  is fixed and won't move with the coordinate system after the  $\delta'$  motion), then rotate clockwise(CW) around the  $z'$  axis for angle  $\delta'$ , at last rotate CCW around the  $y''$  axis for angle  $\gamma$  (this must be done at last because other motor axes won't change together with the coordinate system after the  $\gamma$  motion). The rotation matrices are as follows,

$$A = \begin{pmatrix} 1 & 0 & 0 \\ 0 & \cos\alpha & -\sin\alpha \\ 0 & \sin\alpha & \cos\alpha \end{pmatrix}, \Delta = \begin{pmatrix} \cos\delta' & \sin\delta' & 0 \\ -\sin\delta' & \cos\delta' & 0 \\ 0 & 0 & 1 \end{pmatrix}, \Gamma = \begin{pmatrix} 1 & 0 & 0 \\ 0 & \cos\gamma & -\sin\gamma \\ 0 & \sin\gamma & \cos\gamma \end{pmatrix}. \quad (\text{A.1})$$

Going from the laboratory frame  $(x, y, z)$  to the  $\alpha$  frame  $(x', y', z')$ , we get  $K_{lab} = AK_\alpha$ , then from  $\alpha$  frame to  $\delta'$  frame  $(x'', y'', z'')$ , we get  $K_\alpha = \Delta K_{\delta'}$ , at last from  $\delta'$  frame to  $\gamma$  frame, we get  $K_{\delta'} = \Gamma K_\gamma$ . In the  $\gamma$  frame, the outgoing beam is always  $\vec{K}_{f,\gamma} = (0, K, 0)$  where  $K = \frac{2\pi}{\lambda}$ . So in the laboratory frame, the outgoing beam (the detector position) direction is

$$\hat{K}_f = \frac{\vec{K}_{f,lab}}{K} = A\Delta\Gamma \begin{pmatrix} 0 \\ 1 \\ 0 \end{pmatrix}. \quad (\text{A.2})$$

Similarly in psi-circle diffractometer, rotate CCW around the x axis for angle  $\nu$  first,

then rotate CW around the  $z'$  axis for angle  $\delta$ , we get

$$V = \begin{pmatrix} 1 & 0 & 0 \\ 0 & \cos\nu & -\sin\nu \\ 0 & \sin\nu & \cos\nu \end{pmatrix}, \Delta = \begin{pmatrix} \cos\delta & \sin\delta & 0 \\ -\sin\delta & \cos\delta & 0 \\ 0 & 0 & 1 \end{pmatrix}, \quad \hat{K}_f = V\Delta \begin{pmatrix} 0 \\ 1 \\ 0 \end{pmatrix}. \quad (\text{A.3})$$

To convert from the psi-circle diffractometer to the six-circle surface diffractometer, use

$$\Delta\Gamma \begin{pmatrix} 0 \\ 1 \\ 0 \end{pmatrix} = A^{-1}V\Delta \begin{pmatrix} 0 \\ 1 \\ 0 \end{pmatrix} \Rightarrow \begin{pmatrix} \sin\delta' \cos\gamma \\ \cos\delta' \cos\gamma \\ \sin\gamma \end{pmatrix} = \begin{pmatrix} \sin\delta \\ \cos(\nu - \alpha)\cos\delta \\ \sin(\nu - \alpha)\cos\delta \end{pmatrix}. \quad (\text{A.4})$$

Intrinsically  $\alpha = \mu$ , then we obtain the relationship

$$\sin\gamma = \sin(\nu - \mu)\cos\delta, \quad \sin\delta' = \sin\delta/\cos\gamma. \quad (\text{A.5})$$

And to convert from the six-circle surface diffractometer to the psi-circle diffractometer, use

$$A\Delta\Gamma \begin{pmatrix} 0 \\ 1 \\ 0 \end{pmatrix} = V\Delta \begin{pmatrix} 0 \\ 1 \\ 0 \end{pmatrix} \Rightarrow \begin{pmatrix} \sin\delta' \cos\gamma \\ \cos\alpha \cos\delta' \cos\gamma - \sin\alpha \sin\gamma \\ \sin\alpha \cos\delta' \cos\gamma + \cos\alpha \sin\gamma \end{pmatrix} = \begin{pmatrix} \sin\delta \\ \cos\nu \cos\delta \\ \sin\nu \cos\delta \end{pmatrix}. \quad (\text{A.6})$$

We obtain the relationship

$$\sin\delta = \sin\delta' \cos\gamma, \quad \tan\nu = \frac{\sin\alpha \cos\delta' \cos\gamma + \cos\alpha \sin\gamma}{\cos\alpha \cos\delta' \cos\gamma - \sin\alpha \sin\gamma}. \quad (\text{A.7})$$

## A.2 Scattering angle calculation

The main parameter to control the measurements in the experiments is the momentum transfer  $(H, K, L)_H$ , rather than the motor angles (the motor angles are calculated through matrices from H, K, L values in the computer software automatically). It requires some extra steps to get the motor angles in the data analysis process. It is more convenient to use the momentum transfer information to calculate the scattering angles than converting the motor angles.

As shown in Fig. A.2, the incoming x-ray beam ( $\vec{K}_i$ ) is described by an out-of-plane angle  $\alpha_i$  (incident angle), the scattered beam ( $\vec{K}_f$ ) is described by an out-of-plane angle  $\alpha_f$  (exit angle). The incoming and outgoing beam makes a scattering angle  $2\theta$ , and the in-plane angle between them is  $\Phi$  (different than the motor angle  $\phi$ ). From the trigonometry nature of the momentum transfer shown in the figure, we get

$$\begin{aligned} Q_{\perp} &= K_i \sin\alpha_i + K_f \sin\alpha_f, \\ Q_{//}^2 &= (K_i \cos\alpha_i)^2 + (K_f \cos\alpha_f)^2 - 2(K_i \cos\alpha_i)(K_f \cos\alpha_f) \cos\Phi, \end{aligned} \tag{A.8}$$

where the wave vector magnitude  $K_i = K_f = K = \frac{2\pi}{\lambda}$ , the momentum transfer components  $Q_{//} = \frac{2\pi}{a_H} \sqrt{\frac{4}{3}(H^2 + HK + K^2)}$  and  $Q_{\perp} = Q_z = \frac{2\pi L}{c_H}$ . And we get

$$\begin{aligned} \sin\alpha_i + \sin\alpha_f &= \frac{\lambda L}{c_H}, \\ \cos\Phi &= \frac{(\cos\alpha_i)^2 + (\cos\alpha_f)^2 - \frac{4\lambda^2}{3a_H^2}(H^2 + HK + K^2)}{2\cos\alpha_i \cos\alpha_f}. \end{aligned} \tag{A.9}$$

Our measurements are operated in one of the three modes: fixed incident angle, fixed exit angle, or incident angle equals exit angle. Once we determine the operating



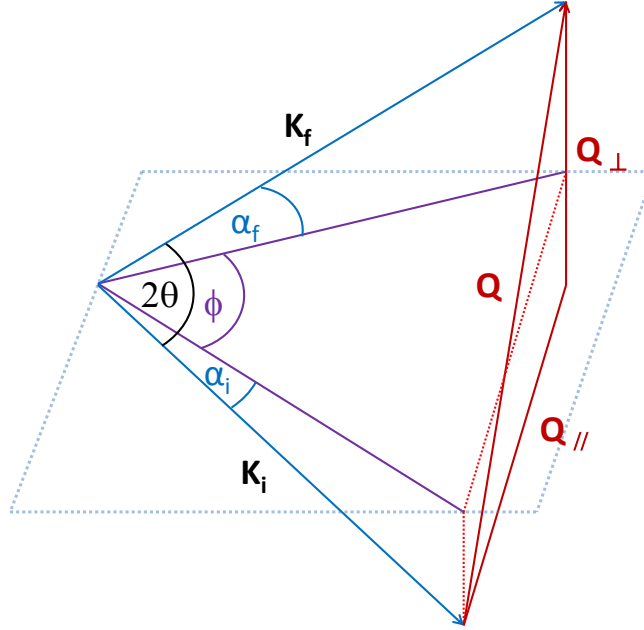


Figure A.2: The incoming beam  $\vec{K}_i$  and the outgoing beam  $\vec{K}_f$  have the incident and exit angles  $\alpha_i$  and  $\alpha_f$  with respect to the sample. The in-plane angle between the incoming and outgoing beams is  $\Phi$ . If we know the momentum transfer components  $Q_{//}$  and  $Q_{\perp}$  and some information about the operating mode, we are able to calculate the scattering angles  $\alpha_i$ ,  $\alpha_f$  and  $\Phi$  from trigonometry.

mode, we know  $\alpha_i$  or  $\alpha_f$  or  $\alpha_i = \alpha_f$ , we can get  $\alpha_i$  and  $\alpha_f$  from the first equation, and get  $\Phi$  from the second equation.

### A.3 Geometry corrections

Under the z axis mode (the mode we operate at) of the six-circle surface diffractometer, the incident angle  $\alpha_i = \alpha$ , the exit angle  $\alpha_f = \gamma$ , and the in-plane angle  $\Phi = \delta$ . Now we have the required detector angles to use Vlieg's equations[39]. Here I will keep angles in a six-circle diffractometer convention.

### A.3.1 Rocking scans (crystal truncation rod)

Crystal truncation rod is generally measured by doing rocking scans ( $\omega$  scans in six-circle surface diffractometer and  $\eta$  scans in psi-circle diffractometer).

**Lorentz factor.** Geometrical correction for the integration volume in the reciprocal space  $L_\varphi = \frac{1}{\sin\delta\cos\alpha\cos\gamma}$ .

**Rod interception.** The momentum transfer  $K$  range during rod measurements is not lined up with the surface normal direction. The projection of  $K$  range onto the rod direction gives the rod interception factor  $C_{rod} = \cos\gamma$ . (Rod interception factor cancels out the  $\cos\gamma$  term in the Lorentz factor, in our manuscript we combined it into the Lorentz factor so  $L_\varphi = \frac{1}{\sin\delta\cos\alpha}$ .)

**Polarization factor.** For synchrotron radiation, the polarization of the beam is almost completely horizontal, therefore the vertical polarization component is often neglected. The polarization factor  $P = P_{hor} = 1 - (\sin\alpha\cos\delta\cos\gamma + \cos\alpha\sin\gamma)^2$ .

#### Active area

The measured intensity is proportional to the area of the sample that is illuminated by the beam and viewed by the detector (this naturally comes from the in-plane summation of the structure factors). This is called the sample active area.

The active area is defined by the incoming beam and the detector field of view, as shown in Fig. A.3a. In the most general case, the active area  $A_{geo} = \frac{s_1 s_2}{\sin\delta}$  where  $s_1$  is the vertical beam size and  $s_2$  is the detector vertical field of view at the sample. As the incident angle  $\alpha$  increases, the horizontal beam footprint  $\frac{s_0}{\sin\alpha}$  decreases. Assuming a rectangular sample, some incident angles are defined in the following case limits:  $\alpha_1$  when the horizontal beam footprint is the same as the sample size  $d_{sample}$ ,  $\alpha_2$  when the horizontal beam footprint is about the same as the detector field of view,  $\alpha_3$  when

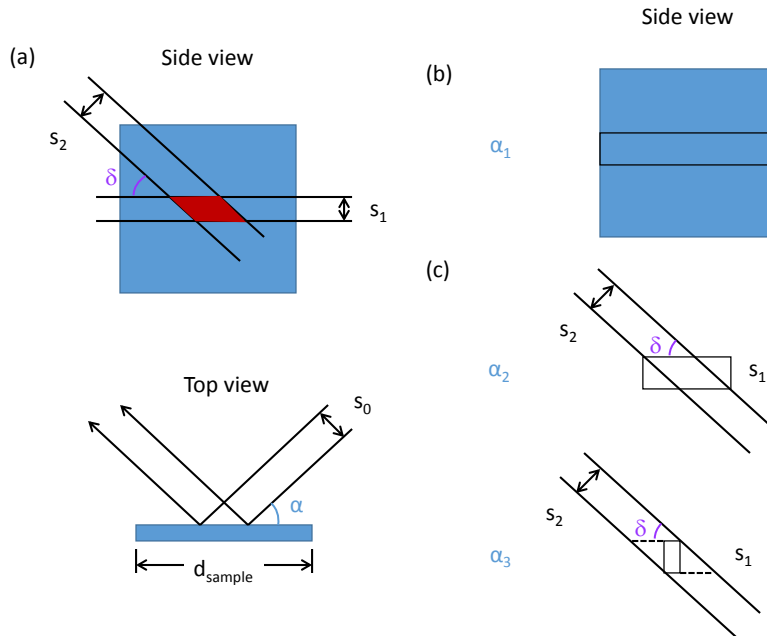


Figure A.3: (a) The active area on the sample is defined by the vertical incoming beam size  $s_1$  and detector vertical field of view  $s_2$  at the sample. The horizontal beam footprint is defined by the horizontal beam size  $s_0$  and the incident angle  $\alpha$ . (b) When the incident angle  $\alpha$  is very small, the beam footprint is bigger than the sample, as the incident angle increases, the beam footprint decreases. At incident angle  $\alpha_1$  the horizontal beam footprint is the same as the sample size  $d_{sample}$ . (c) The size of the beam footprint is compared with the detector field of view,  $\alpha_2$  and  $\alpha_3$  are defined at the two limits.

the horizontal beam footprint is smaller than the detector field of view. Use the beam footprint as the rectangle box in Fig. A.3b and c to view the situations.

$$\begin{aligned}
\frac{s_0}{\sin\alpha_1} &= d_{sample}, \\
\frac{s_2}{\sin\delta} + \frac{s_1}{\tan\delta} &= \frac{s_0}{\sin\alpha_2}, \\
\frac{s_0}{\sin\alpha_3} + \frac{s_1}{\tan\delta} &= \frac{s_2}{\sin\delta}.
\end{aligned} \tag{A.10}$$

Since we do not care about the sample area that is not illuminated by the beam, we can simply treat the sample as a  $d_{sample}$  by  $s_1$  slab. In some extreme cases where the in-plane angle  $\delta$  is small or the sample size  $d_{sample}$  is small, the following condition may happen  $d_{sample} < \frac{s_2}{\sin\delta} + \frac{s_1}{\tan\delta}$  or  $d_{sample} < \frac{s_2}{\sin\delta} - \frac{s_1}{\tan\delta}$ . In such two cases, beam footprint is bigger than the sample size, use the sample slab as the rectangle box in Fig. A.3c to view the situation limits, and they correspond to  $\sin\alpha_1 > \sin\alpha_2$  or  $\sin\alpha_1 > \sin\alpha_3$ . Considering our 10 mm by 10 mm sample size, 0.3 mm by 0.3 mm beam size, and 2.2 mm detector field of view calculated from two sets of 1 mm detector vertical slits, it is possible that these cases would happen.

The measurements are done in terms of momentum transfer  $L$ , and according to equation A.9,  $L$  is directly related with  $\alpha$ . I am going to use  $L, L_1, L_2, L_3$  instead of  $\alpha, \alpha_1, \alpha_2, \alpha_3$  to describe different conditions. From definition  $L_2 < L_3$ .  $L < L_2$  means beam footprint is bigger than detector field of view,  $L > L_3$  means beam footprint is smaller than detector field of view.  $L_1 < L_2$  means sample is bigger than detector field of view,  $L_1 > L_3$  means sample is smaller than detector field of view.  $L < L_1$  means beam footprint is bigger than the sample. Maybe some cases are not realistic in our measurements, but I will show the calculations for all possible cases just for

completeness.

Here are all the possible cases.

$$L \leq L_2,$$

$$\text{case 1, } L_1 > L_3, A_{geo} = d_{sample}s_1,$$

$$\text{case 2, } L_2 < L_1 \leq L_3, A_{geo} = \frac{s_1s_2}{\sin\delta} - x^2\tan\delta, \quad (\text{A.11})$$

$$x = \left( \frac{s_2}{\sin\delta} + \frac{s_1}{\tan\delta} - d_{sample} \right) / 2,$$

$$\text{case 3, } L_1 \leq L_2, A_{geo} = \frac{s_1s_2}{\sin\delta}.$$

$$L_2 < L \leq L_3,$$

$$\text{case 4, } L_1 > L_3, A_{geo} = d_{sample}s_1,$$

$$\text{case 5, } L \leq L_1 \leq L_3, A_{geo} = \frac{s_1s_2}{\sin\delta} - x^2\tan\delta, \quad (\text{A.12})$$

$$x = \left( \frac{s_2}{\sin\delta} + \frac{s_1}{\tan\delta} - d_{sample} \right) / 2,$$

$$\text{case 6, } L_1 < L, A_{geo} = \frac{s_1s_2}{\sin\delta} - y^2\tan\delta,$$

$$y = \left( \frac{s_2}{\sin\delta} + \frac{s_1}{\tan\delta} - \frac{s_0}{\sin\alpha} \right) / 2.$$

$$L > L_3,$$

$$\text{case 7, } L_1 \geq L, A_{geo} = d_{sample}s_1, \quad (\text{A.13})$$

$$\text{case 8, } L_1 < L, A_{geo} = \frac{s_0s_1}{\sin\alpha}.$$

If we want to compare the sample size (related with  $L_1$ ), beam footprint (related with  $L$ ) and detector field of view (related with  $L_2$  and  $L_3$ ), we need to rank the 4 parameters, there are all together 12 possible permutation cases ( $L_2 < L_3$  fixed). Fig. A.4 is provided to visualize the different cases and relate the equations from

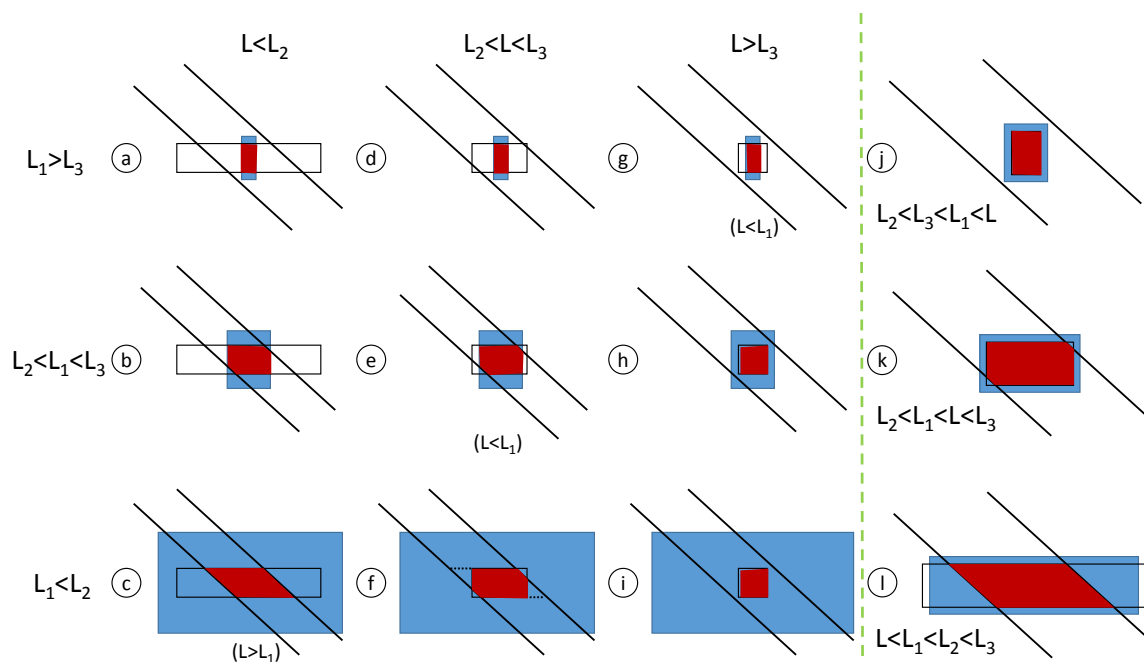


Figure A.4: Sample active area (red) in different typical cases with different relative sizes of the sample (blue), beam footprint (black rectangle) and detector field of view (tilted lines). The sizes of the sample, beam footprint and detector field of view are exaggerated in all cases. (a) to (i) are same scale, (j) to (l) are with a different scale.

calculation cases to the real situations. All 12 cases are drawn, Fig. A.4 a-g belongs to calculation case 1-7, Fig. A.4 h and i both belongs to calculation case 8. The other condition of Fig. A.4 g, e and c are drawn with different scale for exaggeration as Fig. A.4 j, k, and l, and they belong to calculation case 8, 6, and 3.

After calculating the active area  $A_{geo}$ , we get the active area correction factor  $C_{area} = \frac{A_{geo}}{A_0}$ , where  $A_0$  is a constant and we follow Vlieg to choose  $A_0 = s_1 s_2$ .

**Total correction.** Multiplying all the correction factors, the total correction factor  $C_{tot} = L_\varphi C_{rod} P C_{area}$ . The measured integrated intensity  $I_{measured} = I_{calc} C_{tot}$ , where  $I_{calc}$  is the intensity calculated from structure factor terms using equation 3.14. Since the geometry corrections are dependent of the measurement angles, we can only correct the measured data points,  $I_{corr} = I_{measured}/C_{tot}$ , and compare the calculated intensity  $I_{calc}$  with the corrected data  $I_{corr}$ .

### A.3.2 Stationary geometry (specular reflectivity)

Specular reflectivity is a special case for crystal truncation rods, it requires incident angle equals exit angle and no in-plane momentum transfer,  $\alpha = \gamma = \theta$  and  $\delta = 0$  with  $Q = Q_z = \frac{4\pi}{\lambda} \sin\theta = \frac{2\pi L}{c_H}$ .

**Lorentz factor.** If the measurement is done for specular without rocking scans, the stationary Lorentz factor is simply  $L_s = \frac{1}{\sin\theta}$ .

**Polarization factor.** The polarization factor simplifies to  $P = \cos^2(2\theta)$ .

**Active area.** There is no in-plane angle between the incoming and outgoing beam, and the detector acceptance is wider than the beam size, so all the beam illuminated on the sample get detected, the active area is the beam footprint on the sample  $A_{geo} = \frac{s_1 s_0}{\sin\alpha}$ , take  $A_0 = s_1 s_0$  this time, then  $C_{area} = \frac{1}{\sin\alpha} = \frac{1}{\sin\theta}$ .

**Footprint.** At low  $Q$ , the beam footprint is larger than the sample size and part of the beam spills off. We have to correct for the active area at low  $Q$  ( $L < 0.7$  for Ag/Si with 16.2 keV energy beam).  $F_p = \frac{\sin\alpha}{\sin\alpha_1} = \frac{L}{L_1} (L < L_1)$ .

**Refraction correction.** This is not a correction factor we multiply at the end, it is carried out in structure factor calculations. Because of the refraction index for x-ray is slightly less than unity, there is the total refraction region below  $Q_c$ [32]. When we calculate the structure factors, we need to use the internal wave vector  $Q_i$  instead of  $Q$ , with  $Q_i^2 = Q^2 - Q_c^2$ .

**Total correction.** The total correction factor  $C_{tot} = L_s P C_{area} F_p$  (practically we use  $1/Q^2$  for  $L_s C_{area}$ ). Since this time we only have one angle  $\theta$ , and it is directly related with  $Q$  and  $L$ , the geometry correction factor could be calculated together with the structure factors. The correction is done on the structure factor calculation  $I_{corr} = I_{calc} C_{tot}$ , and we compare  $I_{corr}$  with  $I_{measured}$ .



# Bibliography

- [1] John A. Venables. *Introduction to Surface and Thin Film Process*. Cambridge University Press, 2000.
- [2] I. K. Robinson and D. J. Tweet. Surface x-ray diffraction. *Reports on Progress in Physics*, 55(5):599, 1992.
- [3] D. A. Evans, M. Alonso, R. Cimino, and K. Horn. Observation of quantum size effects in photoemission from Ag islands on GaAs(110). *Physical Review Letters*, 70(22):3483–3486, 1993.
- [4] Arthur R. Smith, Kuo-Jen Chao, Qian Niu, and Chih-Kang Shih. Formation of atomically flat silver films on GaAs with a “silver mean” quasi periodicity. *Science*, 273(5272):226–228, 1996.
- [5] Luca Gavioli, Kevin R. Kimberlin, Michael C. Tringides, John F. Wendelken, and Zhenyu Zhang. Novel growth of Ag islands on Si(111): Plateaus with a singular height. *Physical Review Letters*, 82(1):129–132, 1999.

- [6] K. Budde, E. Abram, V. Yeh, and M. C. Tringides. Uniform, self-organized, seven-step height Pb/Si(111)-(7x7) islands at low temperatures. *Physical Review B*, 61(16):R10602–R10605, 2000.
- [7] M. Hupalo, S. Kremmer, V. Yeh, L. Berbil-Bautista, E. Abram, and M. C. Tringides. Uniform island height selection in the low temperature growth of Pb/Si(111)-(7x7). *Surface Science*, 493(13):526–538, 2001.
- [8] D.-A. Luh, T. Miller, J. J. Paggel, M. Y. Chou, and T.-C. Chiang. Quantum electronic stability of atomically uniform films. *Science*, 292(5519):1131–1133, 2001.
- [9] Roberto Otero, Amadeo L. Vázquez de Parga, and Rodolfo Miranda. Observation of preferred heights in Pb nanoislands: A quantum size effect. *Physical Review B*, 66(11):115401, 2002.
- [10] Mustafa M. Ozer, Yu Jia, Biao Wu, Zhenyu Zhang, and Hanno H. Weiering. Quantum stability and reentrant bilayer-by-bilayer growth of atomically smooth Pb films on semiconductor substrates. *Physical Review B*, 72(11):113409, 2005.
- [11] A. Gray, Y. Liu, Hawoong Hong, and T. C. Chiang. X-ray diffraction studies of trilayer oscillations in the preferred thickness of In films on Si(111). *Physical Review B*, 87(19):195415, 2013.
- [12] Zhenyu Zhang, Qian Niu, and Chih-Kang Shih. “Electronic growth” of metallic overlayers on semiconductor substrates. *Physical Review Letters*, 80(24):5381–5384, 1998.

- [13] F. K. Schulte. A theory of thin metal films: electron density, potentials and work function. *Surface Science*, 55:427–444, 1976.
- [14] Peter J. Feibelman. Static quantum-size effects in thin crystalline, simple-metal films. *Physical Review B*, 27(4):1991–1996, 1983.
- [15] Pavel Sobotik, Ivan Ost’adal, Josef Myslivecek, Tomas Jarolimek, and Frantisek Lavicky. Transition from 2d to 3d growth during Ag/Si(111)-(7x7) heteroepitaxy. *Surface Science*, 482485, Part 2(0):797–801, 2001.
- [16] D. K. Goswami, K. Bhattacharjee, B. Satpati, S. Roy, P. V. Satyam, and B. N. Dev. Preferential heights in the growth of Ag islands on Si(111)-(7x7) surfaces. *Surface Science*, 601(3):603–608, 2007.
- [17] Baris Unal, Alex Belianinov, P. A. Thiel, and M. C. Tringides. Lattice expansion in islands stabilized by electron confinement: Ag on Si(111)-7x7. *Physical Review B*, 81(8):085411, 2010.
- [18] B. J. Hinch, C. Koziol, J. P. Toennies, and G. Zhang. Evidence for quantum size effects observed by helium atom scattering during the growth of Pb on Cu(111). *EPL (Europhysics Letters)*, 10(4):341, 1989.
- [19] MustafaM Ozer, Cai-Zhuang Wang, Zhenyu Zhang, and HannoH Weitering. Quantum size effects in the growth, coarsening, and properties of ultra-thin metal films and related nanostructures. *Journal of Low Temperature Physics*, 157(3-4):221–251, 2009.
- [20] W. B. Su, C. S. Chang, and T. Tsong Tien. Quantum size effect on ultra-thin metallic films. *Journal of Physics D: Applied Physics*, 43(1):013001, 2010.

- [21] T. C. Chiang. Photoemission studies of quantum well states in thin films. *Surface Science Reports*, 39(78):181–235, 2000.
- [22] M. Milun, P. Pervan, and D. P. Woodruff. Quantum well structures in thin metal films: simple model physics in reality? *Reports on Progress in Physics*, 65(2):99, 2002.
- [23] Biao Wu and Zhenyu Zhang. Stability of metallic thin films studied with a free electron model. *Physical Review B*, 77(3):035410, 2008.
- [24] C. M. Wei and M. Y. Chou. Theory of quantum size effects in thin Pb(111) films. *Physical Review B*, 66(23):233408, 2002.
- [25] Neil Ashcroft and David Mermin. *Solid State Physics*. Thomson Learning, 1976.
- [26] Hawoong Hong, C. M. Wei, M. Y. Chou, Z. Wu, L. Basile, H. Chen, M. Holt, and T. C. Chiang. Alternating layer and island growth of Pb on Si by spontaneous quantum phase separation. *Physical Review Letters*, 90(7):076104, 2003.
- [27] C. A. Jeffrey, E. H. Conrad, R. Feng, M. Hupalo, C. Kim, P. J. Ryan, P. F. Miceli, and M. C. Tringides. Influence of quantum size effects on island coarsening. *Physical Review Letters*, 96(10):106105, 2006.
- [28] C. A. Jeffrey, R. Feng, E. H. Conrad, P. F. Miceli, C. Kim, M. Hupalo, M. C. Tringides, and P. J. Ryan. The growth of Pb nanocrystals on Si(111)7x7 : Quantum size effects. *Superlattices and Microstructures*, 41(23):168–177, 2007.
- [29] Lin Huang, S. Jay Chey, and J. H. Weaver. Metastable structures and critical thicknesses: Ag on Si(111)-7x7. *Surface Science*, 416(12):L1101–L1106, 1998.

- [30] B. E. Warren. *X-ray diffraction*. Dover Publications, Inc., 1990.
- [31] John Jackson. *Classical Electrodynamics Third Edition*. Wiley, 1998.
- [32] P. F. Miceli. *Semiconductor Interfaces, Microstructures and Devices: Properties and Applications Chapter 4*. IOP publishing, 1993.
- [33] W. C. Elliott, P. F. Miceli, T. Tse, and P. W. Stephens. Orientation dependence of homoepitaxy: An in situ x-ray scattering study of Ag. *Physica B: Condensed Matter*, 221(14):65–69, 1996.
- [34] I. K. Robinson and E. Vlieg. X-ray reflectivity study of the Si(111)7x7 surface. *Surface Science*, 261(13):123–128, 1992.
- [35] B. D. Cullity. *Elements of X-Ray Diffraction (2nd Edition)*. Addison-Wesley Longman, Inc, 1978.
- [36] Kunio Takayanagi, Yasumasa Tanishiro, Shigeki Takahashi, and Masaetsu Takahashi. Structure analysis of Si(111)-7x7 reconstructed surface by transmission electron diffraction. *Surface Science*, 164(23):367–392, 1985.
- [37] I. K. Robinson. Symmetry of Si(111)7x7 at an a-Si interface. *Physical Review B*, 35(8):3910–3913, 1987.
- [38] I. K. Robinson, W. K. Waskiewicz, R. T. Tung, and J. Bohr. Ordering at Si(111)/a-Si and Si(111)/SiO<sub>2</sub> interfaces. *Physical Review Letters*, 57(21):2714–2717, 1986.
- [39] E. Vlieg. Integrated intensities using a six-circle surface x-ray diffractometer. *Journal of Applied Crystallography*, 30(5 Part 1):532–543, 1997.

- [40] R. Feidenhans'l. Surface structure determination by x-ray diffraction. *Surface Science Reports*, 10(3):105–188, 1989.
- [41] R. D. Aburano, Hawoong Hong, J. M. Roesler, K. Chung, D. S. Lin, P. Zschack, H. Chen, and T. C. Chiang. Boundary-structure determination of Ag/Si(111) interfaces by x-ray diffraction. *Physical Review B*, 52(3):1839–1847, 1995.
- [42] W. B. Su, H. Y. Lin, Y. P. Chiu, H. T. Shih, T. Y. Fu, Y. W. Chen, C. S. Chang, and Tien T. Tsong. Correlation between morphological transition and preferred thickness of Pb and Ag islands on Si(111)7x7. *Physical Review B*, 71(7):073304, 2005.
- [43] Shawn T. Hayden. *SUBSURFACE STRUCTURE and MORPHOLOGY: EPI-TAXIAL METAL FILM GROWTH STUDIED BY IN SITU X-RAY SCATTERING*. Dissertation, 2014.
- [44] Yong Han and Da-Jiang Liu. Quantum size effects in metal nanofilms: Comparison of an electron-gas model and density functional theory calculations. *Physical Review B*, 80(15):155404, 2009.
- [45] Dahai Shao, Xiaojie Liu, Ning Lu, C. Z. Wang, Kai-Ming Ho, M. C. Tringides, and P. A. Thiel. Effect of oxygen on the stability of Ag islands on Si(111)-7x7. *Surface Science*, 606(2324):1871–1878, 2012.
- [46] Adrian C. Melissinos. *Experiments In Modern Physics*. Academic Press, 1966.
- [47] J. W. Evans, P. A. Thiel, and M. C. Bartelt. Morphological evolution during epitaxial thin film growth: Formation of 2d islands and 3d mounds. *Surface Science Reports*, 61(12):1–128, 2006.

- [48] K. J. Caspersen and J. W. Evans. Metal homoepitaxial growth at very low temperatures: Lattice-gas models with restricted downward funneling. *Physical Review B*, 64(7):075401, 2001.
- [49] C. E. Botez, W. C. Elliott, P. F. Miceli, and P. W. Stephens. Vacancy formation in homoepitaxially grown Ag films and its effect on surface morphology. *Physical Review B*, 66(7):075418, 2002.
- [50] C. E. Botez, K. Li, E. D. Lu, W. C. Elliott, P. F. Miceli, E. H. Conrad, and P. W. Stephens. Vacancy trapping and annealing in noble-metal films grown at low temperature. *Applied Physics Letters*, 81(25):4718–4720, 2002.
- [51] C. E. Botez, P. F. Miceli, and P. W. Stephens. Temperature-dependent vacancy formation during the growth of Cu on Cu(001). *Physical Review B*, 66(19):195413, 2002.
- [52] Chinkyoo Kim, Rui Feng, Edward H. Conrad, and Paul F. Miceli. Nanoclustering of vacancies in thin metal films revealed by x-ray diffuse scattering. *Applied Physics Letters*, 91(9):093131–3, 2007.
- [53] Chinkyoo Kim, Edward H. Conrad, and Paul F. Miceli. X-ray diffuse scattering study of vacancy nanoclusters in homoepitaxial Ag(001) films. *Physical Review B*, 86(15):155446, 2012.
- [54] Yunsic Shim, Valery Borovikov, Blas P. Uberuaga, Arthur F. Voter, and Jacques G. Amar. Vacancy formation and strain in low-temperature Cu/Cu(100) growth. *Physical Review Letters*, 101(11):116101, 2008.

- [55] P. H. Dederichs. Diffuse scattering from defect clusters near bragg reflections. *Physical Review B*, 4(4):1041–1050, 1971.
- [56] M.A. Krivoglaz. *X-Ray and Neutron Diffraction in Nonideal Crystals*. Springer-Verlag, 1996.
- [57] P. H. Dederichs. Effect of defect clustering on anomalous x-ray transmission. *Physical Review B*, 1(4):1306–1317, 1970.
- [58] L. D. Landau and E. M. Lifshitz. *Theory of elasticity*, volume 7 of *Course of Theoretical Physics*. Pergamon Press, second edition edition, 1970.
- [59] Simulation data courtesy of J. Amar.
- [60] William Humphrey, Andrew Dalke, and Klaus Schulten. VMD: Visual Molecular Dynamics. *Journal of Molecular Graphics*, 14(1):33–38, 1996.
- [61] Reinhard B. Neder and Thomas Proffen. *Diffuse Scattering and Defect Structure Simulations*. Oxford University Press, 2008.
- [62] H. You. Angle calculations for a ‘4s+2d’ six-circle diffractometer. *Journal of Applied Crystallography*, 32(4):614–623, 1999.
- [63] M. Lohmeier and E. Vlieg. Angle calculations for a six-circle surface x-ray diffractometer. *Journal of Applied Crystallography*, 26(5):706–716, 1993.



## VITA

Yiyao Chen was born October 14, 1986 in Jiangsu, China and attended Nanjing Foreign Language School. He received his B.S. degree in Physics from Shanghai Jiao Tong University in July 2008. He received his M.S. degree in Physics from University of Missouri in July 2010 and will receive the Ph.D. degree in Physics from University of Missouri in May 2016.